Experimental and Theoretical Analysis of the Impact with Solid and Flexible Surfaces

by

Ozdes Cermik

A dissertation submitted to the Graduate Faculty of
Auburn University
in partial fulfillment of the
requirements for the Degree of
Doctor of Philosophy

Auburn, Alabama
May 6, 2017

Keywords: Collision, Image Processing, Friction, Spherical Impact

Copyright 2017 by Ozdes Cermik

Approved by

Dan B. Marghitu, Chair, Professor of Mechanical Engineering
Sabit Adanur, Co-Chair, Professor of Mechanical Engineering
Robert L. Jackson, Professor of Mechanical Engineering
Joseph Ragan, Assistant Professor of Mechanical Engineering

Abstract

Impact plays an important role in many engineering applications, mechanical systems, and different areas such as robotics, machine design, etc. It is a complex phenomenon that occurs when two or more bodies collide. In the textile industry, weaving machines with projectile and shuttle filling insertion systems provide good examples of collision during fabric manufacturing.

This work investigates the normal and oblique impact on flexible and rigid surfaces through experimental and analytical methods. Three different cases, including, the impact of a hollow sphere on a flexible flat, the impact of a solid rubber sphere on a wooden flat, and the impact of a rod on a deformable flat have been studied. The experiments are performed using either a high speed or an infrared camera depending on the study. The high speed camera provides the opportunity to study the motion during the impact due to better frequency. The motions of the spheres have been captured at 10,000 frames per second. The image processing technique with a digital image correlation method has been developed to measure the motion of the spheres. A speckle pattern study has been done to find the optimum pattern for the image processing method. The Hough transform method has been used to track the position of the centroid of the spheres. The linear and angular motion of the spheres have been analyzed before, during, and after the impact.

The oblique impact of a hollow sphere on a flexible surface has been modeled with a spring-damper system. The impact has been divided into two sub-phases: compression and restitution. The contact force expression has been determined for the compression and the restitution phases using the experimental data from the normal impact experiments. Experiments have been done for a wide range of impact angles and initial velocities. The coefficient of restitution and effective coefficient of friction have been analyzed experimentally.

The simulation and experimental results have been compared, and the model is verified for the oblique impacts.

The oblique impact of a solid rubber sphere on a wooden flat has been studied. The wooden flat is considered to be rigid. The digital image processing method has been used to measure the linear and angular velocities of the sphere during the impact. A theoretical model has been proposed for both the normal and tangential directions. The normal force has been divided into two sub-phases: compression and restitution. The tangential force is considered to be the friction force and has been divided into three sub-phases during the impact: sliding, sticking and post-sliding. The model has been compared and verified with the experiments.

An experimental study has been done for the impact of a rod on a deformable flat. The motion of the rod before and after the impact has been accurately captured with a 3D infrared camera. The results in terms of rebound angular velocity, coefficient of restitution, and permanent deformation on the flat have been compared for different impact angles. An optical profilometer has been used to measure the permanent deformation after the impact.

Acknowledgments

I would like to acknowledge everyone who assisted me throughout my doctoral studies over the years. First and foremost I like to thank and dedicate all my success to my family my lovely wife Mehtap, my son Toprak and my daughter Derin. Their everyday endless love, support, and encouragement was what made my doctoral studies and this dissertation possible.

I would like to acknowledge my advisor, Prof. Dan Marghitu for his support and guidance which made my doctoral studies a very good experience. I would like to thank my Co-advisor Prof. Sabit Adanur, dissertation committee members Prof. Robert Jackson and Dr. Joseph Ragan for all of their guidance through the process. I should express many thanks to my lab mates, especially Hamid Ghaednia for their helps. Thanks to Dr. Andres Carrano and Mr. Kamran Kardel for assistance with the optical profilometer.

I would like to thank Republic of Turkey Ministry of National Education for the opportunity to study abroad and covering all of my expenses throughout my studies in the USA.

Last but not least, I like to thank my parents, my mother-in-law, my sister, my brother and brother-in-law for their continuous support and inspiration.

Table of Contents

Abstract ii

Acknowledgments iv

List of Figures vii

List of Tables xiv

1 Introduction and literature review 1

2 Digital image processing method 12

2.1 Introduction 12

2.2 Method 15

2.3 Speckle pattern analysis 17

2.4 Experiments 23

2.4.1 Oblique impact of a tennis ball with a racket 24

2.4.2 Oblique impact of a lacrosse ball with a wooden flat 29

2.5 Conclusion 33

3 Impact of a hollow ball with a flexible flat 34

3.1 Dynamics of the ball 34

3.1.1 Compression Phase 36

3.1.2 Restitution Phase 38

3.1.3 Simulation results 38

3.2 Experiments 41

3.2.1 Image processing 42

3.2.2 Experimental results 45

3.2.3 Coefficient of restitution 53

3.2.4 Effective coefficient of friction 54

3.3 Comparing the theory and experiments 56
3.3.1 Finding force coefficients 56
3.3.2 Verifying the theory for the oblique impact 59
3.4 Discussion 66
3.5 Conclusion 67
4 Impact of a solid rubber ball with a rigid flat 68
4.1 Dynamics of the impacting ball 68
4.2 Theoretical model 70
4.2.1 Normal force 70
4.2.2 Tangential force 72
4.3 Experiments 74
4.4 Comparing the theory with the experiments 79
4.5 Discussion and conclusion 85
5 Experimental study of the impact of a rod with a flat 87
5.1 Dynamics of the rod 87
5.2 Experiments 89
5.3 Results 91
5.4 Conclusion 101
6 Conclusions 102

List of Figures

1.1 The illustration of an impact of a sphere and a rigid flat. 2

1.2 Typical contact force-time profile. 3

1.3 Typical contact force-deformation profile. 4

1.4 Schematic of deformed objects, (a) indentation (b) flattening. 9

2.1 Spline interpolation for a 15×15 pixel interrogation window: (a) the original image, (b) spline interpolation with 5 extra points in between pixels. 16

2.2 Computation time versus the number of extra points in the interpolation for a 15×15 pixel interrogation window shown in Fig. 2.1. 16

2.3 Speckle patterns used in this study; (a) to (f) show different speckle patterns and indexes I to III show different densities for each speckle pattern with I and III being the least and most dense, respectively. 18

2.4 Speckle pattern study for the translation in one direction. 20

2.5 Speckle pattern study for the translation in two directions. 20

2.6 Speckle pattern study for pure rotation. 21

2.7 Speckle pattern study for the general motion. 22

2.8 Experimental setup for the impact of the tennis ball with the racket; (a) front view, (b) right view. 24

2.9 Experimental setup for the impact of the lacrosse ball with a wooden flat: (a) front view, (b) right view. 25

2.10 Original frames and the velocity field of the impact of a tennis ball with a racket calculated by DIC: (a) the beginning of the impact , (b) during the impact, (c) the end of the impact. 26

2.11 Position of the centroid of the tennis ball measured by Hough transform method. 27

2.12 Velocity of the centroid of the tennis ball with the DIC method. 28

2.13 Angular velocity of the tennis ball measured by the DIC method. 29

2.14 Original frames and the velocity field of the impact of a lacrosse ball with a wooden flat calculated by DIC: (a) the beginning of the impact, (b) during the impact, (c) the end of the impact. 30

2.15 Position of the centroid of the lacrosse ball measured by Hough transform method. 31

2.16 Velocity of the centroid of the lacrosse ball with the DIC method. 32

2.17 Angular velocity of the lacrosse ball measured by the DIC method. 32

3.1 Tennis ball in contact with the string-bed. 35

3.2 The sketch of the impact model. 36

3.3 The displacement of the center of the ball during the impact in local coordinates $[\mathbf{\imath}, \mathbf{\jmath}, \mathbf{k}]$ for the impact angle $\beta = 15°$. 39

3.4 The velocity of the center of the ball during the impact in local coordinates $[\mathbf{\imath}, \mathbf{\jmath}, \mathbf{k}]$ for the impact angle $\beta = 15°$. 40

3.5 The normal contact force and the displacement during the impact for $\beta = 15°$. . 41

3.6 Image of the ball just before impacting the racket. 42

3.7 Modifying the contrast and finding the boundary. 43

3.8 Calculating the position of the center of the ball. 43

3.9 Tracking the position of the center of the ball while part of it is covered with the racket. 44

3.10 Trajectory of the ball for different impact angles with the Hough transform method: (a) normal impact, (b) $\beta = 15°$, (c) $\beta = 30°$, (d) $\beta = 45°$,(e) $\beta = 57°$. . 45

3.11 The displacement of the center of the ball in global $[\mathbf{i}_0, \mathbf{j}_0, \mathbf{k}_0]$ and local coordinates $[\mathbf{i}, \mathbf{j}, \mathbf{k}]$ for the impact angle $\beta = 0°$. 46

3.12 The displacement of the center of the ball in global coordinates $[\mathbf{i}_0, \mathbf{j}_0, \mathbf{k}_0]$ for the impact angle $\beta = 15°$. 47

3.13 The displacement of the center of the ball in local coordinates $[\mathbf{i}, \mathbf{j}, \mathbf{k}]$ for the impact angle $\beta = 15°$. 47

3.14 The displacement of the center of the ball in global coordinates $[\mathbf{i}_0, \mathbf{j}_0, \mathbf{k}_0]$ for the impact angle $\beta = 30°$. 48

3.15 The displacement of the center of the ball in local coordinates $[\mathbf{i}, \mathbf{j}, \mathbf{k}]$ for the impact angle $\beta = 30°$. 49

3.16 Path of the center of the ball in global $[\mathbf{i}_0, \mathbf{j}_0, \mathbf{k}_0]$ and local $[\mathbf{i}, \mathbf{j}, \mathbf{k}]$ coordinates for the impact angle $\beta = 30°$. 49

3.17 The displacement of the center of the ball in global coordinates $[\mathbf{i}_0, \mathbf{j}_0, \mathbf{k}_0]$ for the impact angle $\beta = 45°$. 50

3.18 The displacement of the center of the ball in local coordinates $[\mathbf{i}, \mathbf{j}, \mathbf{k}]$ for the impact angle $\beta = 45°$. 51

3.19 The displacement of the center of the ball in global coordinates $[\mathbf{\imath}_0, \mathbf{\jmath}_0, \mathbf{k}_0]$ for the impact angle $\beta = 57°$. 52

3.20 The displacement of the center of the ball in local coordinates $[\mathbf{\imath}, \mathbf{\jmath}, \mathbf{k}]$ for the impact angle $\beta = 57°$. 52

3.21 Coefficient of restitution for different initial normal velocities from 0.5 to 4.5 m/s. 53

3.22 Average coefficient of restitution for different impact angles β. 54

3.23 Effective coefficient of friction for different initial velocities from 0.5 to 4.5 m/s and different impact angles β. 55

3.24 Variation of the effective coefficient of friction for different impact angles β. . . 55

3.25 Displacement mean absolute error for the variation of k and b. 57

3.26 Velocity after the impact mean absolute error for the variation of k and b. . . . 57

3.27 Multiplication of mean absolute error for the variation of k and b. 58

3.28 Summation of mean absolute error for the variation of k and b. 58

3.29 Summation of error with 2D spline interpolation. 59

3.30 Comparison between the theory and experiment for the normal component of the displacement for the oblique impact with $\beta = 15°$. 60

3.31 Comparison between the theory and experiment for the tangential component of the displacement for the oblique impact with $\beta = 15°$. 61

3.32 Comparison between the theory and experiment for the normal component of the displacement for the oblique impact with $\beta = 30°$. 62

3.33 Comparison between the theory and experiment for the tangential component of the displacement for the oblique impact with $\beta = 30°$. 62

3.34 Comparison between the theory and experiment for the normal component of the displacement for the oblique impact with $\beta = 45°$. 63

3.35 Comparison between the theory and experiment for the tangential component of the displacement for the oblique impact with $\beta = 45°$. 64

3.36 Comparison between the theory and experiment for the normal component of the displacement for the oblique impact with $\beta = 57°$. 65

3.37 Comparison between the theory and experiment for the tangential component of the displacement for the oblique impact with $\beta = 57°$. 65

3.38 Comparison of the coefficient of restitution between the experiments and the theory. 66

4.1 Lacrosse ball in contact with the wooden flat. 68

4.2 Contact force during the impact. 73

4.3 Velocity of the centroid of the lacrosse ball with the DIC method for the normal impact. 75

4.4 Velocity of the centroid of the lacrosse ball with the DIC method at $\beta = 20°$ . . 76

4.5 Angular velocity of the centroid of the lacrosse ball measured with the DIC method at $\beta = 20°$. 77

4.6 Velocity of the centroid of the lacrosse ball with the DIC method at $\beta = 40°$ . . 78

4.7 Angular velocity of the centroid of the lacrosse ball measured with the DIC method at $\beta = 40°$. 78

4.8 Coefficient of restitution for different initial normal velocities. 79

4.9 Comparing the models with the experiment at $\beta = 20°$ for the tangential velocity of the center of the ball. 82

4.10 Comparing the models with the experiment at $\beta = 20°$ for the tangential velocity of the tip of the ball. 82

4.11 Comparing the models with the experiment at $\beta = 30°$ for the tangential velocity of the center of the ball. 84

4.12 Comparing the models with the experiment at $\beta = 40°$ for the tangential velocity of the center of the ball. 85

5.1 The rod impacting the flat. 88

5.2 Experimental setup for the impact of the rod (a) right view, (b) front view. . . 90

5.3 Experimental setup for the impact of the rod (a) rod is held by the dropping device, (b) infrared camera. 90

5.4 Position of the center of the rod before and after the impact for angle 45°. . . . 91

5.5 Velocity of the center of the rod before and after the impact for angle 45°. . . . 92

5.6 Angular velocity of the rod before and after the impact for angle 45°. 93

5.7 Coefficient of restitution as a function of initial impact velocity at $\theta = 17°$. . . . 94

5.8 Coefficient of restitution as a function of initial impact velocity at $\theta = 45°$. . . . 94

5.9 Coefficient of restitution as a function of initial impact velocity at $\theta = 70°$. . . . 95

5.10 Comparision of the coefficient of restitution as a function of initial impact velocity for all of the impact angles. 96

5.11 Permanent deformation as a function of initial impact velocity at $\theta = 17°$. . . . 97

5.12 Permanent deformation as a function of initial impact velocity at $\theta = 45°$. . . . 97

5.13 Permanent deformation as a function of initial impact velocity at $\theta = 70°$. . . . 98

5.14 Comparison of the permanent deformation as a function of initial impact velocity for all of the impact angles. 98

5.15 Angular velocity after the impact as a function of initial impact velocity at $\theta = 17°$. 99

5.16 Angular velocity after the impact as a function of initial impact velocity at $\theta = 45°$.100

5.17 Angular velocity after the impact as a function of initial impact velocity at $\theta = 70°$.100

5.18 Comparison of the angular velocity after the impact as a function of initial impact velocity for all of the impact angles. 101

List of Tables

5.1 The material properties of the rod and the flat 87

Chapter 1

Introduction and literature review

Impact is a complicated physical phenomenon which occurs when two objects collide with each other. It involves large reaction forces and changes in velocity of the colliding bodies. Many analytical, experimental, and numerical works have been done to simulate the motion of the objects with different geometries.

The history of the collision starts with Galileo in the seventeenth century who was considered the father of the modern science. He worked on falling objects but not specifically on collisions. The impact between two rigid bodies was initially analyzed by Newton in his work, "Philosophiae Naturalis Principia Mathematica ", which was appeared in 1686 [1]. Later, Maclaurin described the collision and elastic element between two rigid bodies and separated the impact into two phases: compression and restitution.

The most common method used to measure the energy lost in a collision is the coefficient of restitution which depends on many factors, such as the geometry of the colliding bodies, material properties, initial velocity, oblique angle, initial spin, and friction. The coefficient of restitution is usually defined by one of the following three ways:

$$e_1 = \frac{V_a}{V_b} \quad , \quad e_2 = \frac{I_R}{I_C} \quad , \quad e_1 = \sqrt{\frac{E_R}{E_C}} \tag{1.1}$$

the Newtonian or kinematic coefficient of restitution, e_1, which is widely used, is defined as the ratio between the velocity after (V_a) and before the impact (V_b) [1]. Poisson also worked on collision and introduced a new coefficient of restitution as the ratio between the normal restitution (I_R) and compression impulse (I_C) [2]. Stronge defined the energetic coefficient of restitution as the square root of the ratio of energy released during the restitution (E_R) to the energy absorbed during the compression (E_C) [3]. Among these three expressions,

the Newtonian coefficient of restitution is employed throughout this dissertation due to its simplicity.

Two main approaches are applied for the impact analysis. For the first approach, the impact duration and the deformation during the impact are neglected. The dynamic analysis involves pre and post impact phases. The impulse-momentum and the coefficient of restitution are crucial for the analysis [4, 5]. For the second approach, the impact duration is not neglected. The impact duration is estimated to be 10^{-5} second for metals and not longer than 10^{-2} second for softer materials such as strong rubbers. The colliding objects are not considered rigid, therefore, deformation is taken into consideration. The dynamic analysis involves before, during, and after the impact. In this approach, the contact force acts in a continuous manner during the impact. The contact forces are added to the equations of motion for the analysis, and the motion of the colliding objects is calculated by numerically solving the equations of motion. This approach describes the real behavior of the system in a better way.

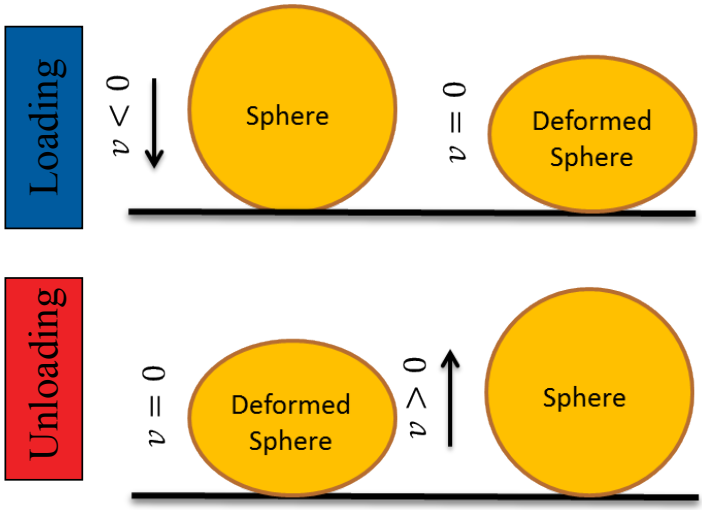

Figure 1.1: The illustration of an impact of a sphere and a rigid flat.

The colliding bodies are subjected to elastic and/or plastic deformation with energy lost in various forms. The dynamic of impact depends on many properties of colliding bodies such as material properties, geometry, linear and angular velocities. The impact can be divided

into two main phases: loading (compression) and unloading (restitution). The impact of a sphere with a flat surface is presented in Fig. 1.1. The loading phase starts when the sphere touches the flat and the sphere starts deforming depending on its stiffness properties. This phase ends when the normal velocity of the contact point of the sphere becomes zero. At this point, the contact force and the deformation of the sphere reach their maximum. The unloading phase starts from this point; the sphere starts regaining its shape, and the contact force decreases from maximum to zero.

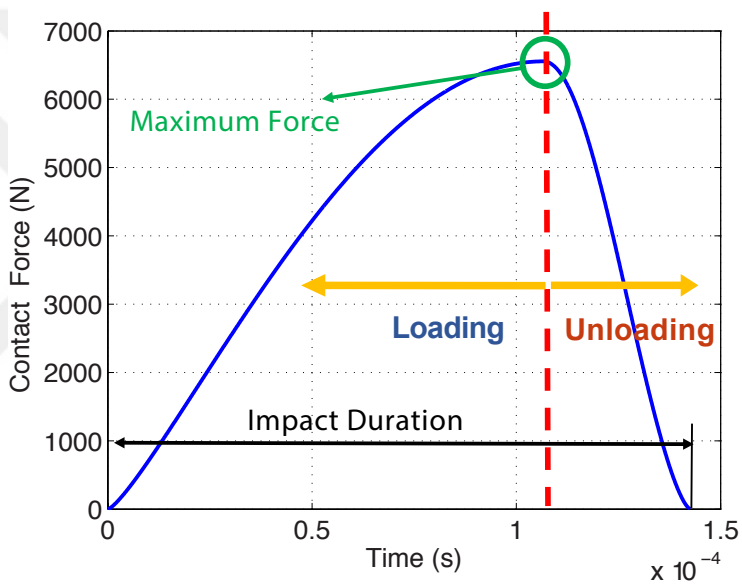

Figure 1.2: Typical contact force-time profile.

Figure 1.2 presents a typical contact force-time relation for an impact of sphere and a flat. The loading and unloading phases as well as the impact duration and the maximum contact force are shown in Fig. 1.2. The impact duration can be measured from the width of the force-time profile. Contact force increases as the sphere continues to deform and reaches its maximum when maximum deformation occurs.

A typical contact force-deformation profile can be seen in Fig. 1.3. Some of the deformation is not fully recoverable for the impact with sufficiently high velocities. This leaves permanent deformation (plastic deformation) as seen in Fig.1.3. The impact can be fully elastic where no energy is lost and no deformation occurs, fully plastic, where all energy

is lost and permanent deformation occurs, or elasto-plastic, where some energy is lost with some permanent deformation or no deformation.

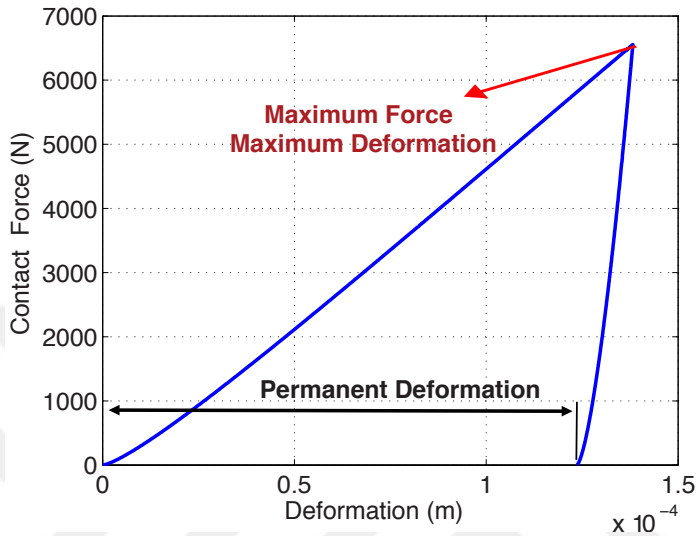

Figure 1.3: Typical contact force-deformation profile.

Many sports involve the impact of a ball that collides with another object such as a tennis ball on a court or racket, a soccer ball with a foot, or a golf ball with a golf club, etc. The impact duration is very short and ranges from $0.4 - 1$ millisecond for a golf ball [6], $7 - 9$ milliseconds for a soccer ball [7], $4 - 5$ milliseconds for a tennis ball [8], and $0.6 - 2$ milliseconds for a baseball [9]. Impact duration is found to decrease with increasing initial impact velocity.

The impact of a ball with a surface has been initially studied for the normal impact case where the ball impacts the surface vertically. The analysis gets more complicated when a ball is incident at an oblique angle on a surface due to friction force. Garwin [10] studied the oblique impact of a superball on a rigid surface. He assumed perfectly elastic collision in both normal and tangential directions. Therefore, kinetic energy was assumed to be conversed during the collision. The coefficient of restitution was considered to be 1. His model is a kinematic model which does not count the effect of friction. Brody [11] studied the oblique impact of a tennis ball on a surface of the court. He used the classical approach in the

analysis where deformation on the ball was neglected. Brody applied Newtonian mechanics and used the constant coefficient of restitution. Brody concluded that the ball without initial spin slides throughout the impact at a low impact angle relative to the horizontal surface with small friction force. If the friction force and the impact angle are large enough, the ball slides and begins to roll before it loses contact with the surface. He assumed the ball would roll when the angular velocity of the ball, ω, is v_x/R, where R is the radius of the ball, and v_x is the horizontal component of the ball's center of the mass velocity. Cross [12] developed an analytical model in order to study the effects of friction between the tennis ball and the racket strings. Similar to Brody's model [11], he assumed that the ball would either slide throughout the impact or slide and then roll. The coefficient of sliding and rolling frictions were measured experimentally. The study showed that a small decrease in the coefficient of sliding friction below 0.3 could result in large change for the rebound angle of the ball. However, the accuracy of the model was not verified with the experiments. Some studies [13, 14] showed that a ball in a rolling mode has smaller angular speed after the impact than the one that grips the surface. Cross [14] measured the horizontal coefficient of restitution for a superball and tennis ball on different surfaces. It was seen that a ball on a rolling mode can spin faster than its limit due to possible partial energy recovery in the horizontal direction.

Cross [8] studied the dynamic properties of different types of tennis balls during the impact. The contact force and duration were measured on a force plate. The actual change in ball diameter during compression was not measured in the experiments. Cross [13] studied grip-slip behavior of different types of balls using the same force plate. He measured the friction force during the impact. Unlike Garwin's [10] and Brody's [11] models, Cross showed that the ball does not roll when it bounces, but actually grips the surface. Cross showed that if the ball does not slide throughout the impact, friction force reverses direction during the impact. This reversal can happen more than once depending on the ball type [13]. Maw et al., [15] studied the oblique impact of elastic spheres on a half-space. They predicted this

reversal of the friction force theoretically. The coefficient of restitution was assumed to be 1 for the analysis. It has been shown by several authors that the coefficient of restitution is reduced with increasing initial velocity [8, 16, 17]. The coefficient of restitution is found to be higher for the oblique impacts than for the normal impacts as stated in [14, 18, 19].

The Kelvin-Voigh model, in which the Newtonian damper and the Hookean elastic spring are connected in a parallel system, has been used by several authors in order to model the impact between a ball and a surface. The spring simulates the ball stiffness while the damper simulates energy dissipation. Dignall and Haake [17] developed an analytical model of the normal impact of a tennis ball on a tennis court using the Kelvin-Voigh model. The stiffness and damping coefficients were analytically defined. The contact time and the coefficient of restitution were measured from the experiments. The stiffness and damping coefficients were calculated analytically using the coefficient of restitution and the contact time from the experiments. They were assumed to be constant throughout the impact. The model was extended to the oblique impact case and verified with the experiments. Haake et al., [16] used the force plate method as seen in [8] and high speed camera to study the motion of the ball with the tennis racket. They used Dignal and Haake's model [17] to calculate stiffness and damping coefficients for the impact of the different tennis balls with the tennis racket. It was shown that the stiffness and damping coefficients of the tennis ball increased with higher initial impact velocity of the ball [16, 17]. Goodwill and Haake [20] developed a model by adding a new linear spring in series with the Kelvin-Voigh model for the impact of a tennis ball with a racket string-bed. This extra spring was used to simulate the influence of the string-bed. The stiffness and damping coefficients of the ball were measured from the contact time and the coefficient of restitution assuming that the racket surface was rigid. The stiffness for the spring was measured from a compression test. These three coefficients were put into the model and the coefficient of restitution and maximum string-bed deflection were compared between the experiments and the model. Goodwill and Haake [21] established a viscoelastic model for the normal impact of a tennis ball on a rigid

surface. A new damper representing the large deformation on the ball was added in parallel with the classical spring-damper model. Carre et al., [22] studied the impact of a cricket ball on a rigid surface. The spring-damper model was used to predict the force-deflection behavior. The damping coefficient was varied with the contact area when the velocity before the impact is the main factor. Friction force direction reversal during the impact was seen in the model when rolling mode was reached. Yang et al., [23] developed a nonlinear impact model for the tennis ball and the racket. A nonlinear spring for the string-bed was connected in series with the spring-damper model. The effect of the ball damping ratio and the stiffness of the ball on the impact time and the coefficient of restitution were studied. However, there was no experimental data to verify the accuracy of the model. Ghaednia et al., [24] used spring-damper system for the impact of tennis ball with a tennis racket, and the impact is divided into two phases:compression and restitution. Restitution phase is considered fully elastic.

Cross [25, 26, 27] studied the impact behavior of hollow balls, rubber balls, and superballs. He experimentally measured the contact force acting on ping-pong and squash balls on a force plate [25]. Cross studied the oblique impact of a hollow rubber ball on a polished granite surface [26]. He used a high speed camera to observe the grip-slip behavior of the ball. The angular velocity during the impact was measured manually. Measurement of the normal and the friction forces were obtained using the same apparatus by the same author [13].

Finite element analysis (FEA) has been used in order to simulate the impact of different types of balls with different surfaces. However, it has to be noted that there is still serious problems with implementing the friction between contact elements. Hubbard and Stronge [28] applied FEA for the impact of a ping-pong ball on a rigid surface. Goodwill et al., [18] studied the oblique impact of a tennis ball with a rigid surface using FEA. Experimental data obtained from a force platform were compared with the simulation results. Allen et al., [29] developed a finite element model to simulate the oblique impact of a tennis ball on a

string-bed. Different initial velocities and impact angles have been tested and compared with the finite element method. Allen et al., [30] later studied the impact of a tennis ball on a freely suspended racket. Four different impact positions on the string-bed were tested for the normal impact. Later, Allen et al., [31] developed a new finite element model to simulate the influence of the friction on the impact between the tennis ball with the rigid surface and the string-bed. Rebound angle, rebound topspin, and the coefficient of restitution were obtained as a function of the coefficient of friction. The results showed that a tennis ball could undergo three phases depending on the magnitude of the frictional force for oblique impacts: sliding, over-spinning, and rolling. Rezaei et al., [32] used FEA for the oblique impact of a soccer ball. Simulation results showed that reversal of the direction on the friction force was seen with the increasing coefficient of friction.

Sphere contact models

If the collision is elastic, the contact force which acts on the ball during the collision can be given by Hooke's law $F = kx$, where x is the ball compression and k is the stiffness of the ball. The contact mechanic field includes various models for the contact behavior of elastic-plastic objects of several geometries. For an elastic collision of the sphere, the Hertzian theory [33] works well for a force law of the form $F = kx^{3/2}$. The Hertzian theory gives reasonable agreement for low speed ball impacts but it has limited applicability to most of the sports ball impacts. For most of the impact problems the objects deform plastically. Therefore, the Hertzian theory can not be sufficient by itself and this requires more advanced models to be applied. The contact of a hemisphere with a surface has been studied by many researchers. There are two main approaches when dealing with the contact of hemisphere with a flat: indentation and flattening. For the indentation approach, the hemisphere is considered to be rigid and the flat deforms as seen in Fig. 1.4 (a). For the flattening approach, the flat is considered to be rigid and the hemisphere deforms as seen in Fig. 1.4 (b).

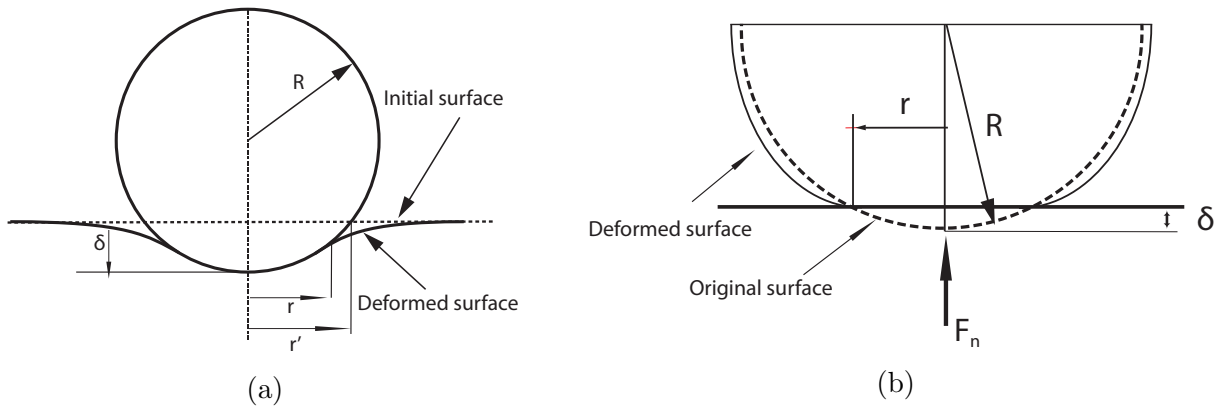

Figure 1.4: Schematic of deformed objects, (a) indentation (b) flattening.

The indentation models have initially been used for the hardness test [34, 35, 36, 37] Johnson [38] developed the simple plastic contact model, in which the contact is divided into two phases: the fully elastic and the fully plastic. The Hertzian theory was used for the fully elastic phase. He considered hardness to be constant for the fully plastic phase. Komvopoulos studied the indentation of a rigid sphere on a layered flat and developed a formulation for a homogeneous flat [39, 40]. Later Ye and Komvopoulos developed a new formulation [41] for the contact force. Kogut and Komvopolous improved the model and a new formulation was given [42]. Jackson et al., [43] calculated the hardness as a function of radius of contact using the slip-line theory. Brake [44] presented a contact model, in which the contact is divided into two phases: elastic and elasto-plastic. He used the Hertzian theory for the elastic phase and Meyer's hardness for the plastic phase.

Flattening models have been studied since the 1960s. In 1968, Johnson studied the fully plastic contact between spheres and cylinders experimentally [45]. Li et al., [46] modified Thornton's contact model [47, 48] with detailed pressure distribution based on FEA modeling. Wu et al., completed a new model for the unloading phase of the impact of an elasto-plastic sphere with a hard flat [49]. Kogut and Etsion [50] developed a new empirical formulation for the elasto-plastic contact of a hemisphere with a rigid flat. The contact is divided into two sub-phases during the loading phase: fully elastic and fully plastic phases. Etsion et al., [51] improved the unloading phase and provided new empirical formulation.

The unloading phase was considered to be elasto-plastic for this study. Jackson and Green [52] developed a new contact model between an elasto-plastic half sphere and a rigid flat. Hardness is not considered to be constant and changes during the contact. This model works for larger deformation. Brake [53] developed a new analytical model and divided the contact into four phases: fully elastic, elasto-plastic, fully plastic, and restitution phases. Cermik et al., [54] used Jackson-Green contact model [52] for the oblique impact of a rod with a metal flat.

The above contact models consider one the objects as rigid while the other one undergoes deformation. Ghaednia et al., [55] accounts for the effect of deformation on both of the objects. This model shows the transition between flattening and indentation regimes using the yield strength ratio defined by the authors.

Contact models used for impact problems

Contact models were previously applied to impact problems. Stronge used Johnson's elastic-fully plastic contact model [38] and defined a new energetic coefficient of restitution [56]. The impact is divided into three phases: fully elastic, fully plastic, and restitution [3, 57]. The fully elastic phase and the restitution phase follow the Hertzian theory. The fully plastic phase follows Johnson's expression [38]. Thornton [48] provided an analytical solution on the elastic-perfectly plastic impact. Kharaz et al., studied the impact of aluminum balls with a massive steel surface experimentally [58]. Jackson et al., [59] used the Jackson-Green contact model in order to predict the coefficient of restitution for the impact of an elasto-plastic sphere with a rigid flat. Marghitu et al., [60] studied the impact of a rotating link with a massive surface and applied the Jackson-Green contact model. Brake [53] used his contact model for the normal impact and compared it with Kharaz's experimental study.

The next three chapters elaborate on the results and progress of our projects. Chapter 2 presents a new image processing method with the digital image correlation technique. The goal of this study is to use the digital image correlation methods for the impact problems.

To the best of our knowledge, the digital image correlation methods have never been implemented for the collision problems. The method enables us to analyze the motion of the ball before, during, and after the impact. In the third and fourth chapters, the impact of an hollow ball on a flexible surface and a rubber ball on a rigid wooden surface have been studied experimentally and theoretically, respectively. The goal of this studies is to measure the linear and angular velocities of the balls before, during, and after the impact. A theoretical model for each study has been proposed. The models have been compared with the experiments. Chapter 5 presents an experimental study on the oblique impact of a rod on a deformable flat. The final chapter is the conclusions of all the discussions of the dissertation.

Chapter 2

Digital image processing method

2.1 Introduction

Applications of video analysis to investigate the motion of objects have been utilized by many authors. Experiments with video analysis enhance the understanding of dynamic and kinematic concepts. Analyzing the motion of objects during the impact is always a challenge due to small impact duration and deformation. The deformation during the impact is significantly small, especially for the impact with a low initial velocity. The accuracy usually is not high enough compared to the scale of deformation on the colliding objects to trust the measurements. This requires high accuracy devices or methods to be used in order to measure and predict the motion of the objects during the impact.

There have been many efforts on measuring the motion of objects during impact. Stoianovici and Hurmuzlu [61] measured the motion of a metal rod impacting a flat with a high speed camera at $1,000$ frames per second (fps). The velocities before and after the impact were calculated. The impact duration was measured with an electrical circuit. The work does not include the measurement of the motion of the rod during the impact. The electrical current between the objects can also affect the contact force, especially the friction force due to the welding mechanism. Minamoto and Kawamura [62] used a electrical circuit and calculated the impact duration and coefficient of restitution. Accelerometers can be used to measure the impact characteristics. They are commonly being used as impact detection sensors for robots. These sensors can be used to measure the contact force during the impact. However, they may change the surface characteristics.

Image processing techniques have been widely used to measure the motion of the impacting objects. Many studies such as Kharaz, Gorham, and Salman [63, 64, 65], Cermik

et al., [66] Ghaednia et al., [24, 55, 67, 68, 69], Marghitu et al., [70], Pfeiffer [71], Kardel et al., [72] were limited to the motion before and after the impact, and the coefficient of restitution was measured with image processing techniques. The main drawback of the simple image processing methods such as tracking an object [67, 24, 68] is one-pixel accuracy of the position measurements. However, one-pixel accuracy is not enough when dealing with an impact problem, since the displacement during the impact is usually smaller than one-pixel accuracy. Numerical derivations on the position can be used to calculate the velocity and acceleration (ultimately contact force), but this will decrease the accuracy significantly. Therefore, sub-pixel accuracy is needed for the image processing technique in order to increase the accuracy.

The motion of spheres such as different types of sports balls have been studied by many researchers. Laurent et al., [73] used a high speed camera to analyze the impact of spheres, but measurements were limited to before and after the collisions. They used edge detection and clustering technique in order to find the position of the spheres. They improved the accuracy with sub-pixel expansion. Goodwill et al., [74] studied the impact between a tennis ball and a racket and measured the ball rotation using an image processing technique [75]. The velocity and rotation of the ball before and after the impact were calculated automatically with a specialized software. Haake et al., [76] captured the motion of a tennis ball during the contact with a string-bed at high frequency. However, no information was obtained during the impact other than the contact time. Allen et al., [77] used a high speed camera in order to capture the impact of a tennis ball with a racket and compared the results with finite element simulations.

Cross [13, 78, 79] studied different types of sport balls in terms of their bouncing behavior. He used a video camera at low fps rate and calculated the rotation of the ball before and after the bounce. The impact behavior of different rubber balls was studied by Cross [27]. Grip and slip phases of the bounce were visually analyzed with a high speed camera. Cross [26, 80] studied the oblique impact of a hollow rubber ball and measured the angular

velocity of the ball during the impact. He used a manual image processing technique, which was limited to higher impact velocities. Rezaei et al., [32] studied oblique impact of a soccer ball and used a high speed camera in order to track the motion of the ball. The tracking of the ball was automatic. The accuracy was low, the error for the position of the center of the ball was 2 pixels, and no experimental result was obtained during the impact.

Digitial image correlation methods (DIC) are widely used for displacement, strain, and thermal expansion measurements [81, 82]. Although DIC methods are highly accurate and need a simple experimental setup, they are computationally expensive when used for several images. Digital image correlation methods have been started with the work of Peters and Ranson [83] with a pixel accuracy and later were improved by Sutton et al., [84] for sub-pixel accuracy with a method called the coarse-fine method. Although Sutton et al., used linear interpolation between pixels, the accuracy was not enough for the strain measurements. Later, Bruck et al., [85] introduced a revolutionary method by using the Newton-Raphson (NR) search method. They [85] used bi-cubic interpolation instead of bilinear interpolation. The accuracy and computational time of the method increased by an order of magnitude. Later, Davis and Freeman [86], and Jin et al., [87] developed the gradient method and the curve fitting method respectively. Both of the methods are faster than the NR method; however, they are less accurate. Chen et al., [88, 89] improved the accuracy of the NR method by using spline interpolation instead of bi-cubic interpolation. Pan et al. [90, 91, 92, 93, 94] developed several methods to decrease the computational time of NR-DIC and provided a complete review of DIC methods in details [81].

In this chapter, we focus on using the DIC method for collision problems. Impact problems have two main complexities for the image processing methods. First, there is a large number of frames to analyze, which increases the computation time significantly. Second, both large and very small displacements occur at the same time. Digital image correlation methods provide better accuracy for a video recorded with higher frequency. On the other hand, higher frequency requires longer computational time to process the videos.

A combination of spline interpolation used in [89] and Fast Fourier Transform (FFT) cross correlation methods [95, 96] usually used in Particle Image Velocimetery (PIV) is used. Fast Fourier Transform cross correlation has been employed to decrease the computation time. The spline interpolation has been used to get to sub-pixel accuracy and to capture small deformations during the impact. An analysis on the speckle pattern has also been done in order to increase the accuracy of the method. To the best of our knowledge, DIC methods have not been employed to calculate the motion during the impact. Our study can be considered one of the first works that shows the potential of the DIC methods to measure linear and angular velocities during the impact.

2.2 Method

The digital image correlation technique is used to calculate the displacement field on an image. The idea is to track a randomly generated pattern, called a speckle pattern. The speckle pattern is made on the objects by spraying white or black paint. Black ink has been used in this study to generate the speckle pattern on the objects. Later in this chapter, a short optimization of the speckle patterns will be discussed. We use black and white images, where an 8-bit number is assigned to each pixel. The image is divided into square or circular interrogation windows depending on the type of study. Spline interpolation has been used to increase the accuracy from pixel to sub-pixel. Figure 2.1 shows an example of a spline interpolation for a 15×15 pixel interrogation window. A spline interpolation with 5 extra points in the middle of each two pixels has been shown in Fig. 2.1(b). Although the accuracy of the method is improved by increasing the number of extra points for the interpolation, the computation time increases drastically. Figure 2.2 shows the computation time versus the number of extra points in the interpolation; therefore, one should find a balance between the desired accuracy and the computation time. The computation time shown in Fig 2.2 is very short because the analysis is done only for one interrogation window. For a real impact problem, hundreds of interrogation windows and frames are required to be analyzed.

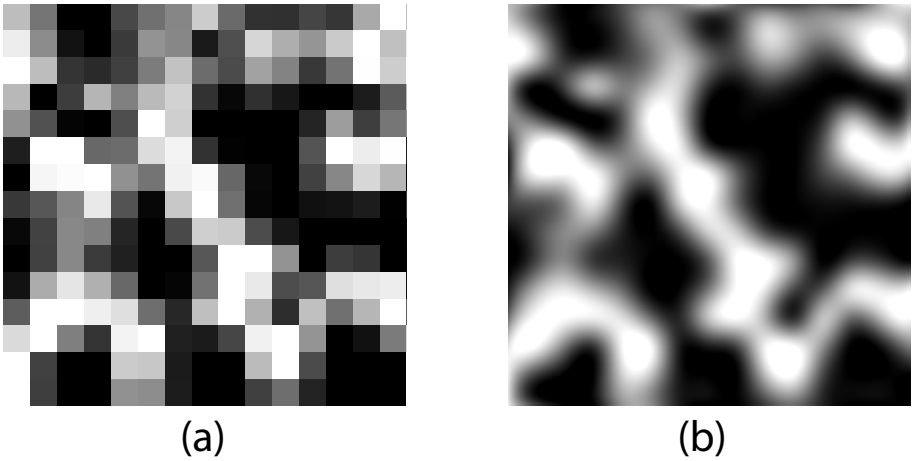

Figure 2.1: Spline interpolation for a 15×15 pixel interrogation window: (a) the original image, (b) spline interpolation with 5 extra points in between pixels.

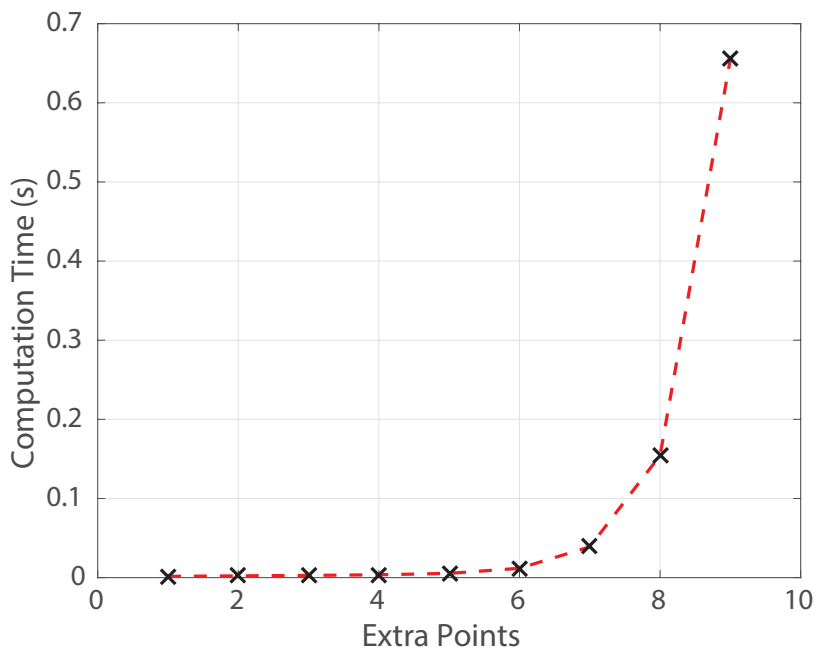

Figure 2.2: Computation time versus the number of extra points in the interpolation for a 15×15 pixel interrogation window shown in Fig. 2.1.

Next, FFT cross correlation [95, 96] has been implemented for each of the interrogation windows to find the displacement of the center for each window during the next frames. Details of the methods have been discussed in the following sections for each of the examples.

Finding the velocity field is not enough to track a certain point on an object. To study the motion of a sphere, one needs to measure the velocity of the centroid of the sphere. The

position of the centroid of the sphere must be known and then used along with the velocity field (measured by the DIC method). A combination of the position tracking method along with the DIC method is needed. The Hough transform [97, 98] method is one way to track the positions of the objects. In this work, the Hough transform method has been used to track the position of the centroid of the sphere, and the velocity of the centroid has been found using the velocity field calculated by the DIC method.

2.3 Speckle pattern analysis

To validate the image processing method code for the linear and angular motion, a video generator has been made. A picture of the object has been used in the generator to make a video with known angular velocity and linear motion of the centroid of the ball. Later, the generated video is analyzed using the DIC method to validate the method and its implementation. The speckle pattern on the objects is another important parameter to be analyzed. There are a few studies [99, 100, 101, 102] for the speckle pattern for strain measurements, but to our best knowledge, there is no comprehensive study on the speckle pattern for the dynamic problems such as impact where large and small displacements and rotations can be observed together.

Figure 2.3 shows six different patterns that have been used for the speckle pattern study. Tennis balls (a)-(d) and lacrosse balls (e) and (f) have been painted with black ink. Patterns (a-d) show four different speckle sizes with three different densities from I to III. In order to maintain the simplicity, we will reference each ball by their indexes represented in Fig. 2.3. For example, Fig. 2.3 (a)I will be called as ball (a)I. Balls (e) and (f) show the combination of different sizes of speckles. Balls (f) also have a few straight lines in addition to the speckles. The images have been captured with a high speed camera at 10,000 fps, which was used for the experiments.

The speckles on balls (a) have an average area of 4 pixels with different densities of dark pixels, with I being 9%, II being 17%, and III being 24%. For balls (b), the average area

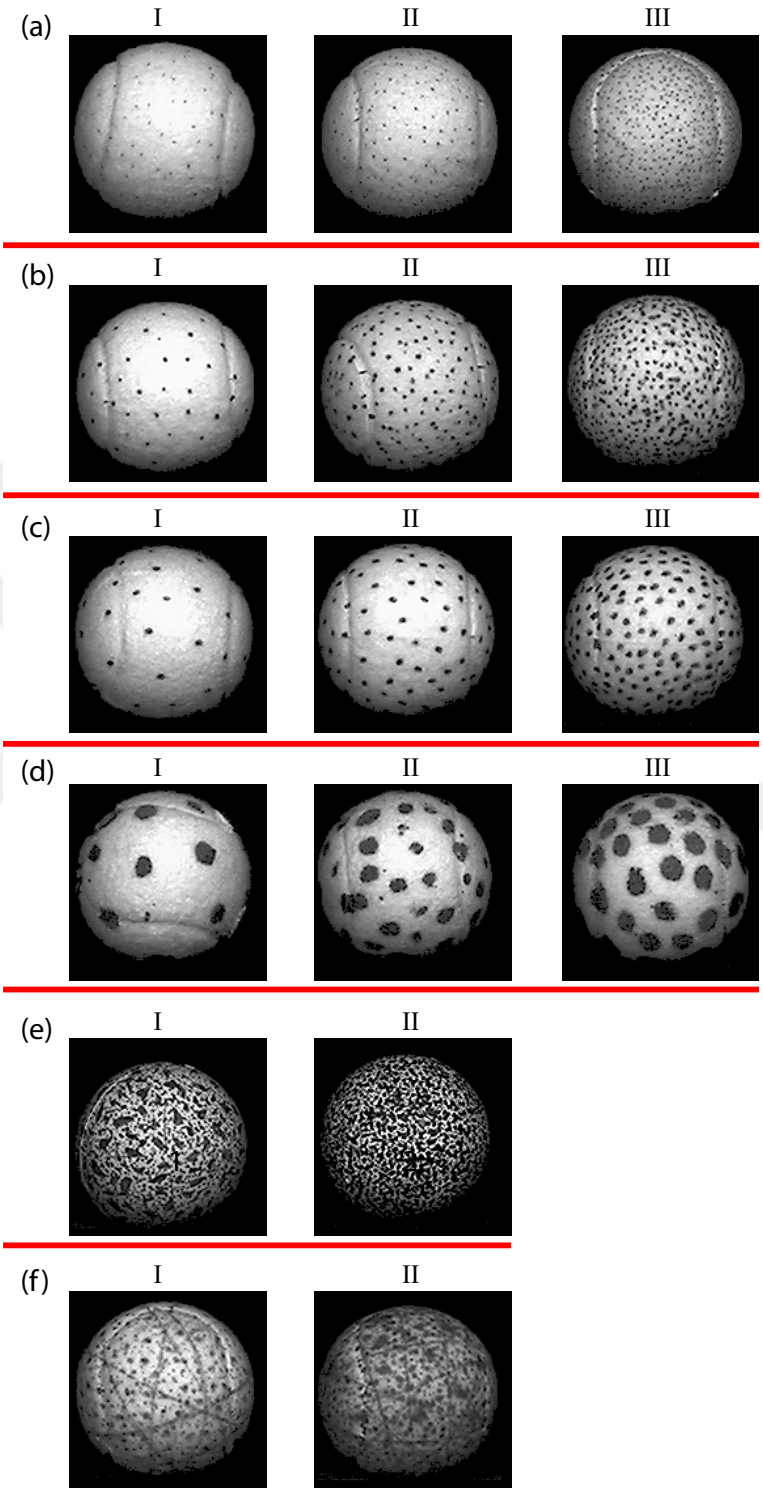

Figure 2.3: Speckle patterns used in this study; (a) to (f) show different speckle patterns and indexes I to III show different densities for each speckle pattern with I and III being the least and most dense, respectively.

of the speckles is 10 pixels with densities 13%, 19%, and 31% for I, II, and III, respectively. Balls (c) have an average speckle area of 20 pixels with densities 14%, 18%, and 27% for I, II, and III, respectively. Balls (d) have an average speckle area of 250 pixels with densities 22%, 30%, 43% for I to III, respectively.

Ball (e)I has a combination of different speckle sizes from 4 to 80 pixels with density of 54%. The combination of speckles areas is from 2 to 40 pixels for the ball (e)II. The shape of the speckles for balls (e) are also random, unlike the circular shape for the other balls. Ball (f)I has different sizes of speckles ranging from 4 to 20 pixels with 27% density. Speckles from 4 to 80 pixels with density of 52% are used for the ball (f)II. The balls shown in Fig. 2.3 have been used along with the video generator to analyze four different motions: translation in one direction, translation in two directions, pure rotation, and general motion.

The first case is the translation in one direction with a velocity, $\vec{v} = 1\hat{\imath}$ pixel/frame. The video is 1 fps. The frequency and the displacement rate are the same for the following cases as well. Figure 2.4 shows the mean absolute error of the displacement rate measurement for all of the balls. Balls (e)I and (e)II show the least errors with 0.01 and 0.02 pixel/frame, respectively. Ball (d)III has the largest error as expected due to the size and density of the speckles. Balls (a)III, (a)II, (b)II, (b)III, (f)I, and (f)II show around 0.1 pixel/frame error.

The second case is the translation in two directions with velocity, $\vec{v} = 1\hat{\imath} + 1\hat{\jmath}$ pixel/frame. Figure 2.5 shows the mean absolute error of the displacement rate for this translation case. Ball (e)I shows the least error with 0.016 and 0.037 pixel/frame in X and Y directions, respectively. Balls (e)II and (a)III also show acceptable errors. Balls (d)I-III show the largest error, which is similar to the first case. There is a trend in the results that the accuracy increases as the density of the dark pixels increases for the balls (a), (b), (c), and (f). On the other hand, the accuracy decreases as the density increases for the balls (e). As explained before, the velocities are calculated for the centroid of the balls, and the centroid of the ball itself is calculated by the Hough transform method. The accuracy of the Hough transform method decreases as the number of speckles increases, because the speckles are disrupting

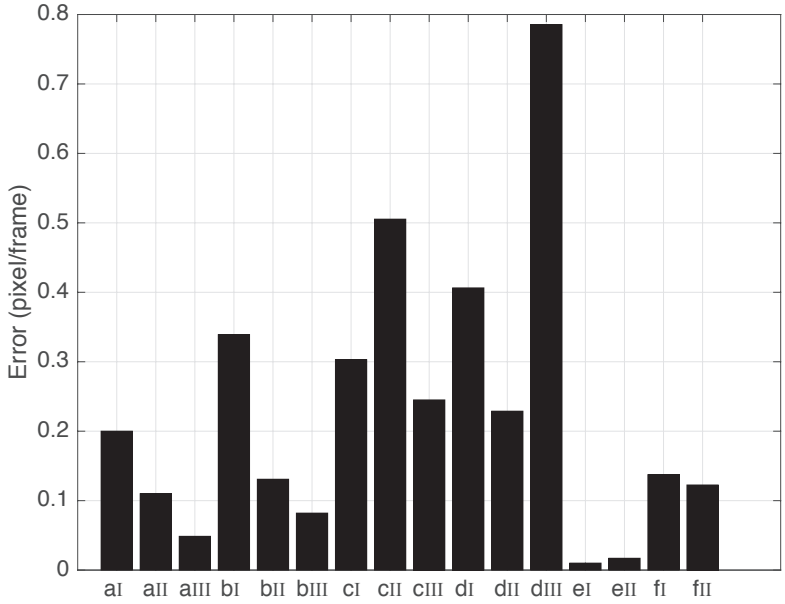

Figure 2.4: Speckle pattern study for the translation in one direction.

the edges of the ball. Therefore, one should consider that there is a balance between the accuracy of the measurements and the density of the speckles.

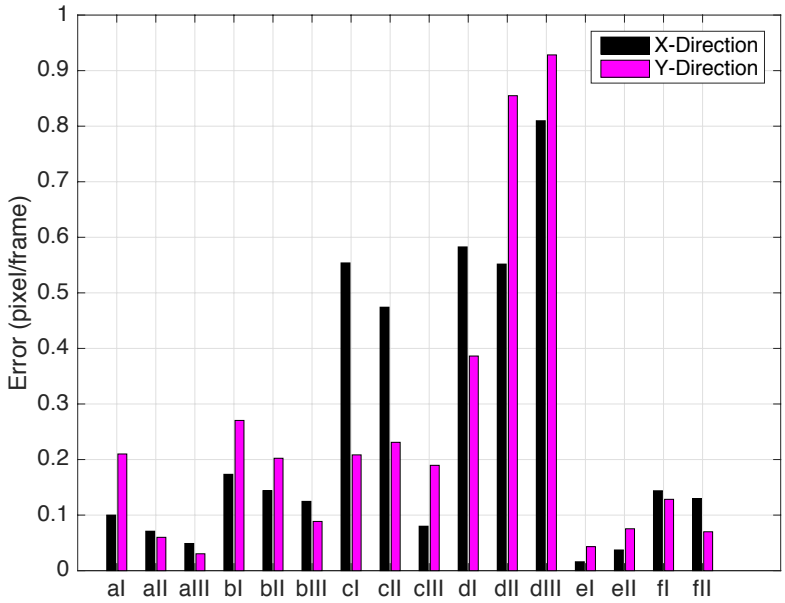

Figure 2.5: Speckle pattern study for the translation in two directions.

The third case is pure rotation of the ball with an angular velocity, $\vec{\omega} = 3\hat{k}$ deg/frame. Figure 2.6 shows the mean absolute error of the rotation measurement in deg/frame. By neglecting the deformations on the ball during the impact, the ball can be assumed as a rigid body. The relative velocity of any two interrogation windows, measured from the velocity field, can be used to calculate the angular velocity. The rotation has been calculated from the velocity field by solving and averaging omega for all of the interrogation windows on the ball. Ball (e)I shows the least error with 0.1 deg/frame. One should consider that 3 deg/frame is a relatively small rotation, and 0.1 deg/frame is an acceptable accuracy.

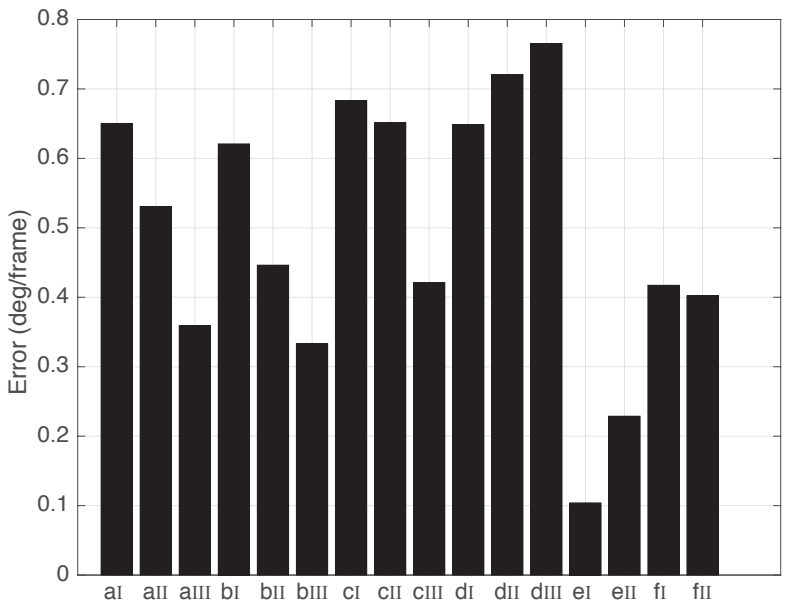

Figure 2.6: Speckle pattern study for pure rotation.

Using circular or ring interrogation windows is another method to calculate the rotation. This method is applied to one of our experimental studies. It has been shown in this study that ring-shape interrogation windows can be a good alternative for some cases.

The final case is the general motion with linear velocity, $\vec{v} = 1\hat{\imath} + 1\hat{\jmath}$ pixel/frame, and angular velocity, $\vec{\omega} = 3\hat{k}$ deg/frame. Figure 2.7 shows the mean absolute error of the displacement rate and rotation measurement for all of the balls. The error for linear motion

and the rotation are shown in pixel/frame and in deg/frame, respectively. It can be seen that

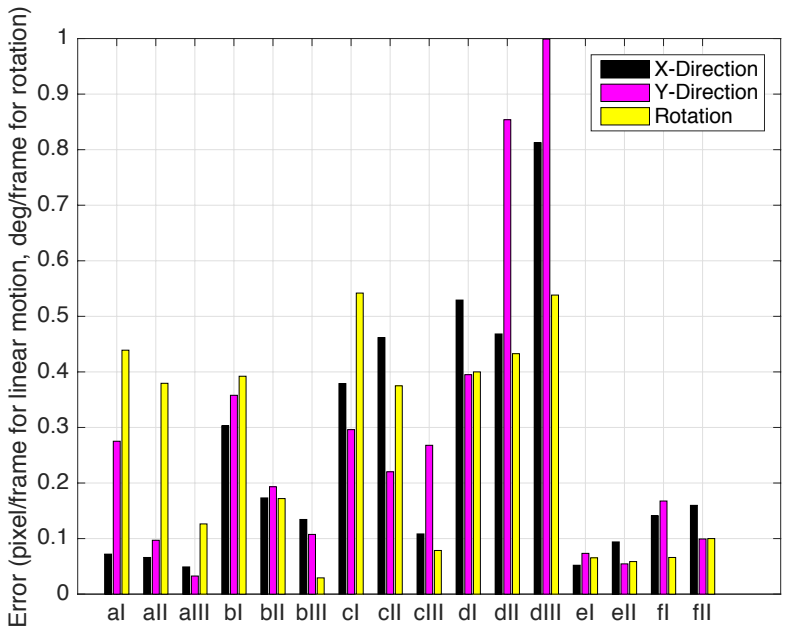

Figure 2.7: Speckle pattern study for the general motion.

balls (e) and (f) perform better than the other balls for this case especially for the rotation. The existence of linear motion and rotation causes the balls to undergo large and small displacements on different locations of the balls. For example, if the centroid of the ball has a velocity on the positive horizontal direction, and the angular velocity is counterclockwise, the top of the ball will have small displacements, and the bottom of the ball will undergo larger displacements. The bigger speckles help with the larger displacements, while the smaller speckles help with the small displacements. The same result can also be seen for the ball (b)III, which contains mid-size speckles. Although the error for this ball compared to the other balls for the previous cases was large, it shows good results especially for the rotation, and for the general motion. Balls (a) ,which have shown a good accuracy for the previous cases, show relatively large errors, especially for the rotation.

Overall, balls (e)I and (f)II show more consistent results. These balls contain a combination of speckle sizes from 4 to 20 pixels. Balls (f) include random thin (2 pixels width)

lines which can help with the ring interrogation DIC method. Balls (e)I and (f)II have been used in our experiments.

2.4 Experiments

Generally, two different conditions are used for the ball impact experiments; low speed impacts and high speed impacts. Low speed impacts are easily achieved by the drop method using gravity to accelerate the ball from a desired height. High speed impacts have been used to reflect real sport conditions, and this requires advanced custom devices such as cannon or pitching machine. The drop method has been used broadly because of its simplicity, but provides limited velocity range. This method has been applied for our experimental studies.

Two different impact cases have been experimentally analyzed with the image processing method: the oblique impact of a tennis ball with a racket and the oblique impact of a lacrosse ball with a wooden flat. The image processing method has been used to measure the linear and angular velocities of the ball during the impact with a high accuracy. Each of the two cases has its own unique challenge that we tried to overcome. Part of the tennis ball becomes invisible during the impact due to the racket frame, and this affects the accuracy. While the ball undergoes a very small deformation, the racket strings have a larger deformation. For the the oblique impact of the lacrosse ball, the flat is rigid and the ball undergoes small deformation due to low impact velocities.

Two very similar experimental setups have been used for the experiments as seen in Fig. 2.8 and Fig. 2.9. Each ball has been released without the initial angular velocity. The impacts have been captured with a high speed camera at 10,000 fps. Projectors with 1000 W provide essential light for the high speed camera. The schematic of the experimental setup for the impact of the tennis ball with a racket is shown in Fig. 2.8. Tennis balls with a diameter of, D, 67 mm and a mass of, m, 56.7 gr have been used for the experiments. A robotic arm has been used to hold and release the tennis ball from a desired height for consistent drops. The racket has been clamped to a massive supporting device which was

clamped to the table to reduce the vibrations during the impact. The camera is placed horizontally 0.8 m from the collision plane. The impact angle, β, is the angle of the tennis racket with the horizontal axis and is controlled by a tripod. The ball with speckle pattern (f)I has been used for the experiments.

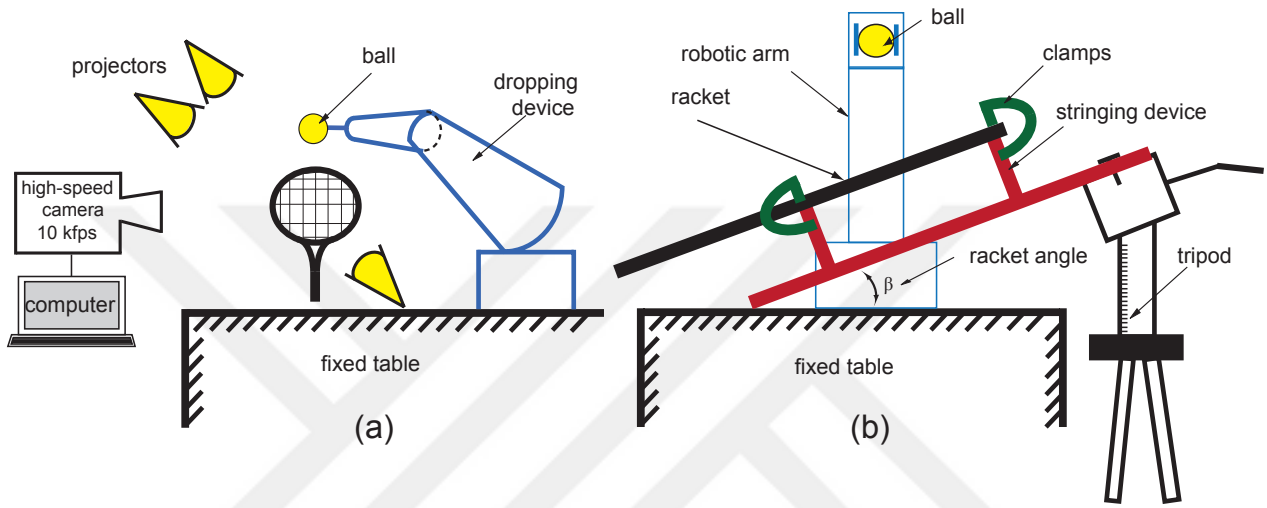

Figure 2.8: Experimental setup for the impact of the tennis ball with the racket: (a) front view, (b) right view.

Figure 2.9 shows the schematic of the experimental setup for the impact of the lacrosse ball with a wooden flat. The lacrosse ball has a diameter of 63.25 mm and a mass of 145.66 gr. To perform consistent drops from a desired initial height, a dropping device with a solenoid has been used to hold and release the ball. A small piece of a ferromagnetic metal with negligible weight has been glued to the top of the ball in order to attach the ball to the dropping device. The wooden flat has been clamped to a massive metal flat which is attached to a tripod that controls the impact angle. The metal flat has been fixed to the table to reduce the vibration during the impact. The impact angle is measured from the horizontal axis.

2.4.1 Oblique impact of a tennis ball with a racket

The ball (f)I with speckle pattern shown in Fig. 2.3 has been used for the experiments. Figure 2.10 shows the image processing procedure for tracking the centroid of the ball,

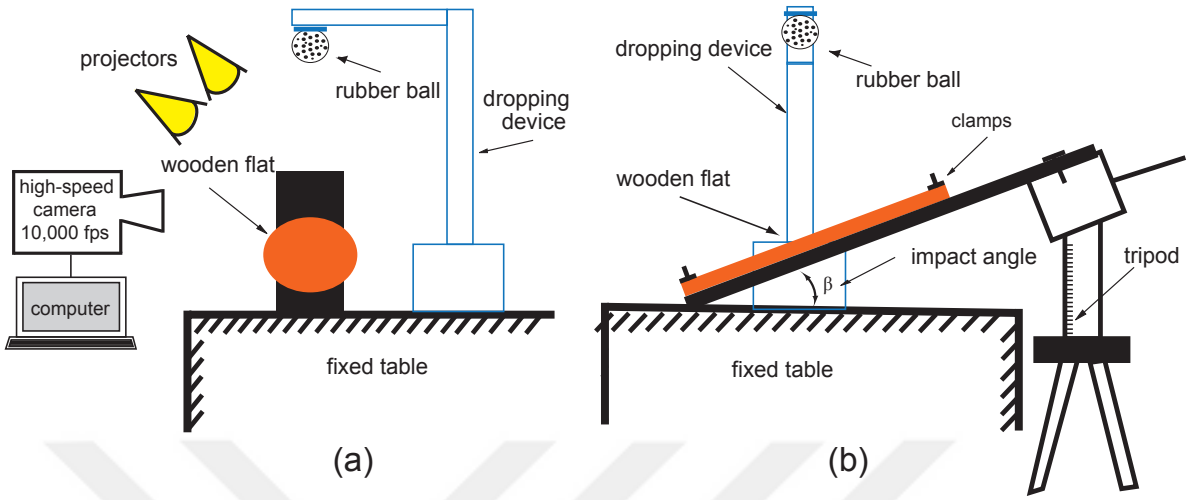

Figure 2.9: Experimental setup for the impact of the lacrosse ball with a wooden flat: (a) front view, (b) right view.

measuring the velocity field and rotation. The pictures on the left and on the right show the original images and the images with measured velocity field using the DIC method, respectively. The Hough transform method has been used to find the boundary and track the centroid of the ball even though part of the ball becomes invisible due to the racket frame. The accuracy of the DIC method, especially for rotation measurements, decreases when part of the ball is covered by the racket frame.

Figure 2.10(a) depicts the ball at the beginning of the impact. The boundary and centroid of the ball are found by the Hough transform method. The right picture in Fig. 2.10(a) shows the velocity field measured by the DIC method at the beginning of the impact. The surface of the ball has been changed to pure white to show the velocity field. The picture has been divided into 15×15 square interrogation windows. The center of each interrogation window is represented with a diamond shaped marker. The velocity at the center of each of the interrogation windows has been calculated and represented with a line in the picture (the length of each line is the scaled displacement of the center of each interrogation window). Each line starts from the center of the interrogation windows and shows the displacement

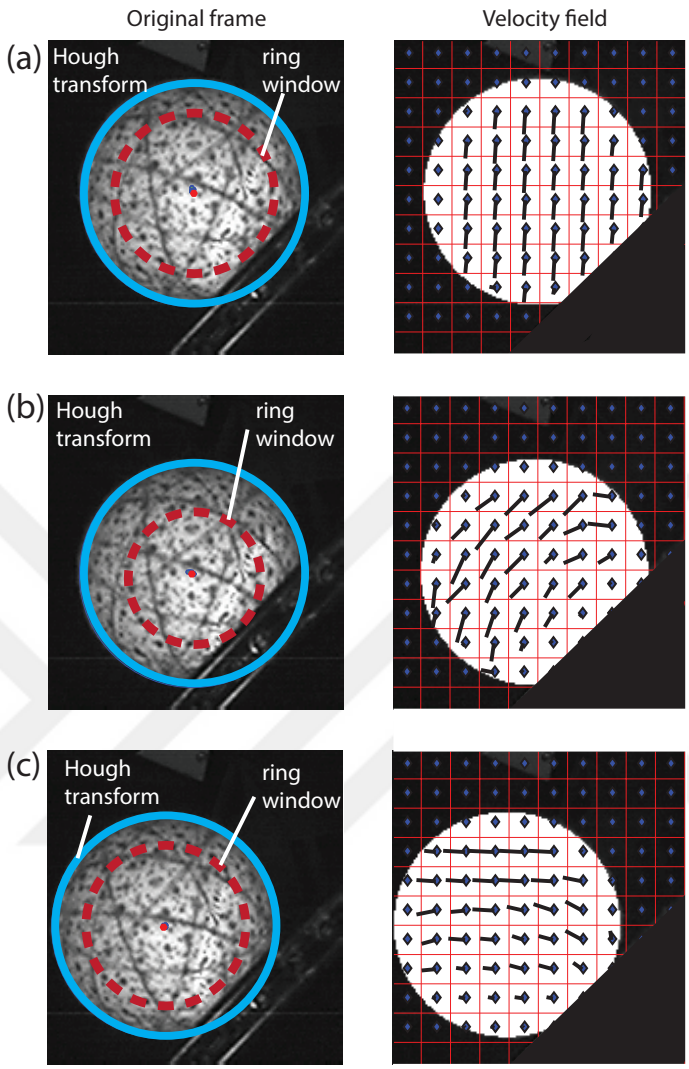

Figure 2.10: Original frames and the velocity field of the impact of a tennis ball with a racket calculated by DIC: (a) the beginning of the impact , (b) during the impact, (c) the end of the impact.

of that window during the next time interval. The velocity field shows constant downward velocity for all of the windows at the beginning of the impact, which is as expected.

There are two different ways that can be used for the rotation measurements. First, the angular velocity can be calculated from square interrogation windows by averaging all of the interrogation windows. The second way is to use a circular interrogation window placed at the centroid of the ball as shown in Fig. 2.10(b). The radius of this ring interrogation window is the distance from the centroid of the ball to the edge of the racket. The radius

of the circular interrogation window shrinks during the impact as the larger part of the ball hides behind the racket, as seen in Fig. 2.10(b). It was observed that the circular interrogation window DIC is working better than averaging the angular velocity for the square interrogation windows. This may be due to the fact that during the impact, a part of the ball is hidden behind the racket. The two-points spline interpolation has been used to increase the accuracy. It was observed that adding lines to the speckle pattern increases the accuracy of the DIC method with the circular interrogation window.

Figure 2.10(b) shows the tennis ball during the impact. Same as Fig. 2.10(a), the Hough transform method is used to find the boundary, and centroid of the ball and the circular interrogation window is used for the rotation measurement. The right picture in Fig. 2.10(b) shows the velocity field during the impact. The velocity field shows smaller values for the points close to the contact point and larger values as it gets further from the contact point, which shows the rotation of the ball during the impact. Figure 2.10(c) shows the velocity field at the end of the impact. The velocity field clearly shows the bounce and the counter clockwise rotation.

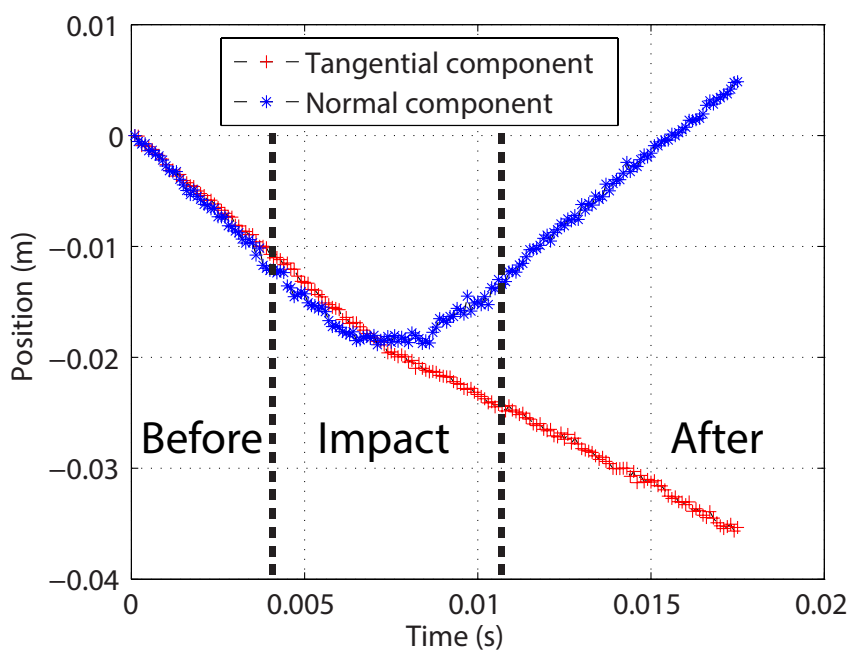

Figure 2.11: Position of the centroid of the tennis ball measured by Hough transform method.

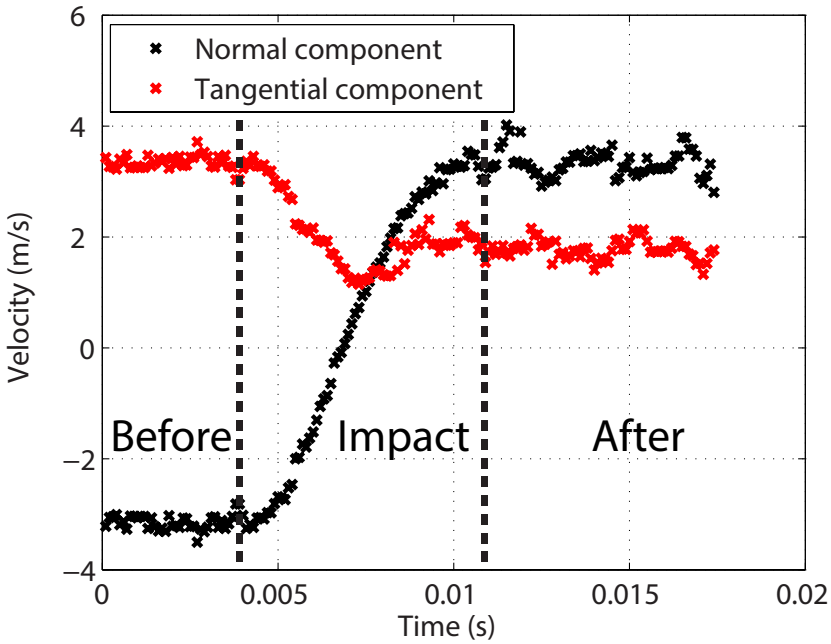

Figure 2.12: Velocity of the centroid of the tennis ball with the DIC method.

Figure 2.11 depicts the position of the centroid of the tennis ball for an impact with the angle $\beta = 45°$. The position of the centroid of the ball before, during, and after the impact has been measured by the Hough transform method, which shows acceptable results. However, the first derivation of the position of the centroid of the ball to calculate the velocity of the centroid of the ball is found to be very noisy. Therefore, the DIC method is used to calculate the velocity of the centroid of the tennis ball. Figure 2.12 presents the measured velocity before, during, and after the impact. Impact starts with initial velocity $\mathbf{v}_C(t_i) = 3.2\mathbf{\imath} - 3.2\mathbf{\jmath}$ m/s. From the normal component of the velocity, it can be seen that the impact starts at $t_i = 4$ ms. The restitution phase starts at $t = 7$ ms and ends at $t_f = 10$ ms.

Figure 2.13 shows the angular velocity of the ball during the same impact as seen in Figs. 2.11 and 2.12. The DIC method with circular ring interrogation is used for the rotation measurements. Although there is some noise in the measurements, the results are acceptable to be used for the analysis. The noise is due to low resolution of the high speed camera.

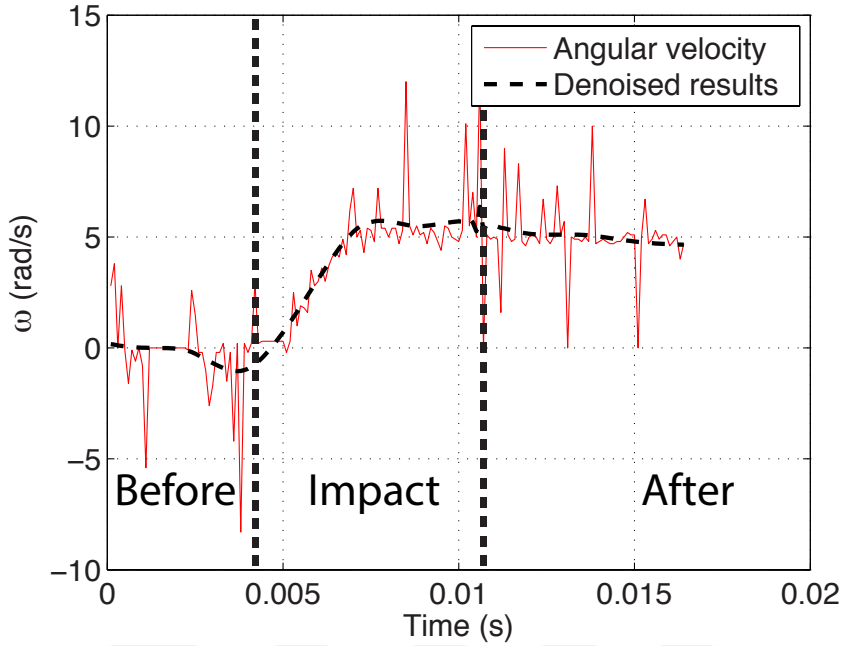

Figure 2.13: Angular velocity of the tennis ball measured by the DIC method.

2.4.2 Oblique impact of a lacrosse ball with a wooden flat

Figure 2.14 depicts the analysis procedure for the impact of a lacrosse ball with a wooden flat. The camera has been tilted such that the flat lays on the horizontal axis for the experiments. This change provides a higher number of pixels in the vertical direction. Same as previous analysis, the Hough transform method has been used to track the centroid of the ball throughout the impact. The ball undergoes small elastic deformations during the impact which affect the accuracy of the Hough transform method. The digital image correlation method with 5 points spline interpolation is used in order to find the velocity field on the surface of the ball with the assumption of no out of plane motion.

The Hough transform method works better with some improvements on the image. To improve the accuracy of the Hough transform method, the boundary of the ball has been found and changed to a different color, and a filter has been applied to the ball. Because of the sharp difference between the boundary and the ball, the method is able to measure the radius of the ball easier. Figure 2.14 (a) shows the images at the beginning of the impact.

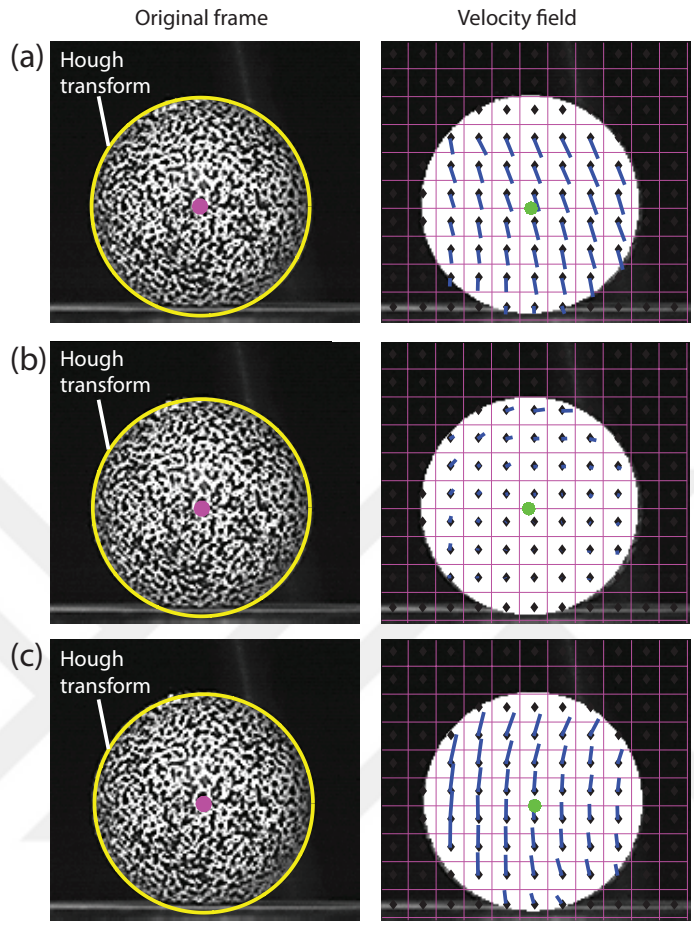

Figure 2.14: Original frames and the velocity field of the impact of a lacrosse ball with a wooden flat calculated by DIC: (a) the beginning of the impact, (b) during the impact, (c) the end of the impact.

Both the boundary of the ball and velocity field can be seen in the images. Figure 2.14(b) shows the velocity distribution on the ball during the impact calculated with the DIC method with 5 points spline interpolation. The camera is tilted 20° to match the local coordinates. There is larger velocity field on the top left of the ball and smaller on the bottom right as seen in Fig 2.14(b). The velocity field shows a clockwise rotation as expected.

The position of the centroid of the lacrosse ball is seen in both the tangential and normal directions in Fig 2.15. The hough transform method is used for the measurements. The normal component of the position of the centroid of the ball decreases until the maximum compression, and then increases for the rest of the impact. The maximum compression occurs nearly at $t = 3.7$ ms. The tangential component of the position of the ball increases

during the impact where the increase rate before the impact is larger than after the impact. The total displacement shown in the figure is small, about 4 mm. Although the accuracy of the method is acceptable for the position analysis, the first derivation for the velocity will result in significant noise.

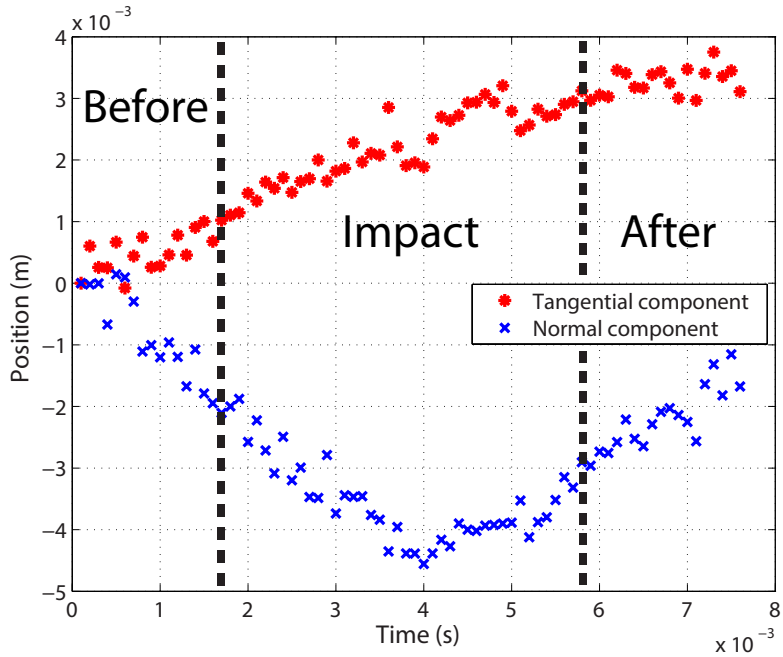

Figure 2.15: Position of the centroid of the lacrosse ball measured by Hough transform method.

The velocity of the centroid of the ball has been found by interpolation of the velocity field calculated by the DIC method. The centroid of the ball is found with the Hough transform method. Figure 2.16 shows the results in both normal and tangential directions. The collision starts around $t_i = 1.4$ ms. At this instant, the normal velocity starts increasing until $t_f = 5.8$ ms. The initial velocity before the impact is $\mathbf{v}_C(t_i) = 0.57\mathbf{\imath} - 1.69\mathbf{\jmath}$ m/s. The maximum compression occurs at $t = 3.7$ ms, and the result matches with the position analysis shown in Fig 2.15. The velocity after the impact is $\mathbf{v}_C(t_f) = 0.28\mathbf{\imath} + 1.39\mathbf{\jmath}$. The tangential component of the velocity decreases until $t = 4.3$ ms and then increases at a very low rate till the end of the impact.

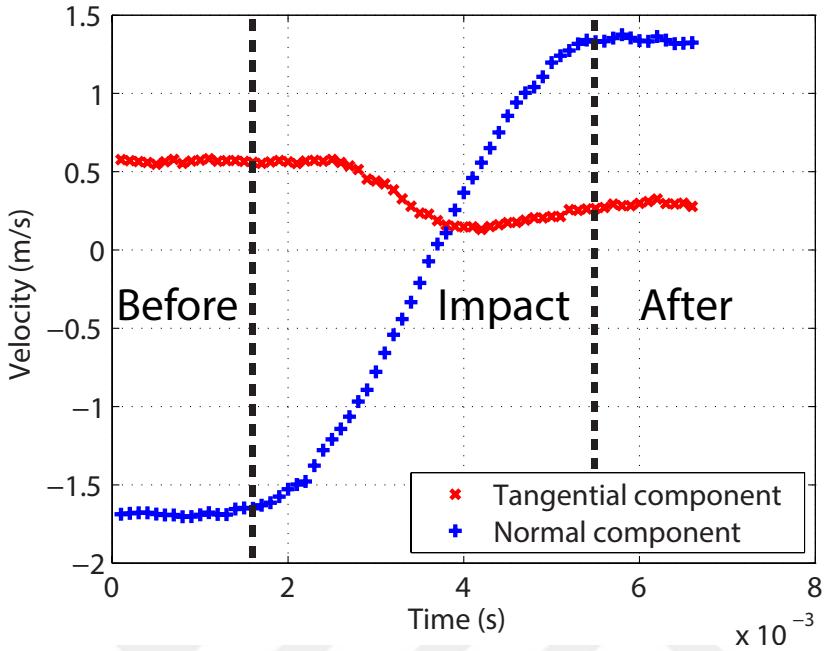

Figure 2.16: Velocity of the centroid of the lacrosse ball with the DIC method.

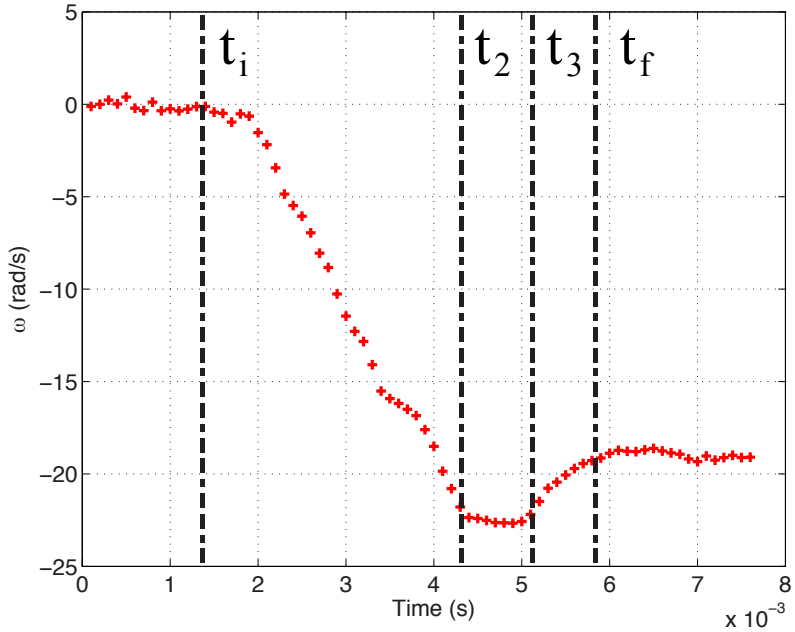

Figure 2.17: Angular velocity of the lacrosse ball measured by the DIC method.

The angular velocity of the ball during the impact has been measured with the DIC method. The relative velocity of any two interrogation windows, measured from the velocity

field, are used to calculate the angular velocity. The rotation has been calculated from the velocity field by solving and averaging all omega results from all of the interrogation windows on the ball. The angular velocity of the ball during the impact is shown in Fig. 2.17 for the same experiment. The impact starts at around $t_i = 1.4$ ms. The magnitude of the angular velocity increases until $t_2 = 4.3$ ms, then stays constant for a short time and decreases until the end of the impact at $t_f = 5.8$ ms.

2.5 Conclusion

A new implementation of the DIC method for the impact problems has been presented. The method measures the linear and angular motion of the spheres. A study has been done to see the effect of the speckle pattern on the accuracy of the DIC method.

Two different experiments have been studied: the oblique impact of the tennis ball with a racket and the oblique impact of a lacrosse ball with a wooden flat. The Hough transform method has been used to track the centroid of the balls. The digital image correlation method is used to find the linear and angular velocities of the balls before, during, and after the impact. The circular interrogation window is used for the tennis ball impact in order to calculate the angular velocity of the ball, while square windows are used for the lacrosse ball experiments.

It has been shown that the DIC method is able to capture the characteristics of the impact. The accuracy can be improved by a high speed camera with better resolution and higher frequency. In the next two chapters, the experimental results obtained from the DIC method are used to understand the nature of the normal and tangential forces during the impact.

Chapter 3

Impact of a hollow ball with a flexible flat

The impact of a tennis ball has been studied experimentally and theoretically many times over the last four decades. Three different setups have been used in order to model the impact of the tennis ball: the ball impacts a court, a clamped racket or a freely suspended racket. Two important physical characteristics of the impact, the coefficient of restitution and the coefficient of friction, have been studied. In this chapter, a hollow ball (tennis ball) impacting a flexible surface (tennis racket) is studied.

3.1 Dynamics of the ball

Consider the impact between the tennis ball and the string-bed as shown in Fig.3.1. The angle of the string-bed with the x_0 horizontal axis, is β. The tennis ball is considered as a sphere of radius R with the mass center at C. The mass of the ball is m. The contact point between the ball and the string-bed is E.

A global reference frame of unit vectors $[\,\mathbf{\imath}_0, \mathbf{\jmath}_0, \mathbf{k}_0]$ and a local reference frame, with the origin at E, of unit vectors $[\mathbf{\imath}, \mathbf{\jmath}, \mathbf{k}]$ are considered as shown in Fig.3.1. The $x-$axis is tangential to the string-bed and the $y-$axis is perpendicular to the string-bed.

To characterize the instantaneous configuration of the ball, the generalized coordinates q_1, q_2, and q_3 are employed. The generalized coordinate q_1 denotes the displacement of the contact point along $x-$axis, the generalized coordinate q_2 denotes the displacement of the contact point along $y-$axis and q_3 is the radian measure of the rotation of the ball.

The position vector of the impact point E is

$$\mathbf{r}_E = q_1\,\mathbf{\imath} + q_2\,\mathbf{\jmath}, \tag{3.1}$$

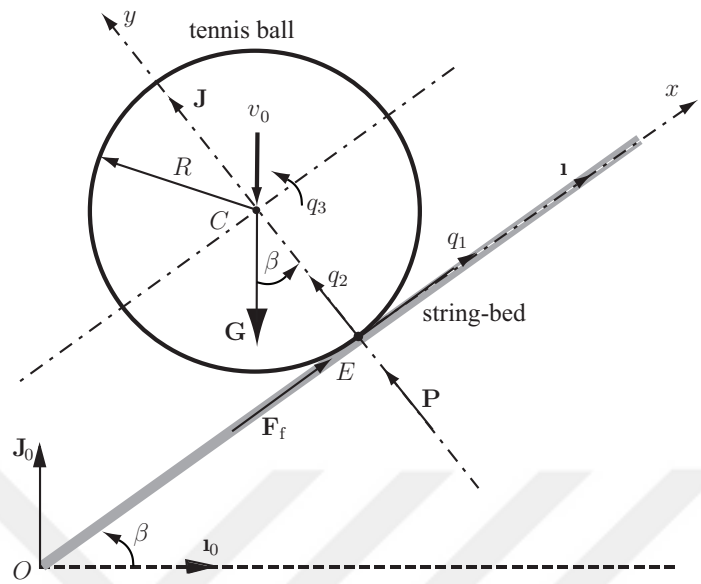

Figure 3.1: Tennis ball in contact with the string-bed.

and the position vector of the centroid, C is

$$\mathbf{r}_C = q_1\,\mathbf{ı} + (q_2 + R)\,\mathbf{ȷ}. \tag{3.2}$$

The angular velocity and acceleration of the ball are

$$\boldsymbol{\omega} = \dot{q}_3\,\mathbf{k} \quad \text{and} \quad \boldsymbol{\alpha} = \ddot{q}_3\,\mathbf{k}. \tag{3.3}$$

The linear velocity and acceleration of the mass center, C are

$$\mathbf{v}_C = \mathrm{d}\,\mathbf{r}_C/\mathrm{d}\,t \quad \text{and} \quad \mathbf{a}_C = \mathrm{d}^2\mathbf{r}_C/\mathrm{d}\,t^2. \tag{3.4}$$

The linear velocity and acceleration of the impact point E are

$$\mathbf{v}_E = \mathbf{v}_C + \boldsymbol{\omega} \times \mathbf{r}_{CE} \quad \text{and} \quad \mathbf{a}_E = \mathbf{a}_C + \boldsymbol{\alpha} \times \mathbf{r}_{CE} + \boldsymbol{\omega} \times (\boldsymbol{\omega} \times \mathbf{r}_{CE}), \tag{3.5}$$

where $\mathbf{r}_{CE} = \mathbf{r}_E - \mathbf{r}_C$.

The compression of the local contact region produces a reaction force. The contact force starts when the ball touches the string-bed. The normal contact force, P, acts at point E and is in y direction. The friction force is in the opposite direction of the tangential velocity of the ball. Figure 3.2 shows the sketch of the impact model for the ball on a surface. The impact has two phases: compression and restitution.

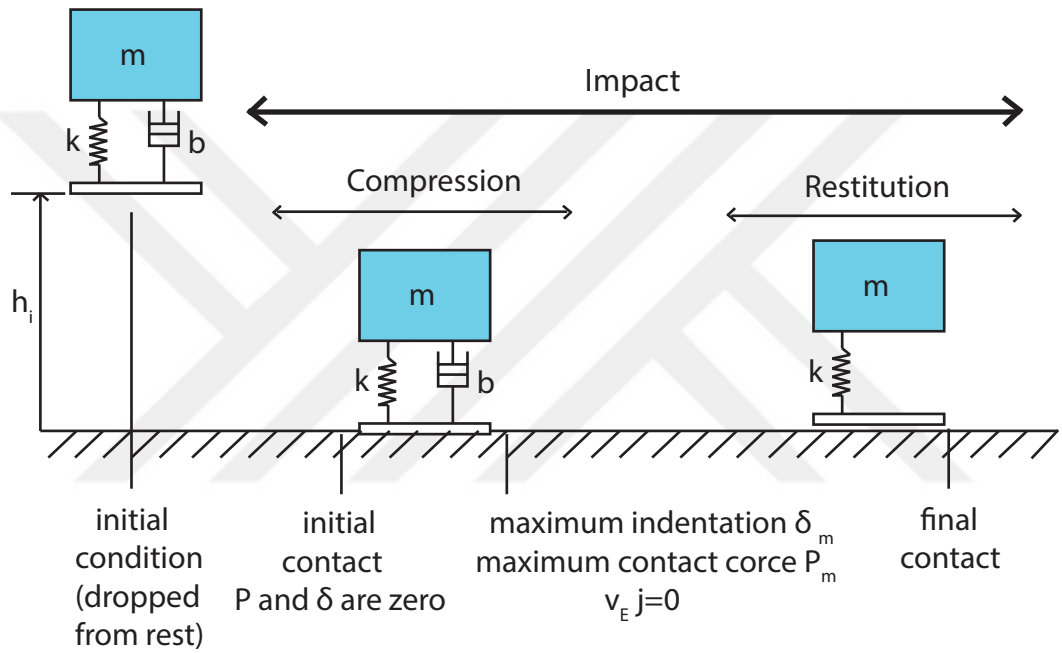

Figure 3.2: The sketch of the impact model.

3.1.1 Compression Phase

The first phase of the impact is the compression. The phase starts with the moment when the ball initially contacts the string-bed. At the beginning of the compression phase, the normal impact force, P, and the indentation, δ, are zero. The impact force acts upward alongside the $y-$axis, as shown in Fig. 3.1 and has the expression $\mathbf{P} = P\,\mathbf{j}$. The magnitude of the normal force is given by,

$$P = k\,\delta - b\,\dot{\delta}, \tag{3.6}$$

where $\delta = q_2(t)$ is the normal elastic displacement during the compression, and k and b are coefficients of the contact force.

The total force at point E is

$$\mathbf{T} = F_f\,\mathbf{\imath} + P\,\mathbf{\jmath}, \tag{3.7}$$

where F_f represents the friction force that is opposite to the tangential component of the velocity of the contact point of the ball. For the particular case of the tennis ball in Fig. 3.1 the tangential component of the velocity has a negative sign.

The friction force is given by,

$$\mathbf{F}_f = \mu\,P\,\mathbf{\imath}, \tag{3.8}$$

where μ is the kinetic coefficient of friction .

For the case of a rigid ball, the equations of motion are

$$\begin{aligned} m\,\mathbf{a}_C &= \mathbf{G} + \mathbf{T}, \\ I_C\,\boldsymbol{\alpha} &= \mathbf{r}_{CE} \times \mathbf{T}, \end{aligned} \tag{3.9}$$

where $\mathbf{G} = -m\,g\,\sin\beta\,\mathbf{\imath} - m\,g\,\cos\beta\,\mathbf{\jmath}$, is the weight of the ball, I_C is the mass moment of inertia about C, and $g = 9.81$ m/s^2 is the gravitational acceleration.

The initial conditions for compression phase are:

$$\begin{cases} q_1(t_0) = q_{10}, & \dot{q}_1(t_0) = -v_0\,\sin\beta, \\ q_2(t_0) = q_{20}, & \dot{q}_2(t_0) = -v_0\,\cos\beta, \\ q_3(t_0) = q_{30}, & \dot{q}_3(t_0) = 0. \end{cases}$$

The final values of $q_i(t_m)$ and $\dot{q}_i(t_m)$ for the compression phase will be the initial conditions for the restitution phase. This phase ends at maximum compression when the normal component of the velocity of the contact point of the ball, $\mathbf{v}_E \cdot \mathbf{\jmath} = 0$. The maximum indentation is δ_m, which corresponds to the maximum compression, and the maximum normal force is P_m.

3.1.2 Restitution Phase

The restitution phase starts at the moment of maximum compression. The ball is pushed by the surface upward. During this phase, the contact force decreases from the maximum value, P_m, to zero. It is assumed that the recovery is fully elastic as it has been proved in contact mechanics field [42, 50, 56, 103, 104], and the normal force for the restitution is

$$P = k\,\delta. \tag{3.10}$$

The total force for the elastic restitution is $\mathbf{T} = F_f\mathbf{i} + P\,\mathbf{j}$. The equations of motion for this case are solved for the initial conditions at maximum compression:

$$\begin{cases} q_1(t_m) = q_{1m}, & \dot{q}_1(t_m) = v_{xm}, \\ q_2(t_m) = \delta_m, & \dot{q}_2(t_m) = 0, \\ q_3(t_m) = q_{3m}, & \dot{q}_3(t_m) = \omega_m. \end{cases}$$

The equations of motion are given by Eq. (3.9). The differential equations of the motion have been solved with MATLAB. At the end of restitution phase, $t = t_f$, the rebound velocity of point E is $\mathbf{v}_E(t_f)$. The restitution phase will end when the contact force is zero. The coefficient of restitution is calculated as

$$e = |\mathbf{v}_E(t_f) \cdot \mathbf{j}/\mathbf{v}_E(t_0) \cdot \mathbf{j}| \tag{3.11}$$

where $\mathbf{v}_E(t_0)$ is the initial normal velocity of E and $\mathbf{v}_E(t_f)$ is the final rebound normal velocity of E.

3.1.3 Simulation results

The equations of the motion are solved with MATLAB. The contact force coefficients and effective friction coefficient are found experimentally and used in the simulation. The ball

impacts the surface with initial impact velocity of the center of the ball $\mathbf{v}_C(t_0) = -2\mathbf{\imath}_0$ m/s in global coordinates. The results are shown for the impact angle $\beta = 15°$. The displacement of the center of the ball during the impact has been simulated in local coordinates as seen in Fig. 3.3. The normal and tangential components of the displacement of the center of the ball during the impact have been shown with solid and dotted lines, respectively. The compression phase ends at nearly $t = 3.1$ ms, and the restitution phase starts from this point.

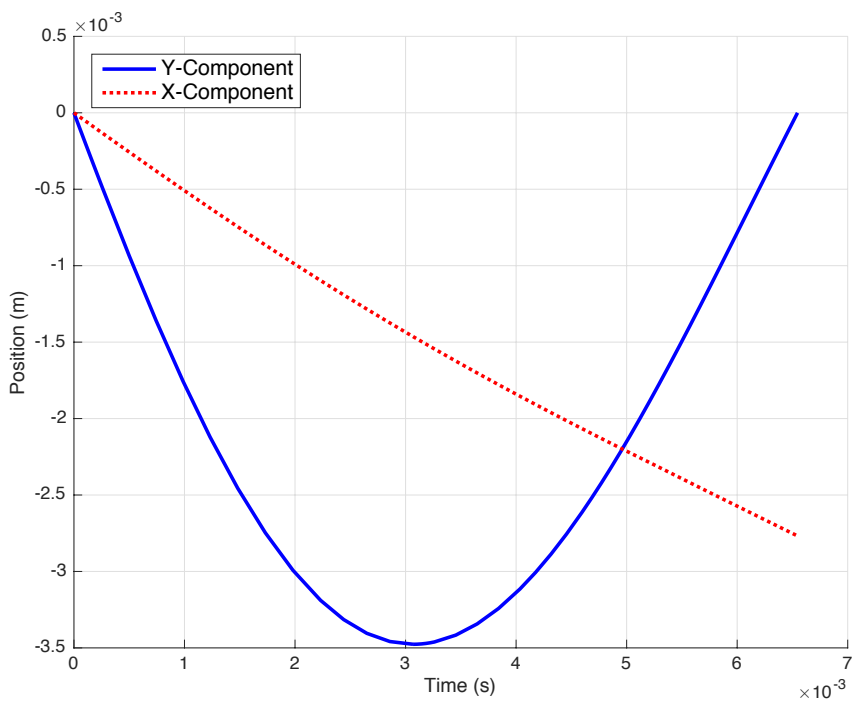

Figure 3.3: The displacement of the center of the ball during the impact in local coordinates $[\mathbf{\imath}, \mathbf{\jmath}, \mathbf{k}]$ for the impact angle $\beta = 15°$.

Figure 3.4 depicts the velocity of the center of the ball during the impact in both normal and tangential directions. The normal velocity of the ball becomes zero at $t =$ 3.1 ms. The normal velocities before and after the impact have been found as $\mathbf{v}_C(t_0) - 1.93\mathbf{\jmath}$, $\mathbf{v}_C(t_f) = 1.67\mathbf{\jmath}$ m/s, respectively. The coefficient of restitution is measured as $e = 0.86$.

The normal contact force as a function of the displacement during the impact has also been simulated for the impact angle $\beta =$ 15°, and the results can be seen in Fig. 3.5. The

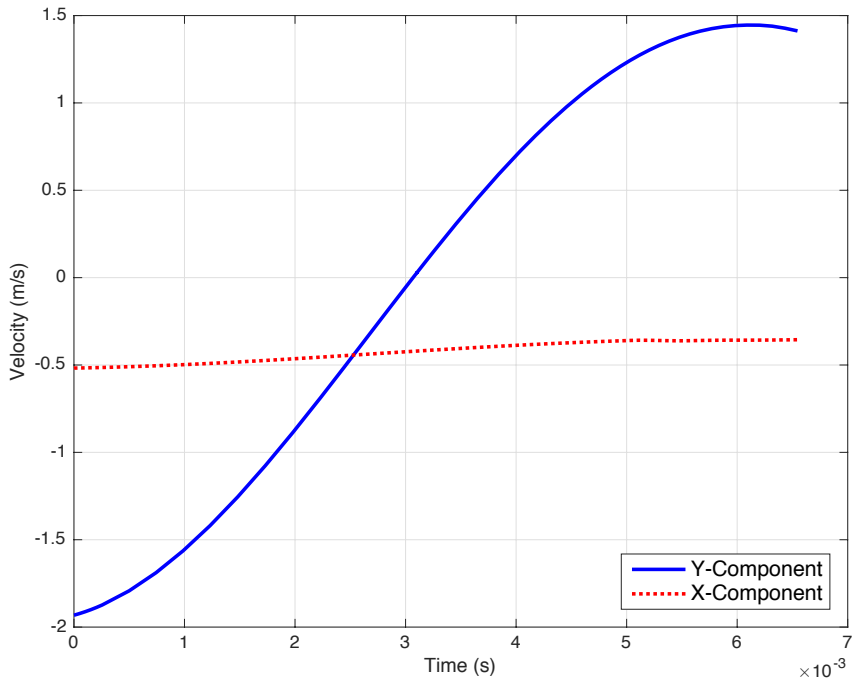

Figure 3.4: The velocity of the center of the ball during the impact in local coordinates $[\mathbf{i}, \mathbf{j}, \mathbf{k}]$ for the impact angle $\beta = 15°$.

loading phase has been shown with solid line. Two different conditions have been applied for the unloading phase. First, the unloading phase is considered as fully elastic which is represented with dashed line in Fig. 3.5. Second, the unloading phase is considered elasto-plastic which includes of the damping coefficient to represent the energy lost. The result for this condition is shown with dotted line in Fig. 3.5. The normal contact force at the beginning of the impact is discontinuous due to damping term. The contact force increases over time and reaches its maximum at $t = 3.1$ ms when the normal velocity becomes zero. The unloading phase starts from this point where maximum deformation occurs. The unloading phase with damping coefficient shows a negative contact force at the end of the impact. As the ball leaves the surface, the indentation tends to be zero. The relative velocity tends to be negative. This causes a negative force that holds the ball and the racket string-bed together. For the unloading phase without damping, the normal contact force decreases from its maximum to zero where the ball leaves the surface.

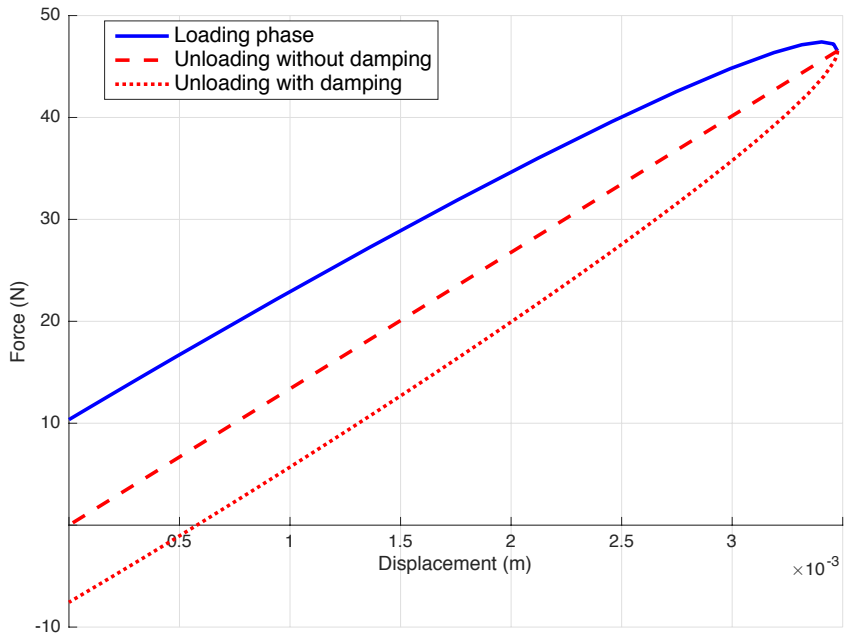

Figure 3.5: The normal contact force and the displacement during the impact for $\beta = 15°$.

3.2 Experiments

An experimental setup has been built in order to provide consistent initial conditions for the impacts. The sketch of the setup is shown in Fig. 2.8. Tennis balls with the diameter of 67 mm and a mass of 56.7 gr have been used for the experiments. A robotic arm has been used to release the ball from different heights in the range of 0.025 m to 1.031 m. For each height, at least three balls have been dropped consistently with the robotic arm. The tennis racket has been fixed on a stringing device and the stringing device is clamped to the fixed table to make the racket steady during the impact. One end of the stringing device has been attached to a tripod as shown in Fig. 2.8. The angle of the racket is controlled and changed gradually by changing the height of the tripod with an accuracy of $\pm 1°$. A digital high-speed camera has been used in order to capture the motion of the ball before, during, and after the impact. In order to provide sufficient light for the high-speed camera, four $1,000$ W projectors have been used.

Five different impact angles have been studied, $\beta = 0°, 15°, 30°, 45°$ and $57°$. For each angle, five different initial velocities in the range of 0.5 to 4.5 m/s have been used. The experiments have been repeated at least three times for each initial velocity. The position and velocity of the ball have been measured using MATLAB. The center of the ball has been tracked in the global $[\mathbf{\imath}_0, \mathbf{\jmath}_0, \mathbf{k}_0]$ and local reference frames $[\mathbf{\imath}, \mathbf{\jmath}, \mathbf{k}]$. Finally the results from the experiments have been compared with the theory.

3.2.1 Image processing

An image processing method has been developed to measure the motion of the ball before, during, and after the impact. The motion of the ball has been captured using the high-speed camera at 10,000 fps. Each frame has a resolution of 512×512 pixels. Figure 3.6 shows the instant just before the ball impacts the racket.

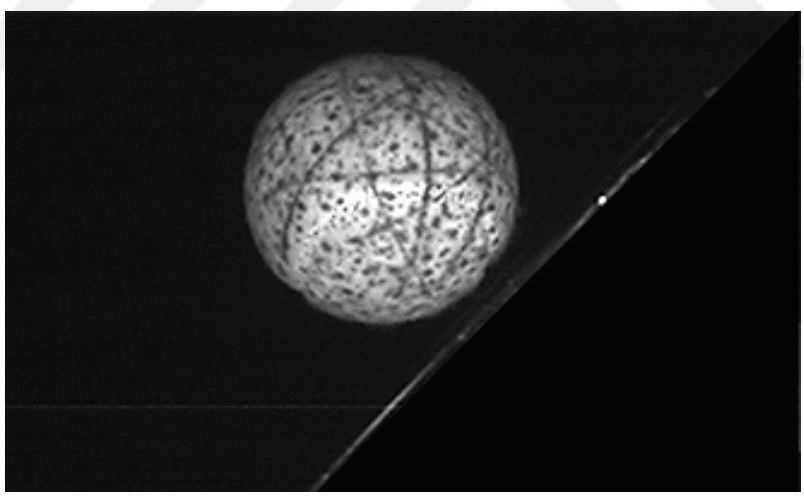

Figure 3.6: Image of the ball just before impacting the racket.

An integer between 0 and 255 called gray value has been assigned to each pixel representing pure black and pure white respectively. Modifications on the image were needed in order to find the center of the ball. First, the gray threshold of the frame has been found. The pixels with a larger gray value have been changed to pure white and the pixels with a smaller gray value have been changed to pure black. The picture after the gray value modification is shown in Fig. 3.7. The boundary of the ball is found by changing the contrast.

A red filter has been applied on the image and the boundary has been changed to yellow as shown in Fig. 3.8. The radius and the center of the ball have been found using the Hough transform method, [105, 106].

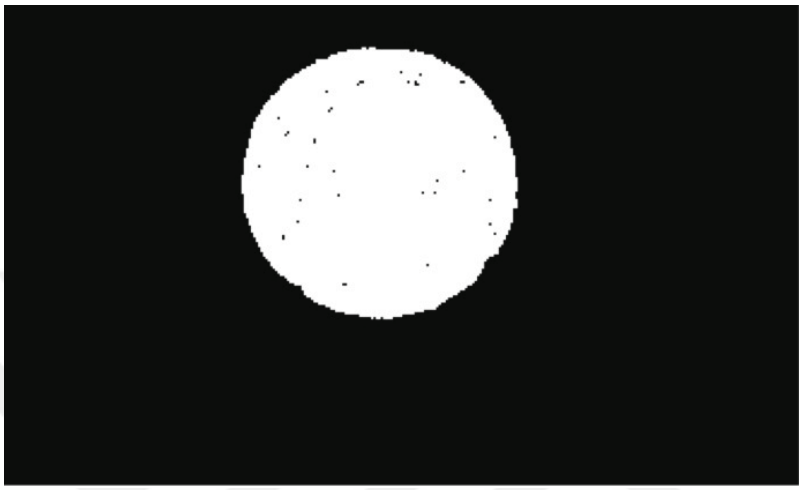

Figure 3.7: Modifying the contrast and finding the boundary.

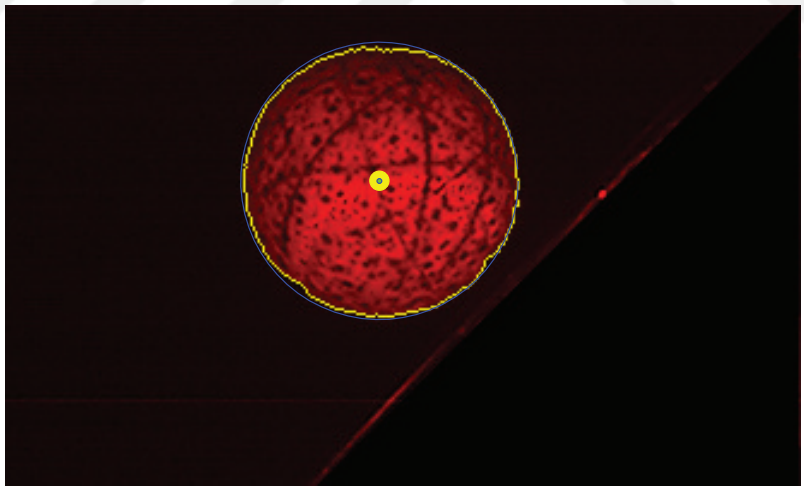

Figure 3.8: Calculating the position of the center of the ball.

The Hough transform method is a technique used in image analysis and digital image processing. It is a useful and effective way to detect analytically defined shapes such as lines and circles and to be able to recognize partial or slightly deformed shapes. The Hough transform method is used to find the shape of the ball for each frame.

A circle with radius R and center (a, b) can be described with the parametric equations:

$x = a + Rcos(\theta)$ and $y = b + Rsin(\theta)$.

When the angle θ sweeps through the full 360 degree range the points (x, y) trace the perimeter of the circle. This method can calculate the position of the center of the ball more accurately with the modifications we have made. This process provides a consistent algorithm to find the ball and its center, even when a part of the ball becomes invisible on the image.

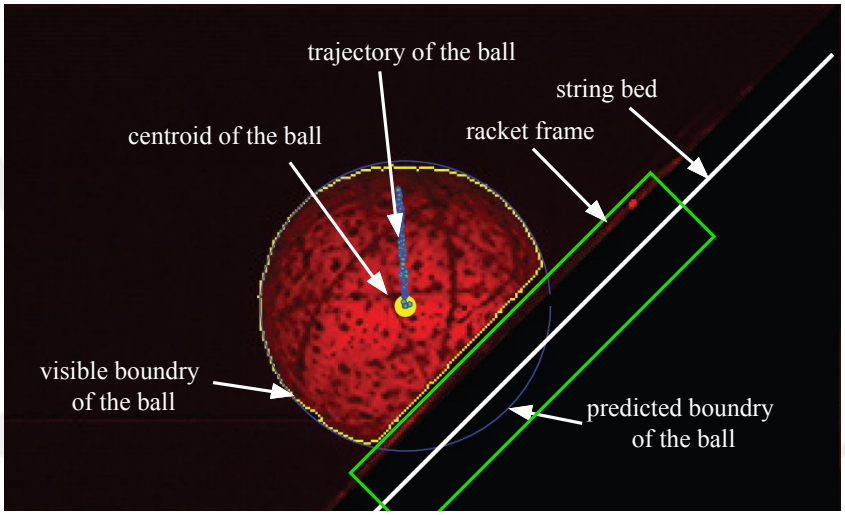

Figure 3.9: Tracking the position of the center of the ball while part of it is covered with the racket.

Figure 3.9 is a sample of the analyzed images while the ball is in contact with the tennis racket. A part of the ball is behind the racket frame during the impact as shown in Fig. 3.9. The big dot at the center of the ball shows the calculated centroid of the ball. The blue line on the top of the centroid ("trajectory of the ball") shows the trajectory of the centroid for the previous frames. The points around the ball show the calculated boundary of the ball. The predicted circle with the Hough transform is shown in Fig. 3.9.

This process has been done for all of the frames. Figure 3.10 shows the trajectory of the centroid of the ball for all of the impact angles. The average radius of the ball in pixels has been found with a standard deviation less than a pixel. This average radius in pixels has been used in order to find a scale factor to convert the displacement from pixels to meters. Calculating the scale factor from pixel to meter with this method eliminates the out-of-plane

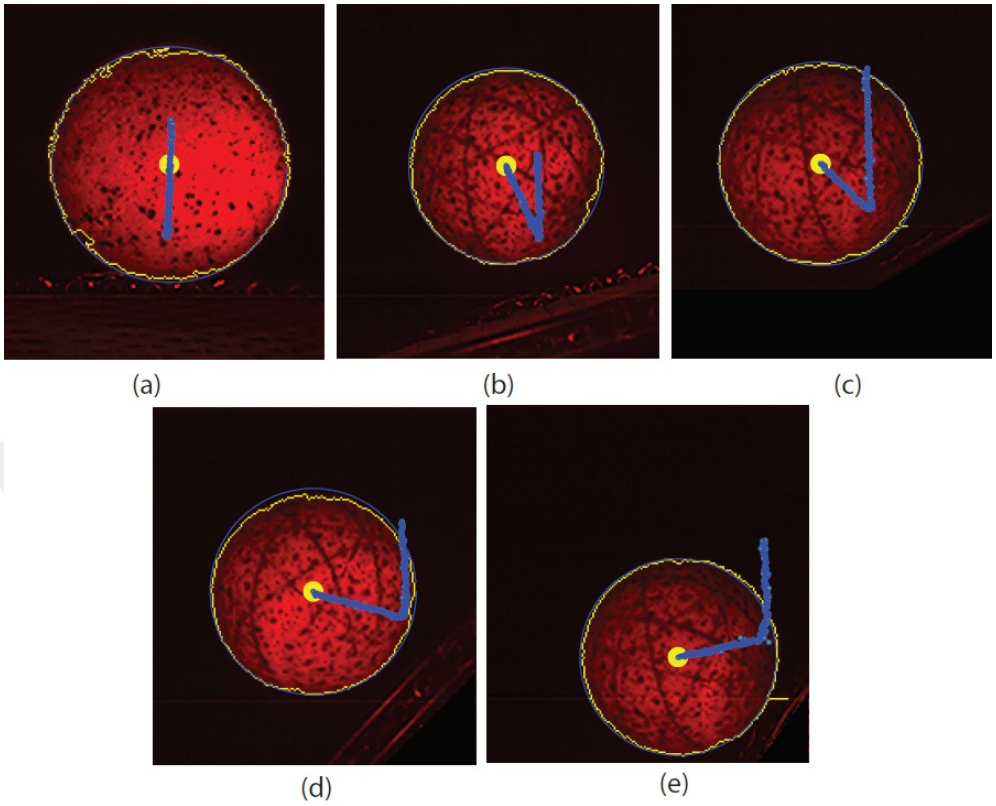

Figure 3.10: Trajectory of the ball for different impact angles with the Hough transform method: (a) normal impact, (b) $\beta = 15°$, (c) $\beta = 30°$, (d) $\beta = 45°$,(e) $\beta = 57°$.

displacement errors. Finally the position of the center of the ball has been calculated before, during, and after the impact in the global $[\mathbf{\imath}_0, \mathbf{\jmath}_0, \mathbf{k}_0]$ and local coordinates $[\mathbf{\imath}, \mathbf{\jmath}, \mathbf{k}]$.

3.2.2 Experimental results

The experimental velocities before and after the impact are calculated using 100 data points before the impact and 100 data points after the impact in the global coordinates and transformed to the local coordinates. The displacement of the center of the ball has been tracked with the image processing technique for five different impact angles.

Normal impact

Figure 3.11 shows the displacement of the center of the ball in the global coordinates for the impact with $\beta = 0°$ for one of the experiments. For the impact angle $\beta = 0°$, the global and local coordinates are the same. The initial velocity of the center of the ball is $\mathbf{v}_C(t_0) = -3.26\mathbf{J}_0$ m/s in the global and local coordinates. The impact starts at $t_0 = 0.0092$ s and ends at $t_f = 0.017$ s. The maximum deflection during the impact is $\delta_m = 0.0079$ m. The velocity of the center of the ball after the impact is $\mathbf{v}_C(t_0) = 2.93\mathbf{J}_0$ m/s.

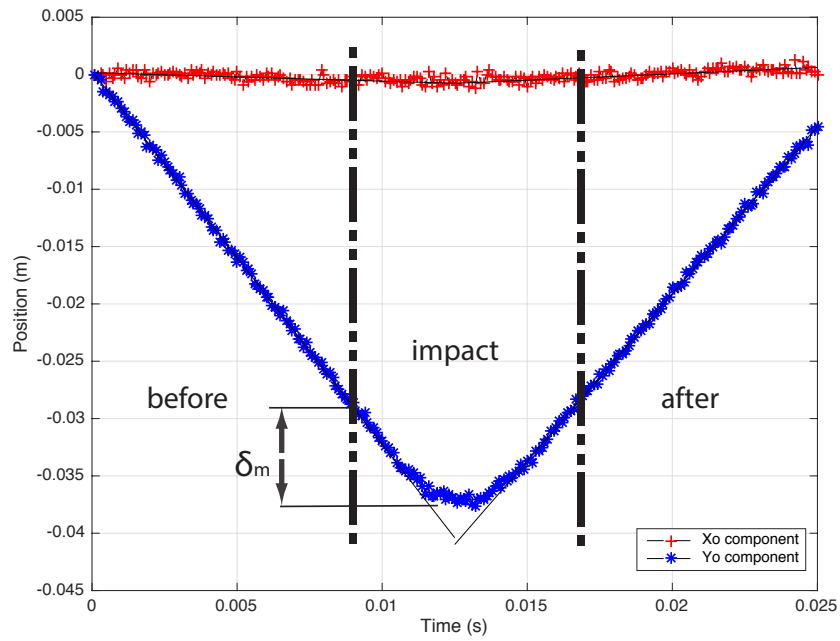

Figure 3.11: The displacement of the center of the ball in global $[\mathbf{I}_0, \mathbf{J}_0, \mathbf{k}_0]$ and local coordinates $[\mathbf{I}, \mathbf{J}, \mathbf{k}]$ for the impact angle $\beta = 0°$.

Oblique impact ($\beta = 15°$)

Figures 3.12 and 3.13 depict the displacement of the center of the ball for the impact angle $\beta = 15°$ in the global and local coordinates respectively. The initial velocity before the impact is $\mathbf{v}_C(t_0) = 0.10\mathbf{I}_0 - 2.60\mathbf{J}_0$ m/s in the global coordinates, which is equal to $\mathbf{v}_C(t_0) = -0.57\mathbf{I} - 2.53\mathbf{J}$ m/s in the local coordinates.

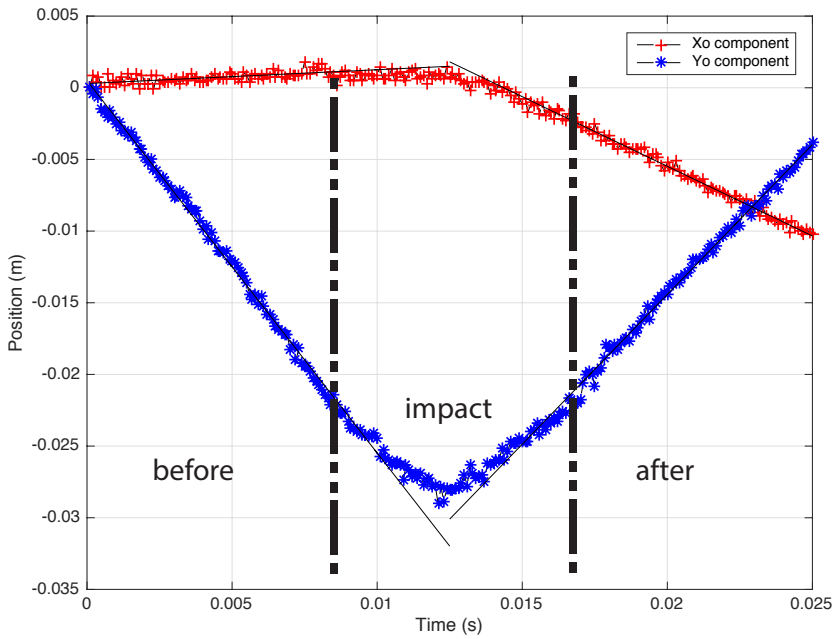

Figure 3.12: The displacement of the center of the ball in global coordinates $[\mathbf{\imath}_0, \mathbf{\jmath}_0, \mathbf{k}_0]$ for the impact angle $\beta = 15°$.

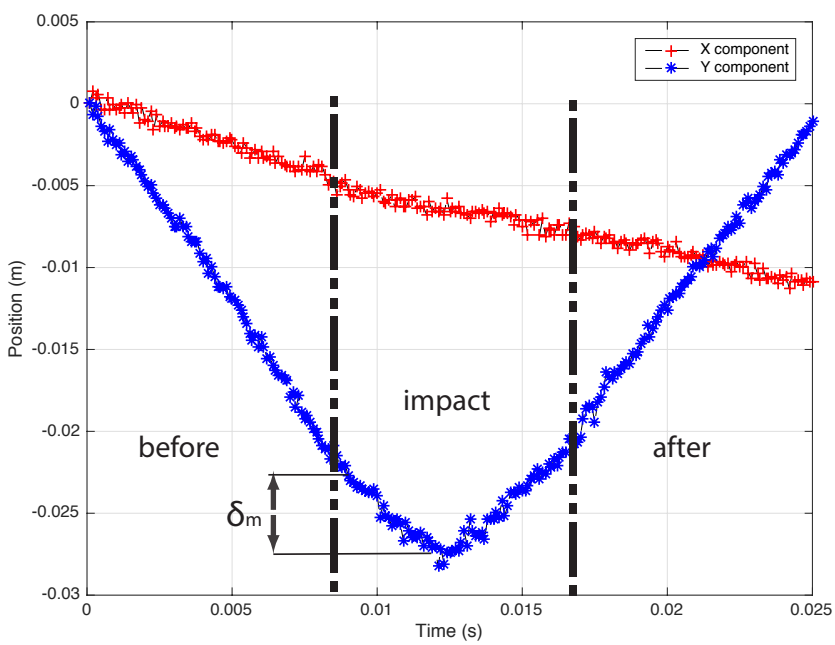

Figure 3.13: The displacement of the center of the ball in local coordinates $[\mathbf{\imath}, \mathbf{\jmath}, \mathbf{k}]$ for the impact angle $\beta = 15°$.

The impact starts at $t_o = 0.0089$ s and ends at $t_f = 0.0175$ s. The maximum deflection during the impact is $\delta_m = 0.0050$ m. The velocity of center of the ball after the impact is $\mathbf{v}_C(t_f) = -0.97\mathbf{\imath}_0 + 2.09\mathbf{\jmath}_0$ m/s in the global coordinates and $\mathbf{v}_C(t_f) = -0.39\mathbf{\imath} + 2.27\mathbf{\jmath}$ m/s in the local coordinates.

Oblique impact ($\beta = 30°$)

Figures 3.14 and 3.15 show the displacement of the center of the ball for the impact angle $\beta = 30°$ in the global and local coordinates respectively. The initial velocity before the impact is $\mathbf{v}_C(t_0) = 0.105\mathbf{\imath}_0 - 3.77\mathbf{\jmath}_0$ m/s in the global coordinates, which is equal to $\mathbf{v}_C(t_0) = -1.8\mathbf{\imath} - 3.32\mathbf{\jmath}$ m/s in the local coordinates. The impact starts at $t_o = 0.0108$ s and ends at $t_f = 0.0148$ s. The maximum deflection during the impact is $\delta_m = 0.00426$ m. The velocity of center of the ball after the impact is $\mathbf{v}_C(t_f) = -2.30\mathbf{\imath}_0 + 2.11\mathbf{\jmath}_0$ m/s in the global coordinates and $\mathbf{v}_C(t_f) = -0.94\mathbf{\imath} + 2.98\mathbf{\jmath}$ m/s in the local coordinates.

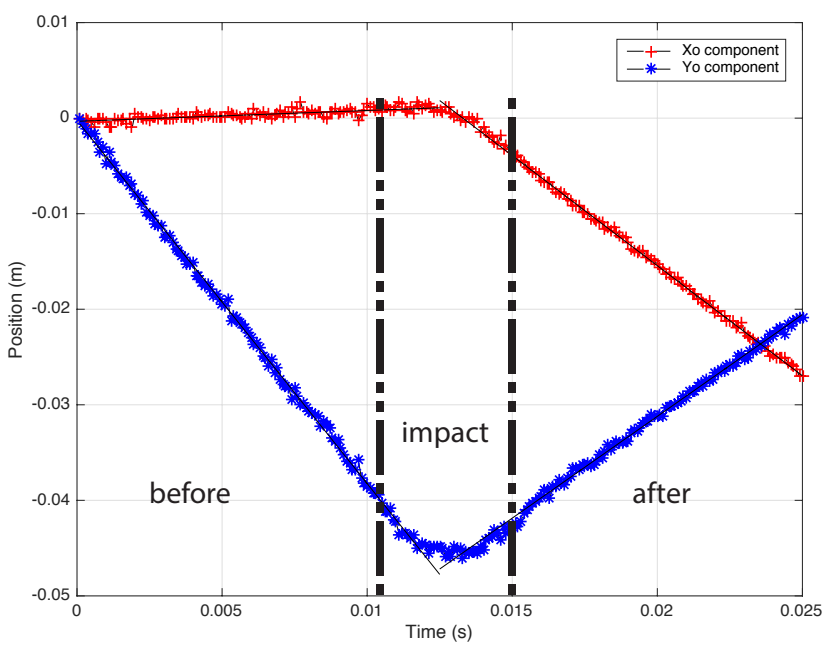

Figure 3.14: The displacement of the center of the ball in global coordinates $[\mathbf{\imath}_0, \mathbf{\jmath}_0, \mathbf{k}_0]$ for the impact angle $\beta = 30°$.

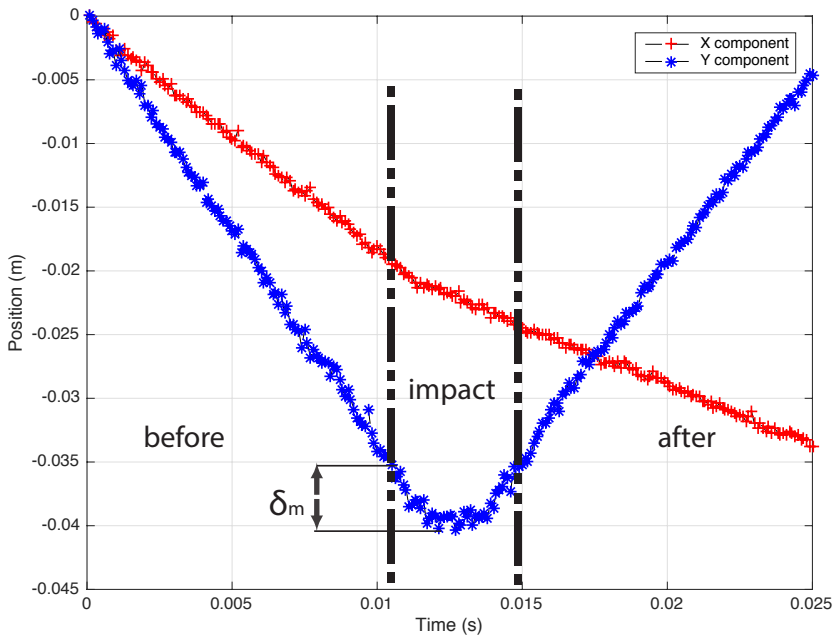

Figure 3.15: The displacement of the center of the ball in local coordinates $[\mathbf{\imath}, \mathbf{\jmath}, \mathbf{k}]$ for the impact angle $\beta = 30°$.

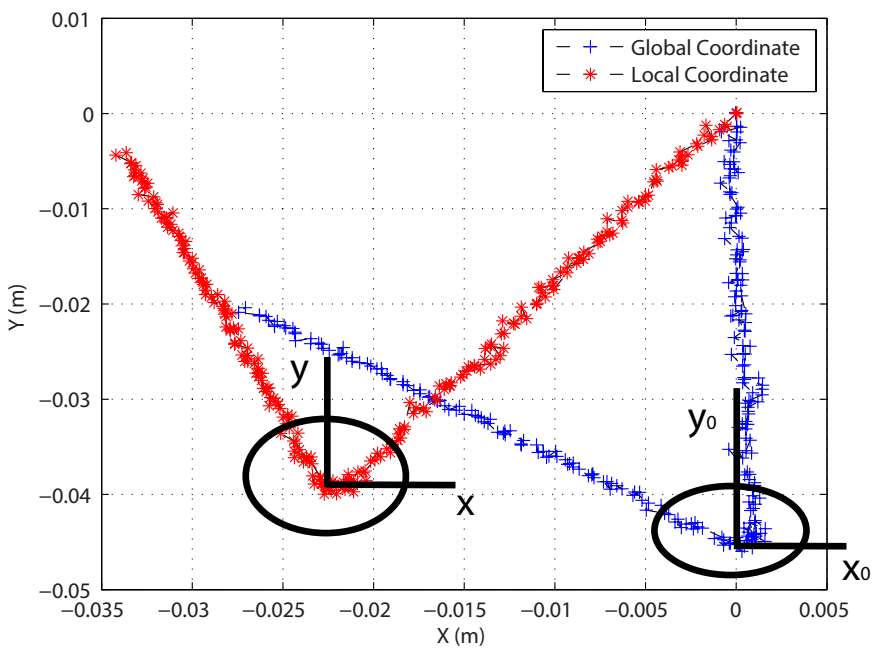

Figure 3.16: Path of the center of the ball in global $[\mathbf{\imath}_0, \mathbf{\jmath}_0, \mathbf{k}_0]$ and local $[\mathbf{\imath}, \mathbf{\jmath}, \mathbf{k}]$ coordinates for the impact angle $\beta = 30°$.

Figure 3.16 shows the trajectory of the center of the ball in both the global coordinates and the local coordinates for the impact with $\beta = 30°$. In the global coordinates, the ball goes down vertically, impacts the racket and goes back up with both the vertical and the horizontal components. In the local coordinates, the ball has both tangential and normal components, before and after the impact.

Oblique impact ($\beta = 45°$)

Figures 3.17 and 3.18 show the displacement of the center of the ball for the impact angle $\beta = 45°$ in the global and local coordinates, respectively. The initial velocity before the impact is $\mathbf{v}_C(t_0) = 0.15\mathbf{\imath}_0 - 3.69\mathbf{\jmath}_0$ m/s in the global coordinates, which is equal to $\mathbf{v}_C(t_0) = -2.5\mathbf{\imath} - 2.72\mathbf{\jmath}$ m/s in the local coordinates. The impact starts at $t_o = 0.0069$ s and ends at $t_f = 0.0108$ s. The maximum deflection during the impact is $\delta_m = 0.00437$ m. The velocity of the center of the ball after the impact is $\mathbf{v}_C(t_f) = -2.75\mathbf{\imath}_0 + 0.71\mathbf{\jmath}_0$ m/s in the global coordinates and $\mathbf{v}_C(t_f) = -1.43\mathbf{\imath} + 2.45\mathbf{\jmath}$ m/s in the local coordinates.

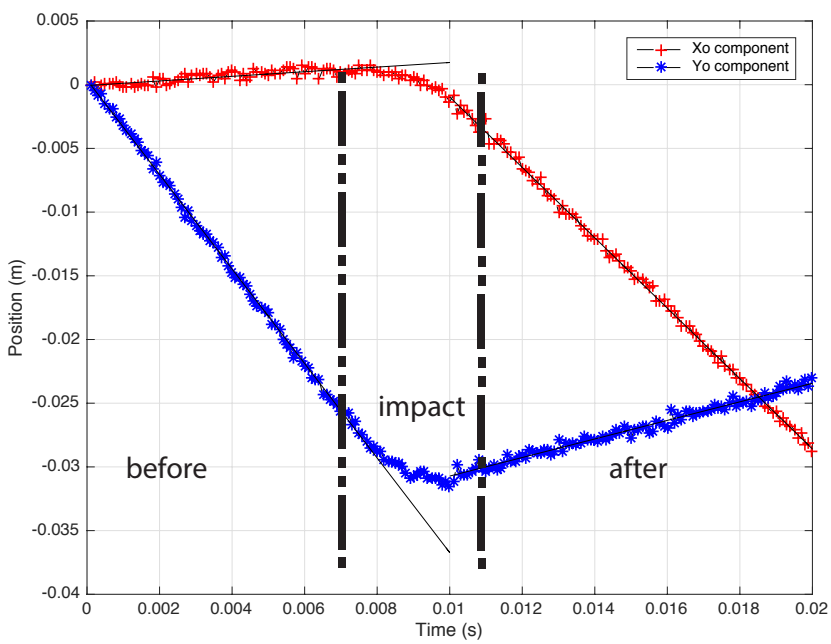

Figure 3.17: The displacement of the center of the ball in global coordinates $[\mathbf{\imath}_0, \mathbf{\jmath}_0, \mathbf{k}_0]$ for the impact angle $\beta = 45°$.

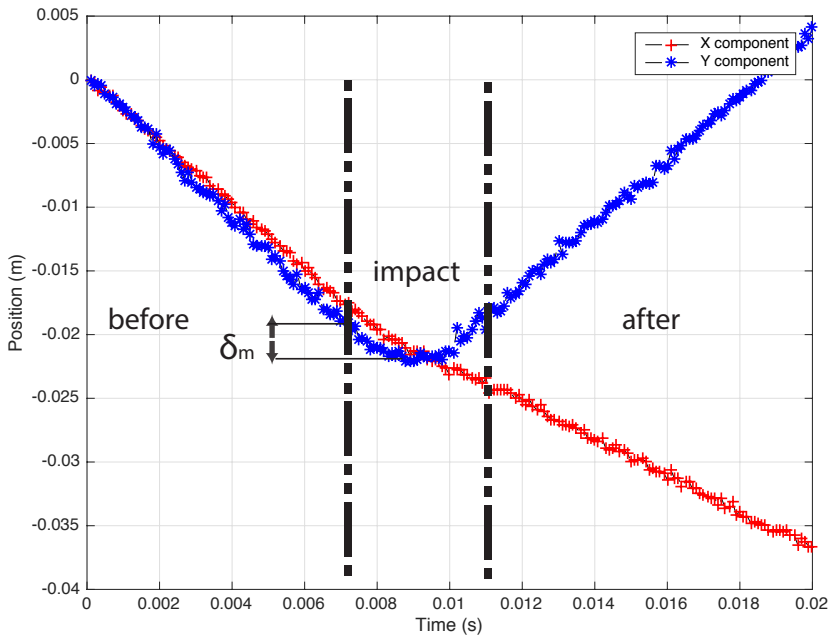

Figure 3.18: The displacement of the center of the ball in local coordinates $[\mathbf{\imath}, \mathbf{\jmath}, \mathbf{k}]$ for the impact angle $\beta = 45°$.

Oblique impact ($\beta = 57°$)

Figures 3.19 and 3.20 present the displacement of the center of the ball for the impact angle $\beta = 57°$ in the global and local coordinates, respectively. The initial velocity before the impact is $\mathbf{v}_C(t_0) = 0.165\mathbf{\imath}_0 - 3.92\mathbf{\jmath}_0$ m/s in the global coordinates, which is equal to $\mathbf{v}_C(t_0) = -3.20\mathbf{\imath} - 2.27\mathbf{\jmath}$ m/s in the local coordinates. The impact starts at $t_o = 0.0060$ s and ends at $t_f = 0.0120$ s. The maximum deflection during the impact is $\delta_m = 0.0069$ m. The velocity of the center of the ball after the impact is $\mathbf{v}_C(t_f) = -2.80\mathbf{\imath}_0 - 0.47\mathbf{\jmath}_0$ m/s in the global coordinates and $\mathbf{v}_C(t_f) = -1.91\mathbf{\imath} + 2.07\mathbf{\jmath}$ m/s in the local coordinates.

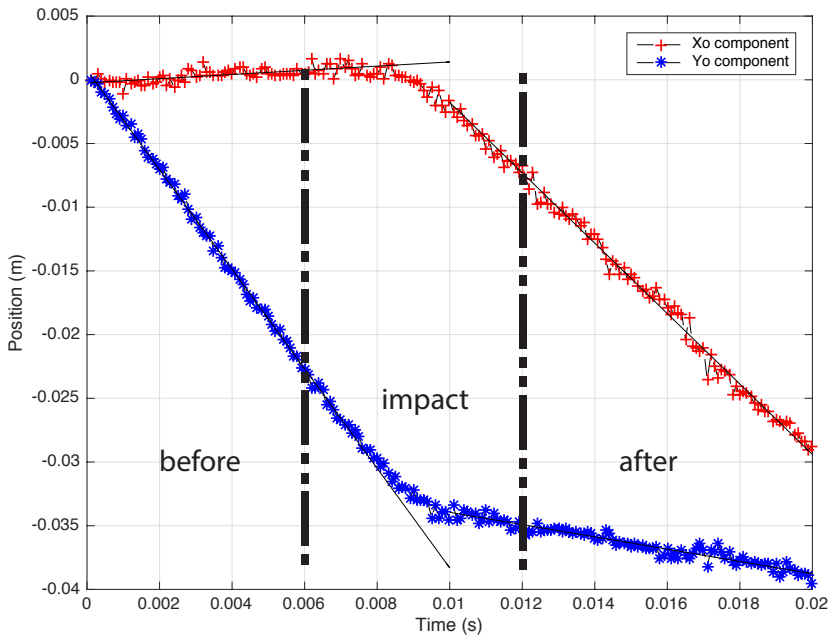

Figure 3.19: The displacement of the center of the ball in global coordinates $[\mathbf{\imath}_0, \mathbf{\jmath}_0, \mathbf{k}_0]$ for the impact angle $\beta = 57°$.

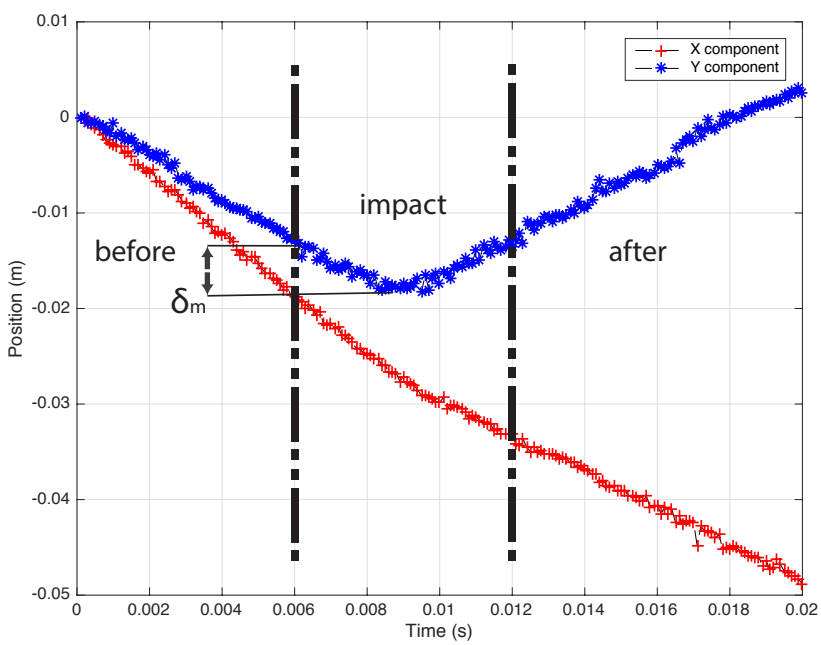

Figure 3.20: The displacement of the center of the ball in local coordinates $[\mathbf{\imath}, \mathbf{\jmath}, \mathbf{k}]$ for the impact angle $\beta = 57°$.

3.2.3 Coefficient of restitution

In this study, the Newtonian coefficient of restitution is used where it is defined as the ratio of the normal velocity after and before the impact. Figure 3.21 shows the coefficient of restitution in terms of the initial velocities for different impact angles. The results are shown for five different impact angles: 0°, 15°, 30°, 45°, and 57°. The coefficient of restitution does not change significantly for different impact angles as it seen in Fig. 3.21, and it has an average value of $e = 0.88$. The coefficient of restitution has been averaged for all of the experimental initial velocities for each angle β as shown in Fig. 3.22. Each cross shaped point shows the average result of different initial velocities for the same impact angle. The coefficient of restitution does not change with the impact angle for the low velocity impact.

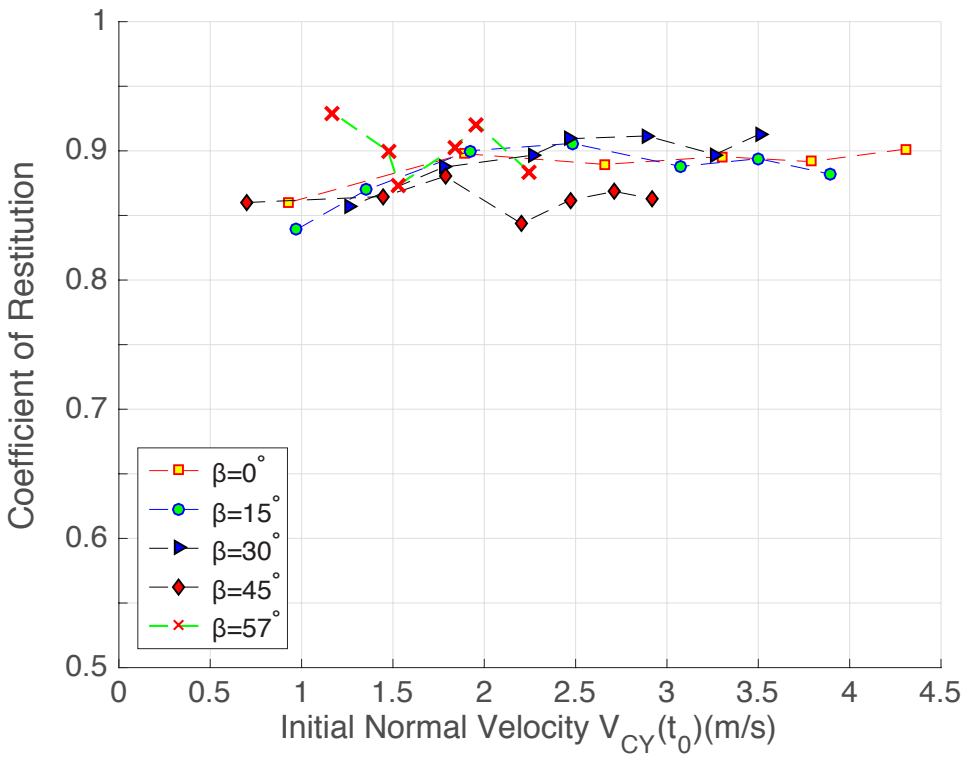

Figure 3.21: Coefficient of restitution for different initial normal velocities from 0.5 to 4.5 m/s.

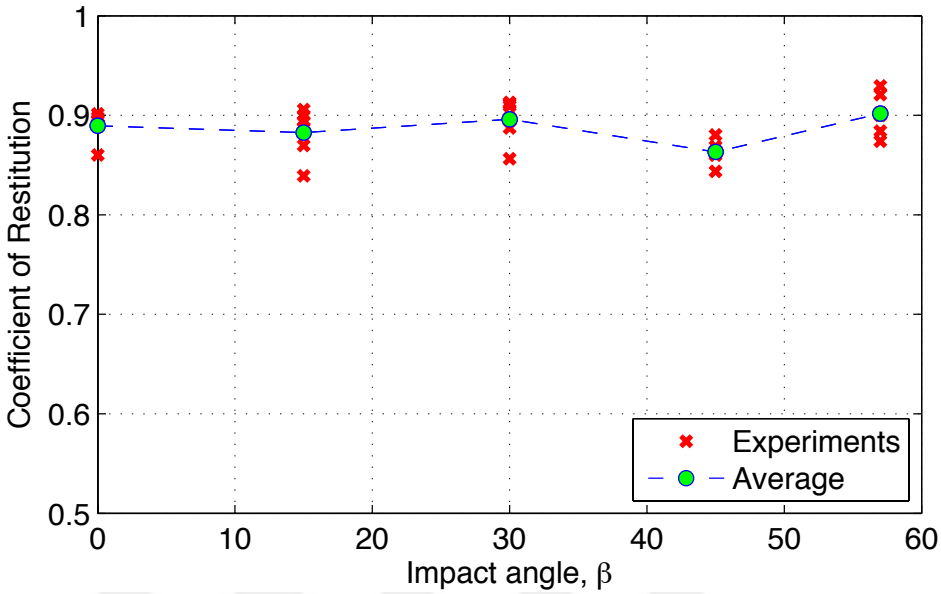

Figure 3.22: Average coefficient of restitution for different impact angles β.

3.2.4 Effective coefficient of friction

The effective coefficient of friction is calculated from the tangential and normal velocity before and after the impacts. It should be noted that this friction is the average friction throughout the impact. The effective coefficient of friction is the ratio between the tangential and normal impulses and calculated as follows;

$$\mu = \frac{m[v_{Cx}(t_f) - v_{Cx}(t_0)]}{m[v_{Cy}(t_f) - v_{Cy}(t_0)]}. \tag{3.12}$$

Figure 3.23 shows the effective coefficient of friction for different initial velocities from 0.5 to 4.5 m/s and different impact angles. The effective coefficient of friction can be considered as constant for each angle for the range of different low velocities.

Figure 3.24 depicts the variation of the effective coefficient of friction with respect to the angle of the racket. Each cross shaped point represents the result for different initial impact velocities for each of the impact angles. The results show that the effective coefficient of friction increases as the impact angle β increases.

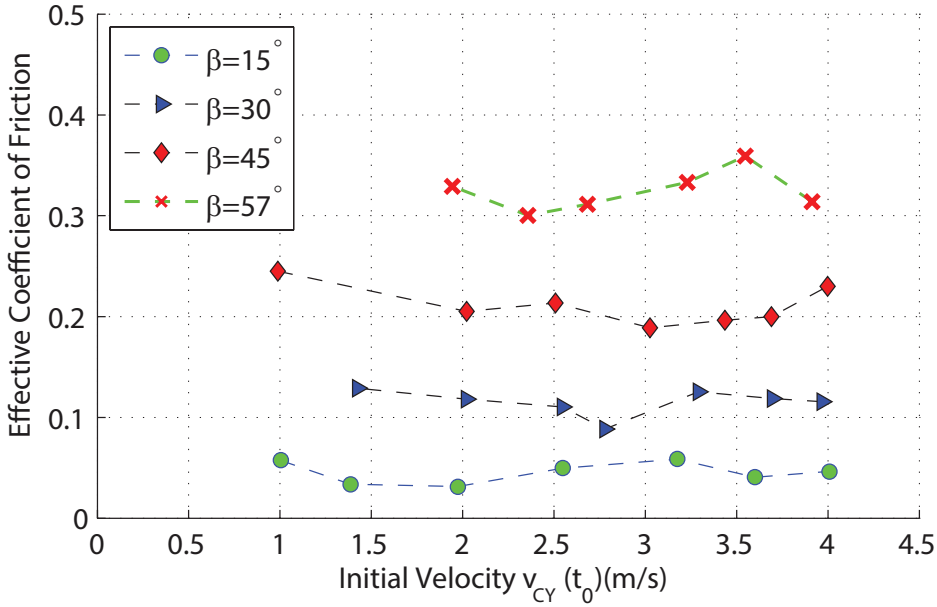

Figure 3.23: Effective coefficient of friction for different initial velocities from 0.5 to 4.5 m/s and different impact angles β.

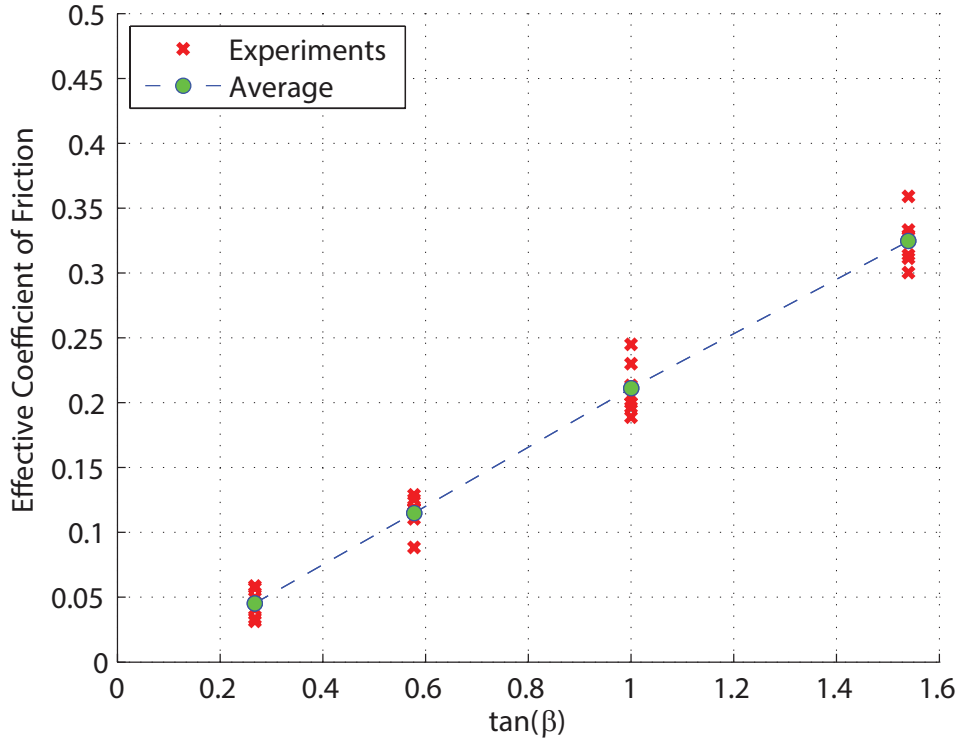

Figure 3.24: Variation of the effective coefficient of friction for different impact angles β.

3.3 Comparing the theory and experiments

In order to verify the theory for the oblique impacts, the contact force coefficients in Eq. 3.6, k (stiffness) and b (damping) coefficients, have to be calculated.

3.3.1 Finding force coefficients

The experimental results for the normal impact ($\beta = 0$) have been used in order to find the contact force coefficients. A total of 15 different experiments have been analyzed. The displacement of the ball and velocity of the ball after the impact have been taken into consideration in order to find the contact force coefficients. The stiffness and damping coefficients have been varied from 0 - 30 000 N/m and 0 - 20 Ns/m, respectively. The mean absolute error has been found between the theory and experiments.

Figure 3.25 presents the mean absolute error for the displacement of the ball between the theory and one of the experiments. The vertical axis shows the error for the range of k and b. The minimum errors are located approximately on a line perpendicular to the k axis which shows that the stiffness coefficient plays a dominant role on the error for displacement. The minimum error cannot be obtained using the displacement error as shown in Fig. 3.25.

Figure 3.26 shows the error between the theory and experiment for the velocity after the impact. No minimum error can be found for this case either. The minimum errors are located approximately on a line perpendicular to the b axis.

In order to find the minimum error, the errors for the displacement and velocity after the impact have been multiplied and summed. First we tried multiplication of the error to see if it gives a minimum error. As it is seen in Fig. 3.27, no minimum error can be obtained successfully for k and b contact coefficients. We then summed the error in both displacement and final velocity cases. Figure 3.28 shows the summation of the error, and it changes in the range of 0 % to 140 % for this case. The minimum error can be finally obtained from the sum of the errors. The minimum can be found in Fig. 3.28 approximately at $k = 13\ 000$ N/m and $b = 7$ Ns/m for this case.

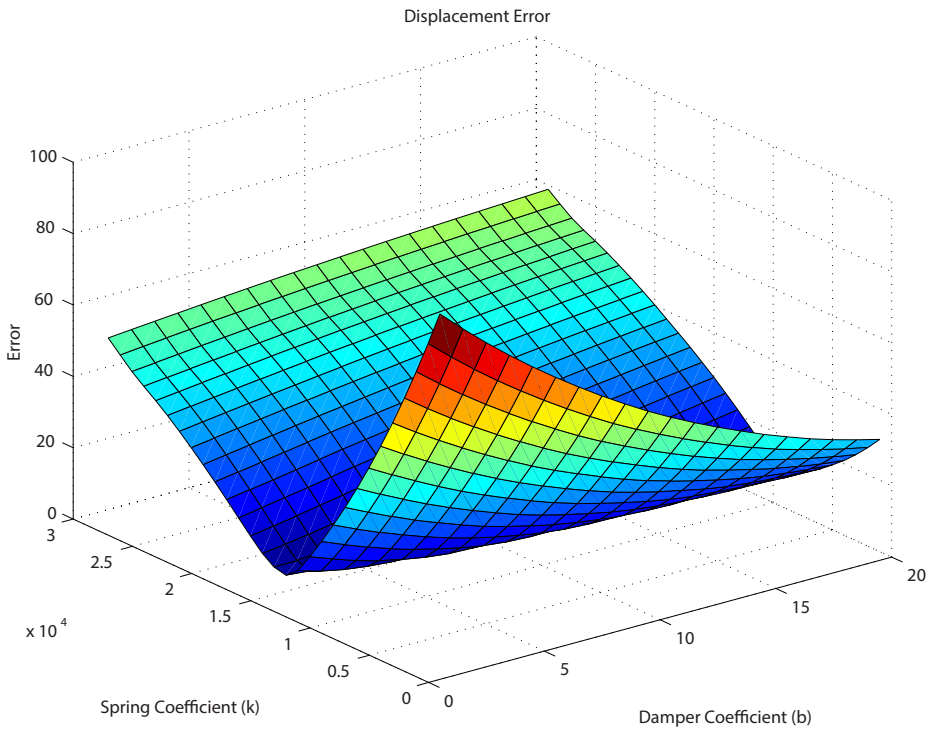

Figure 3.25: Displacement mean absolute error for the variation of k and b.

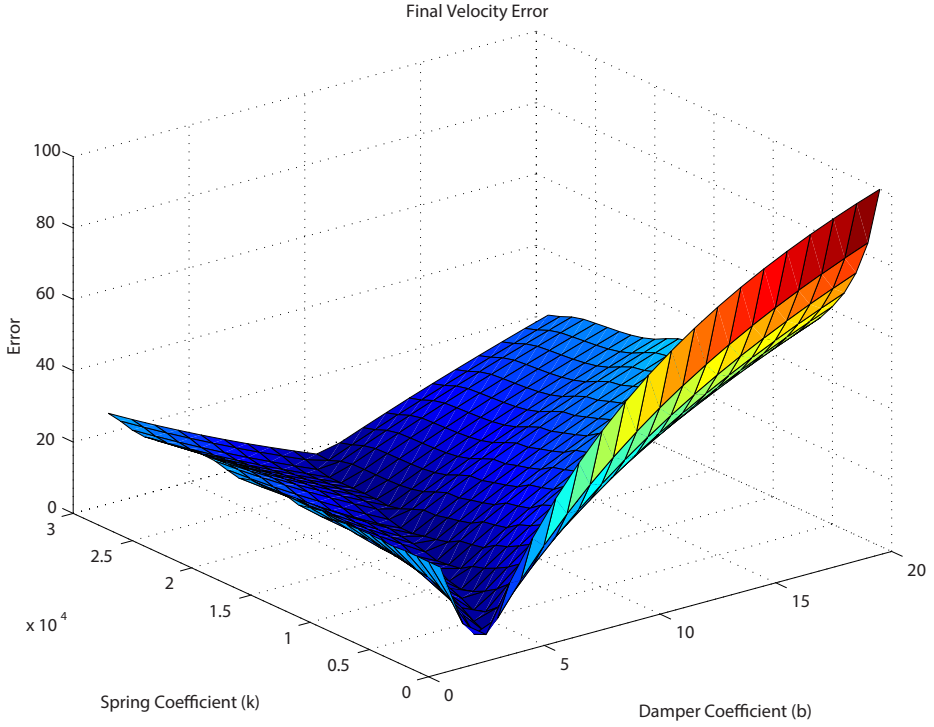

Figure 3.26: Velocity after the impact mean absolute error for the variation of k and b.

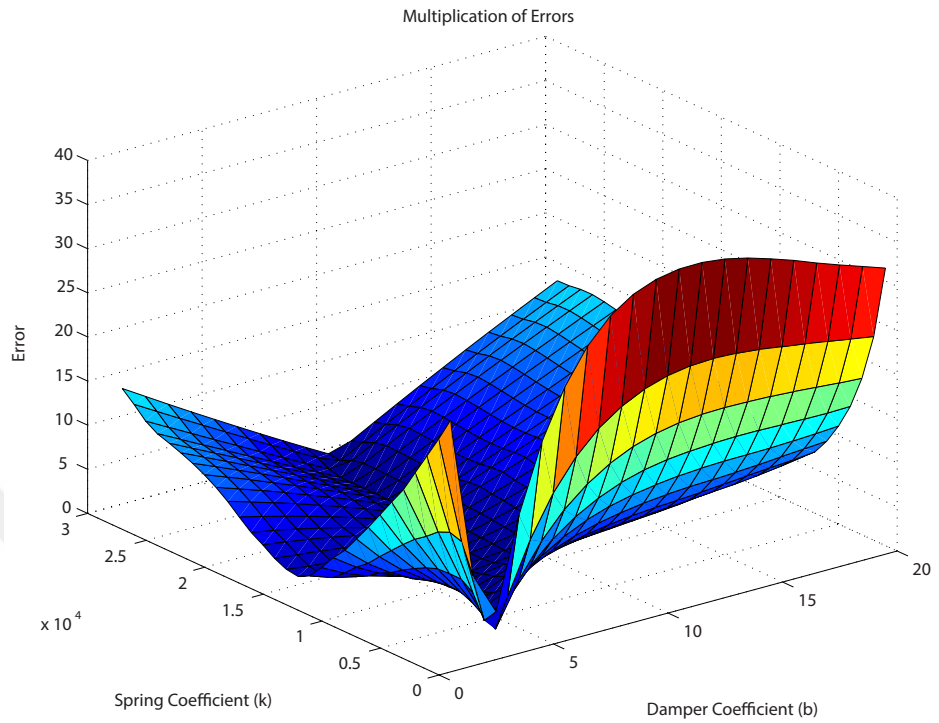

Figure 3.27: Multiplication of mean absolute error for the variation of k and b.

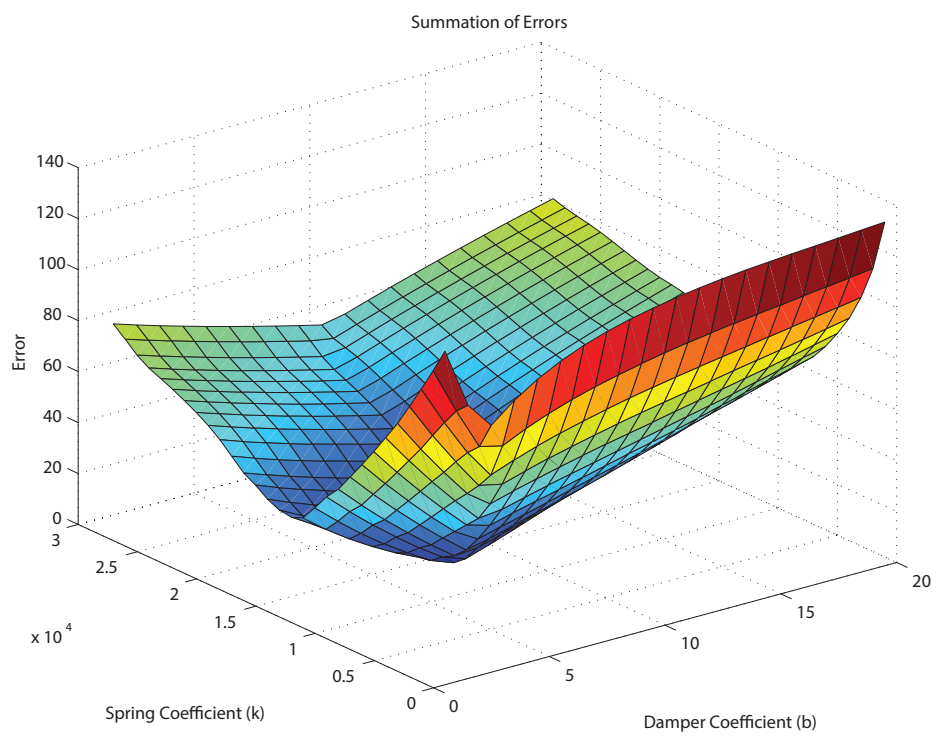

Figure 3.28: Summation of mean absolute error for the variation of k and b.

In order to find the contact coefficients with better accuracy, 2D spline interpolation method is used with MATLAB as seen in Fig. 3.29. The minimum is found at $k = 12\ 526$ N/m and $b = 6.85$ Ns/m with 2D spline interpolation for this case. The coefficients k and b have been found for 15 impacts for the normal impact. The average for the coefficients have been calculated as:

$$k = 13\ 385 \text{ N/m} \qquad \text{and} \qquad b = 5.36 \text{ Ns/m}.$$

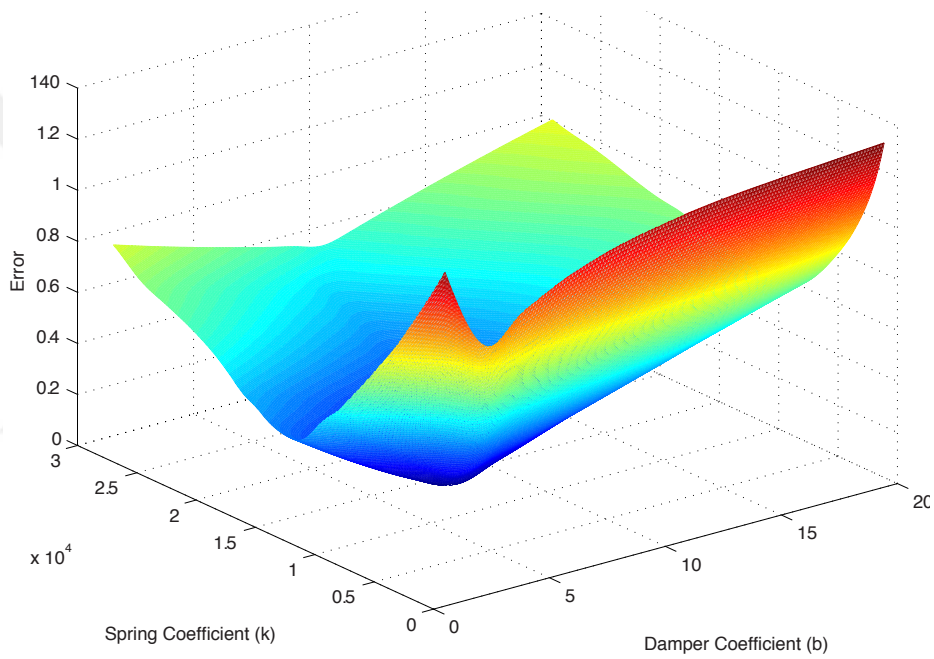

Figure 3.29: Summation of error with 2D spline interpolation.

3.3.2 Verifying the theory for the oblique impact

The contact coefficients have been found experimentally for the normal impact. The averaged stiffness and damping coefficients found previously have been used for the theory. The displacement of the center of the ball and the velocity after the impact have been analyzed for $\beta = 15°$, $\beta = 30°$, $\beta = 45°$, and $\beta = 57°$. The initial impact velocities from the experiments have been used as initial condition for the theory. The displacement and velocity after the impact errors between the theory and experiment have been found for all of the experiments.

Oblique impact ($\beta = 15°$)

Figures 3.30 and 3.31 present the normal and tangential components of the displacement of the center of the ball for the theory and one of the experiments with $\beta = 15°$. The initial velocity before the impact is found from the experiment $\mathbf{v}_C(t_0) = -0.57\mathbf{\imath} - 2.5\mathbf{\jmath}$. The experiment shows that the final velocity is $\mathbf{v}_C(t_f) = -0.41\mathbf{\imath} + 2.27\mathbf{\jmath}$. The final velocity after the impact is found $\mathbf{v}_C(t_f) = -0.44\mathbf{\imath} + 2.14\mathbf{\jmath}$ from the theory. The error between the theory and experiment for the normal components of the velocity is 5.4%. For the tangential component, the error is 6.7%.

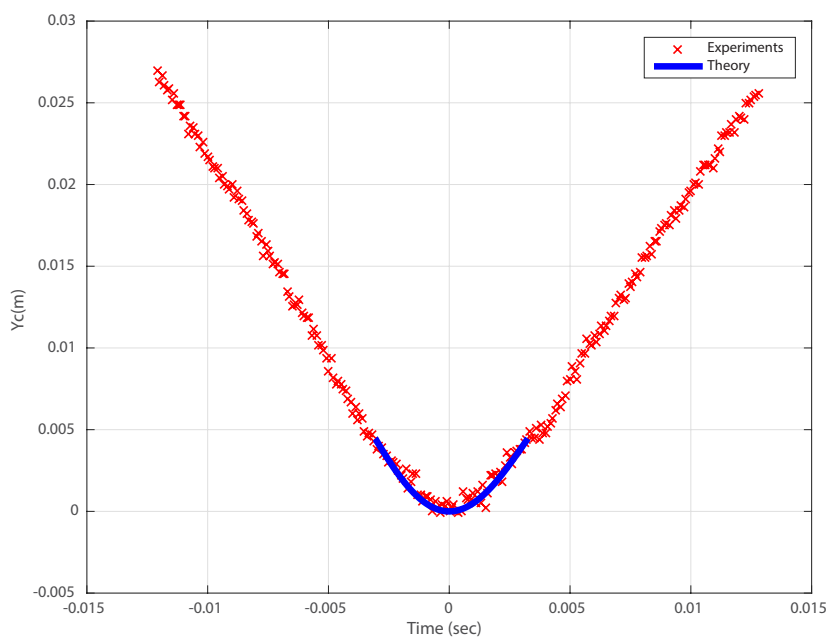

Figure 3.30: Comparison between the theory and experiment for the normal component of the displacement for the oblique impact with $\beta = 15°$.

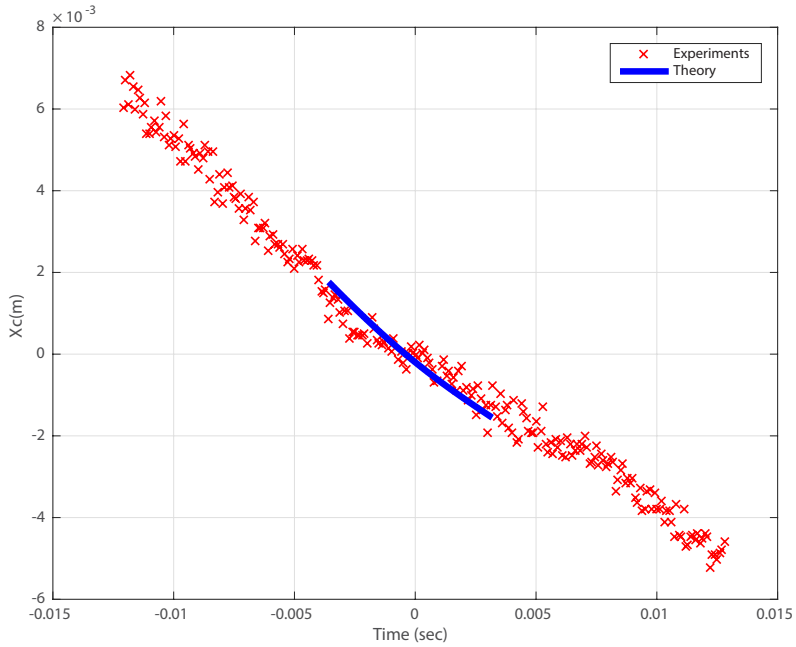

Figure 3.31: Comparison between the theory and experiment for the tangential component of the displacement for the oblique impact with $\beta = 15°$.

Oblique impact ($\beta = 30°$)

Figures 3.32 and 3.33 show displacement results when impact angle β is 30°. The initial velocity before the impact is found from the experiment $\mathbf{v}_C(t_0) = -1.81\mathbf{\imath} - 3.52\mathbf{\jmath}$. The experiment shows that the final velocity is $\mathbf{v}_C(t_f) = -1.10\mathbf{\imath} + 3.13\mathbf{\jmath}$. The final velocity after the impact is found $\mathbf{v}_C(t_f) = -1.20\mathbf{\imath} + 2.96\mathbf{\jmath}$ from the theory. The error between the theory and experiment for the normal components of the velocity is 5.2%. For the tangential component, the error is 9.3%.

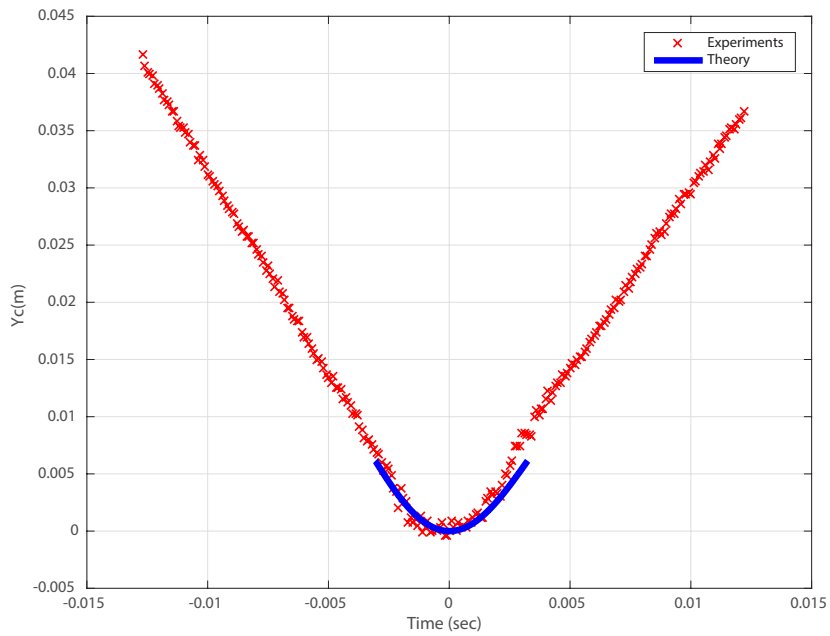

Figure 3.32: Comparison between the theory and experiment for the normal component of the displacement for the oblique impact with $\beta = 30°$.

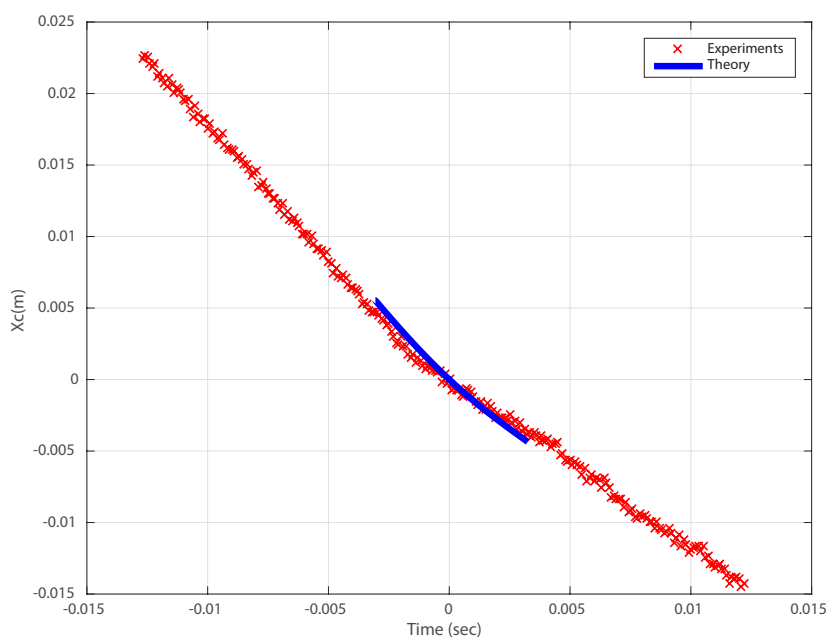

Figure 3.33: Comparison between the theory and experiment for the tangential component of the displacement for the oblique impact with $\beta = 30°$.

Oblique impact ($\beta = 45°$)

Figures 3.34 and 3.35 depict displacement results when impact angle β is 45°. The initial velocity before the impact is found from the experiment $\mathbf{v}_C(t_0) = -2.68\mathbf{\imath} - 2.96\mathbf{\jmath}$. The experiment shows that the final velocity is $\mathbf{v}_C(t_f) = -1.68\mathbf{\imath} + 2.63\mathbf{\jmath}$. The final velocity after the impact is found $\mathbf{v}_C(t_f) = -1.66\mathbf{\imath} + 2.44\mathbf{\jmath}$ from the theory. The error between the theory and experiment for the normal components of the velocity is 7.2%. For the tangential component, the error is 1.5%.

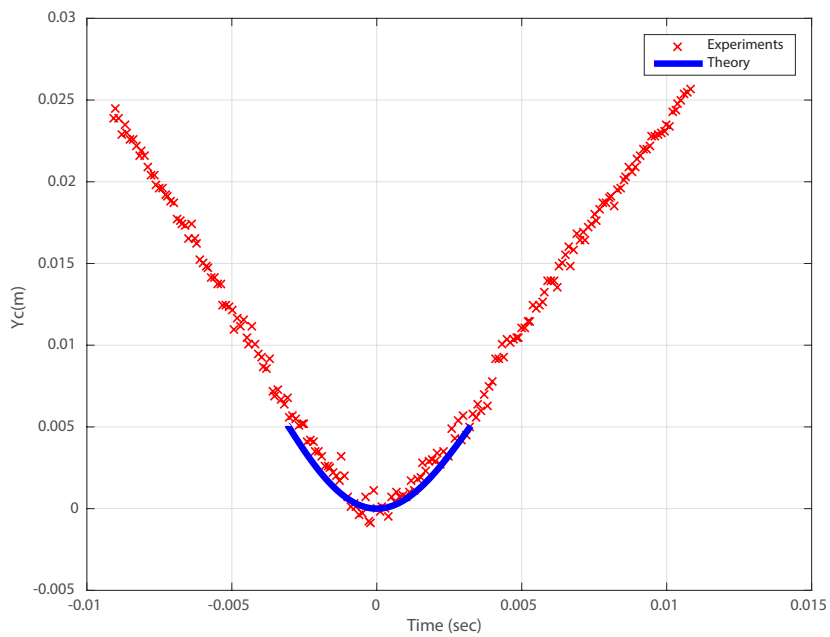

Figure 3.34: Comparison between the theory and experiment for the normal component of the displacement for the oblique impact with $\beta = 45°$.

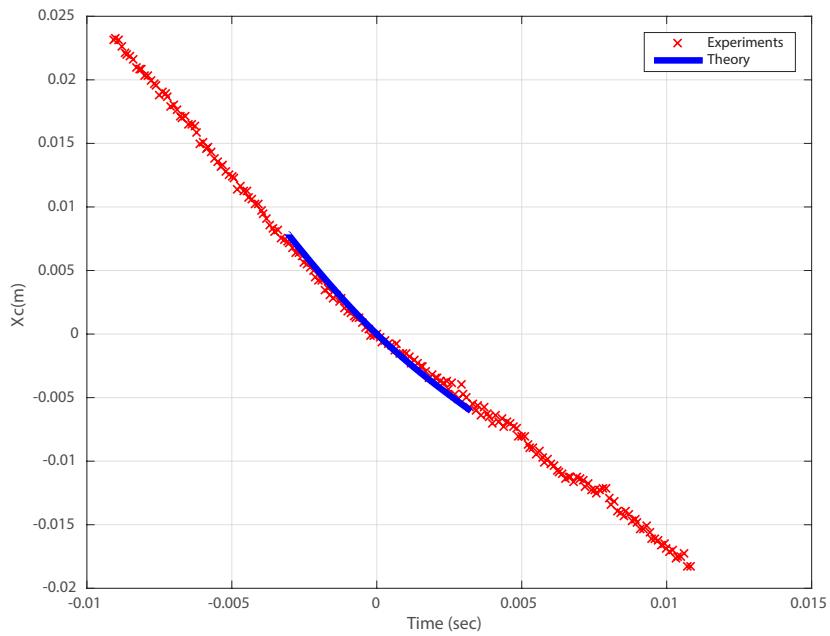

Figure 3.35: Comparison between the theory and experiment for the tangential component of the displacement for the oblique impact with $\beta = 45°$.

Oblique impact ($\beta = 57°$)

Figures 3.36 and 3.37 depict displacement results when impact angle β is 57°. The initial velocity before the impact is found from the experiment $\mathbf{v}_C(t_0) = -2.61\mathbf{\imath} - 1.73\mathbf{\jmath}$. The experiment shows that the final velocity is $\mathbf{v}_C(t_f) = -1.55\mathbf{\imath} + 1.59\mathbf{\jmath}$. The final velocity after the impact is found $\mathbf{v}_C(t_f) = -1.54\mathbf{\imath} + 1.47\mathbf{\jmath}$ from the theory. The error between the theory and experiment for the normal components of the velocity is 7.3%. For the tangential component, the error is less than 1%.

All of the experiments are compared with the theory for all oblique impact cases. The errors of the normal and tangential components of the velocity of the ball between the theory and experiments are found to be less than 10% for all cases. Theory and experiments are in good agreement.

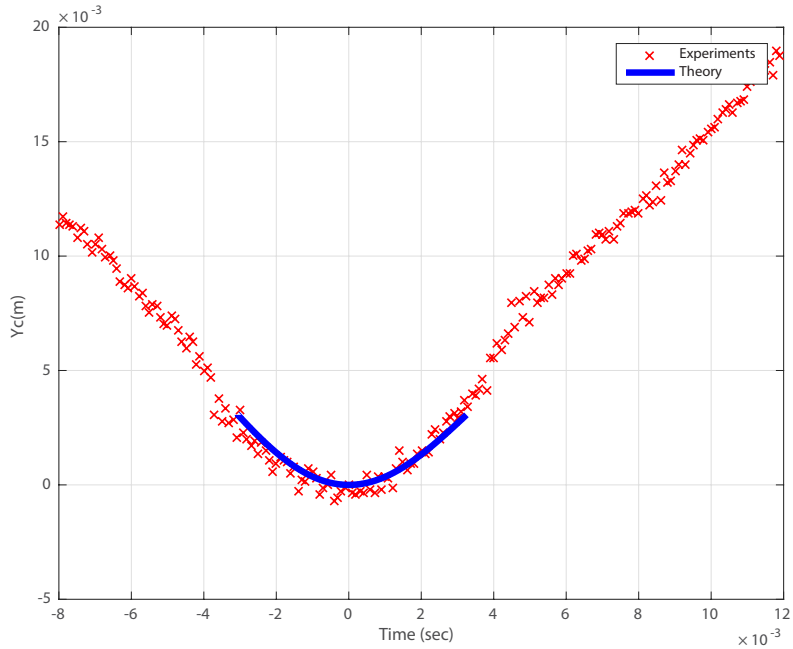

Figure 3.36: Comparison between the theory and experiment for the normal component of the displacement for the oblique impact with $\beta = 57°$.

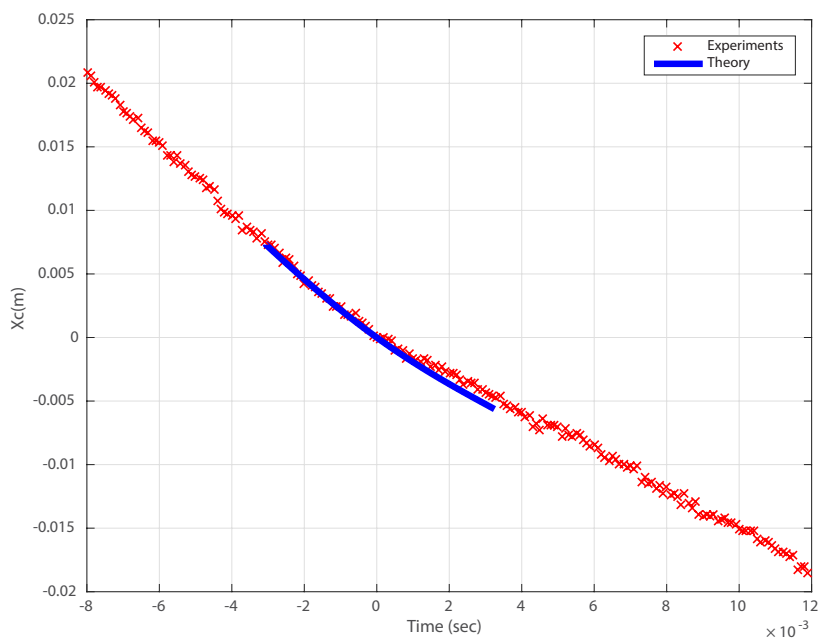

Figure 3.37: Comparison between the theory and experiment for the tangential component of the displacement for the oblique impact with $\beta = 57°$.

3.4 Discussion

The effective coefficient of friction has been found to increase with increasing impact angles. It has to be noted that this friction is assumed to be average friction throughout the impact. When the impact angle increases the ball stays in sliding regime for a longer period, which increases the coefficient of friction.

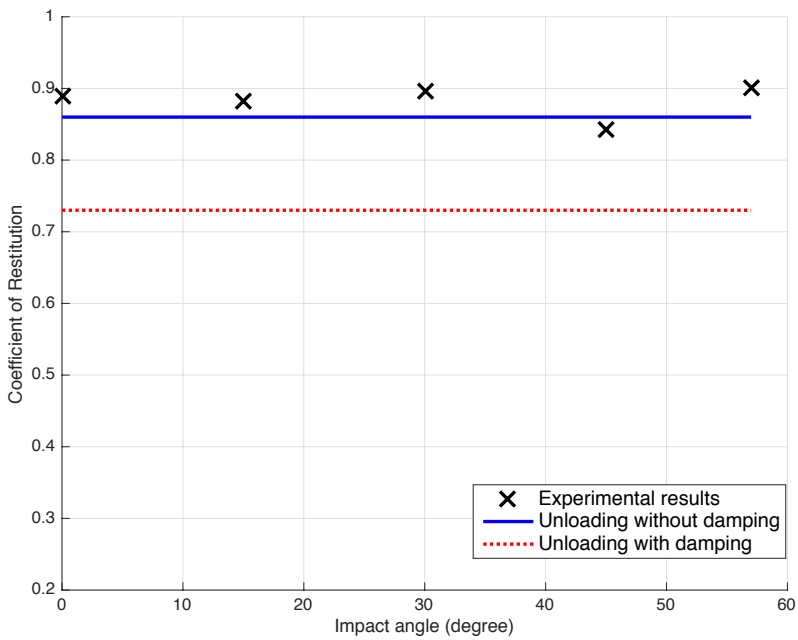

Figure 3.38: Comparison of the coefficient of restitution between the experiments and the theory.

The stiffness and damping coefficients have been used together for the compression phase. It is assumed that the recovery is fully elastic as it has been proved in contact mechanics field [42, 50, 56, 103, 104]. Therefore, damping coefficient is removed from the restitution phase. The error between the theory and experiments in terms of final velocity in normal and tangential directions increases when the restitution phase consists of the damping coefficient. For the oblique impact with $\beta = 15°$ seen in Fig.3.30 and 3.31, the error between the theory and experiment increases from 5.4% to 19.8% for the normal components of the velocity. For the tangential component, the error increases from 6.7% to 10.1%. Same

trend increment is seen for all the impact angles. It is seen from the results that the model without damping in the restitution phase works better with the experiments. This shows the proposed model matches the contact force during the impact. Figure 3.38 presents the comparison between the theory and experimental results for the coefficient of restitution. It has been seen from the result that the unloading phase with damping predicts less coefficient of restitution which doesn't match with the experiments.

3.5 Conclusion

In this study, the oblique impact of a tennis ball with a tennis racket has been analyzed theoretically and experimentally. More than 110 experiments have been done and analyzed for five different impact angles. Image processing technique has been used in order to find the displacement of the center of the ball. Experimental results show that the coefficient of restitution is constant for different impact angles and different low velocities. The effective coefficient of friction is found to increase when the impact angle increases. However, it is constant for different velocities for the same impact angle within the low initial velocity range.

A spring-damper model is used for the theory. First, normal impact experiments have been used in order to obtain the contact force coefficients. The displacement of the ball and the velocity of the ball after the impact are taken into consideration when finding the contact coefficients. The final k and b are found by averaging 15 normal impact experiments. Then, the model is extended to oblique impact case by introducing the frictional force. The effective friction force is calculated experimentally with the assumption of sliding throughout the impact. The coefficients are used for the simulation of the oblique impacts. The theory has been compared with four oblique impact cases in terms of the displacement and velocity after the impact. The simulation results are in good agreement with the experimental results.

Chapter 4

Impact of a solid rubber ball with a rigid flat

In this chapter, a solid rubber ball (lacrosse ball) impacting a wooden flat surface is studied. The impact of a sports ball with a surface has been studied by many researchers. There are some features that still needs further analysis. The behavior of the ball during the impact still attracts the researchers. This behavior is hard to compute experimentally since the impact duration is short, friction force is difficult to calculate, and most of the balls do not stay spherical; they deform during the impact.

4.1 Dynamics of the impacting ball

The lacrosse ball in contact with a wooden surface is shown in Fig.4.1. The angle of the wooden flat with the horizontal flat axis, is β. The lacrosse ball is considered as a sphere of radius R with the mass center at C. The mass of the ball is m. The contact point between the ball and the wood is T.

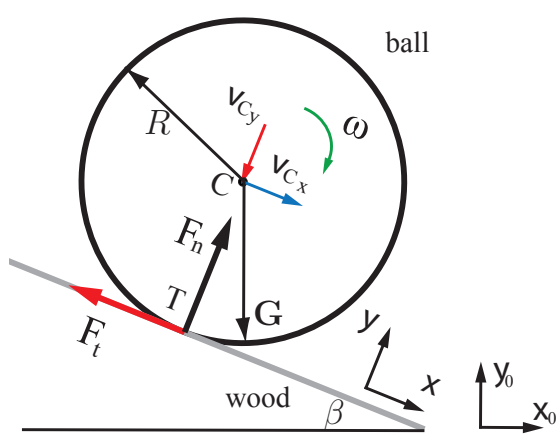

Figure 4.1: Lacrosse ball in contact with the wooden flat.

A global reference frame of unit vectors $[\,\mathbf{\imath}_0, \mathbf{\jmath}_0, \mathbf{k}_0]$ and a local reference frame, with the origin at T, of unit vectors $[\mathbf{\imath}, \mathbf{\jmath}, \mathbf{k}]$ are considered. The $x-$axis is tangential to the wooden flat and the $y-$axis is perpendicular to the wooden flat.

To characterize the instantaneous configuration of the ball, the generalized coordinates q_1, q_2, and q_3 are employed. The generalized coordinate q_1 denotes the displacement of the contact point along $x-$axis, the generalized coordinate q_2 denotes the displacement of the contact point along $y-$axis and q_3 is the radian measure of the rotation of the ball.

The position vector of the impact point T is

$$\mathbf{r}_T = q_1\,\mathbf{\imath} + q_2\,\mathbf{\jmath}, \tag{4.1}$$

and the position vector of the centroid, C is

$$\mathbf{r}_C = q_1\,\mathbf{\imath} + (q_2 + R)\,\mathbf{\jmath}. \tag{4.2}$$

The angular velocity and acceleration of the ball are

$$\boldsymbol{\omega} = \dot{q}_3\,\mathbf{k} \quad \text{and} \quad \boldsymbol{\alpha} = \ddot{q}_3\,\mathbf{k}. \tag{4.3}$$

The linear velocity and acceleration of the mass center, C are

$$\mathbf{v}_C = \mathrm{d}\,\mathbf{r}_C/\mathrm{d}\,t \quad \text{and} \quad \mathbf{a}_C = \mathrm{d}^2\mathbf{r}_C/\mathrm{d}\,t^2. \tag{4.4}$$

By neglecting the deformation of the ball,the linear velocity and acceleration of the impact point T are

$$\mathbf{v}_T = \mathbf{v}_C + \boldsymbol{\omega} \times \mathbf{r}_{CT} \quad \text{and} \quad \mathbf{a}_T = \mathbf{a}_C + \boldsymbol{\alpha} \times \mathbf{r}_{CT} + \boldsymbol{\omega} \times (\boldsymbol{\omega} \times \mathbf{r}_{CT}), \tag{4.5}$$

where $\mathbf{r}_{CT} = \mathbf{r}_T - \mathbf{r}_C$.

The total force at point T is

$$\mathbf{T} = F_t\,\mathbf{\imath} + F_n\,\mathbf{\jmath}, \tag{4.6}$$

where F_t and F_n are the tangential and normal contact forces, respectively.

For the case of a rigid ball, the equations of motion are

$$\begin{aligned} m\,\mathbf{a}_C &= \mathbf{G} + \mathbf{T}, \\ I_C\,\boldsymbol{\alpha} &= \mathbf{r}_{CE} \times \mathbf{T}, \end{aligned} \tag{4.7}$$

where $\mathbf{G} = -m\,g\,\sin\beta\,\mathbf{\imath} - m\,g\,\cos\beta\,\mathbf{\jmath}$, is the weight of the ball, I_C is the mass moment of inertia about C, and $g = 9.81$ m/s^2 is the gravitational acceleration.

4.2 Theoretical model

During the collision the contact force is applied on the ball from the flat in both the normal and tangential directions, where the tangential force can be considered as the friction force. In this model, both the normal and tangential forces during impact have been applied to the tip of the ball. A new formulation for each of these forces has been proposed. Runge-Kutta numerical method has been used to solve the equations of motion directly.

4.2.1 Normal force

The normal force can be divided into two main sub-phases, compression and restitution. The compression phase starts when the ball touches the flat and continues until the relative normal velocity of the colliding objects is zero. At the end of the compression phase, the normal contact force and the deformations are at their maximum. We have proposed that the magnitude of the normal force during the compression is given by

$$F_n = k\delta^{\frac{3}{2}} + b\mathrm{v}_{Cy}\left(-\frac{\mathbf{v}_T\cdot\mathbf{J}}{|\mathbf{v}_T\cdot\mathbf{J}|}\right), \tag{4.8}$$

where k and b are the stiffness and damping coefficients respectively, δ is the deformation of the ball, considering the flat is rigid, v_{Cy} is the velocity of the center of the ball in the y direction, and v_T is the velocity of the tip of the ball, or the velocity of the center of the contact area. The Hertzian theory is used for the first expression [33]. The damper is added in order to satisfy the energy loss during the collision, without which the coefficient of restitution would always be equal to 1.

The restitution phase starts right after the compression phase and continues until the deformation on the ball is fully recovered. This phase has been considered to be fully elastic, and given by

$$F_n = k\delta^{\frac{3}{2}}, \tag{4.9}$$

where the stiffness coefficient has the same value as during the compression phase. The elimination of the damping coefficient for the restitution phase is to solve the contradiction of a negative contact force at the end of the impact where the deformation of the ball is zero.

To find the stiffness and damper coefficients, a set of experiments have been performed. The ball is dropped vertically on a wooden surface with zero tangential and angular velocities for different initial normal velocities. The collision has been recorded with a high speed camera with 10 000 fps. The coefficient of restitution and the impact duration have been measured using the image processing techniques as explained in Chapter 2. The model has been calibrated for the stiffness and damper coefficients in order to achieve minimum error for both the coefficient of restitution and impact duration. The damper coefficient directly affects the coefficient of restitution, and the stiffness coefficient has the major effect on the impact duration. The calibration results suggests that the stiffness, $k = 875000$ N/m and damper coefficient, $b = 9.5$ N.s/m. The stiffness and damping coefficients have been measured by averaging the calibration results for 7 different initial normal velocities. The final results show less than 5% standard deviation for both the stiffness and damping coefficients, which indicates that the proposed contact model fits the real contact force during the collision.

4.2.2 Tangential force

Tangential force is considered as a friction force. The tangential force has been divided into three sub-phases during the collision: sliding, sticking and post-sliding. For a ball with positive initial tangential velocity, $\mathrm{v}_{Cx} > 0$, and zero initial angular velocity, $\boldsymbol{\omega} = 0\mathbf{k}$, that is colliding a flat with a normal velocity, v_{Cy}, toward the flat (Fig.4.1), the tangential force acts as sliding friction with:

$$F_t = \mu_k F_n(-\frac{\mathbf{v}_T.\mathbf{1}}{|\mathbf{v}_T.\mathbf{1}|}), \tag{4.10}$$

where μ_k is the kinematic coefficient of friction, F_n is the normal force, and v_T is the velocity of the contact point of the ball. The sliding friction force is in the opposite direction to the tangential component of the velocity of the contact point of the ball.

During the sliding phase because of the applied torque on the ball due to the tangential force, angular velocity of the ball will increase in the negative direction, hence the velocity of the tip of the ball will decrease (Eq. 4.7). The initial sliding phase continues until the tangential velocity of the tip of the ball reaches zero. It has to be considered that the sliding phase can continue throughout the impact; if collision ends before the tangential velocity of the tip of the ball, v_{Tx}, reaches zero. At larger values of β, the ball can slide throughout the impact. It is assumed that the sliding phase ends when v_{Tx} reaches zero. At this instant, the sticking phase starts.

We define a critical normal force as $F_c = F_n$, and it has been assumed in this model that the ball will stick to the surface when the normal force becomes greater than the critical normal force, $F_n > F_c$. During the sticking phase, the tangential force will be:

$$F_t = \mu_s F_n(-\frac{\mathbf{v}_C.\mathbf{1}}{|\mathbf{v}_C.\mathbf{1}|}), \tag{4.11}$$

where μ_s is the static friction and v_C is the velocity of the center of the ball. F_t is in the opposite direction to the tangential component of the velocity of the center of the ball. The sticking phase will end when the normal force becomes smaller than the critical normal force,

$F_n < F_c$. The post-sliding phase will then start, and the tangential force will follow Eq. 4.10. It has to be noted that the friction force is in the opposite direction of the tangential velocity of the tip. The friction force is predicted to be in the positive direction.

Figure 4.2 shows the normal contact force from the theory. The impact angle $\beta = 20°$ and initial velocity $\mathbf{v}_C(t_0) = 0.57\mathbf{\imath} - 1.69\mathbf{\jmath}$ m/s are used for the simulation. The tangential velocity of the tip starts with $\mathbf{v}_{Tx} = 0.57\mathbf{\imath}$ and decreases to zero while the ball is sliding until $t = 2.08 \times 10^{-3}$ s. At this instant, the normal force is recorded as the critical force (Fig. 4.2). The static friction will continue while the normal force is larger than the critical force. At $t = 3.31 \times 10^{-3}$ s, the normal force becomes smaller than the critical force, and the friction force will switch back to sliding. It has to be noted that the direction of the friction force will be in positive direction since the tangential velocity of the tip becomes negative during the sticking phase.

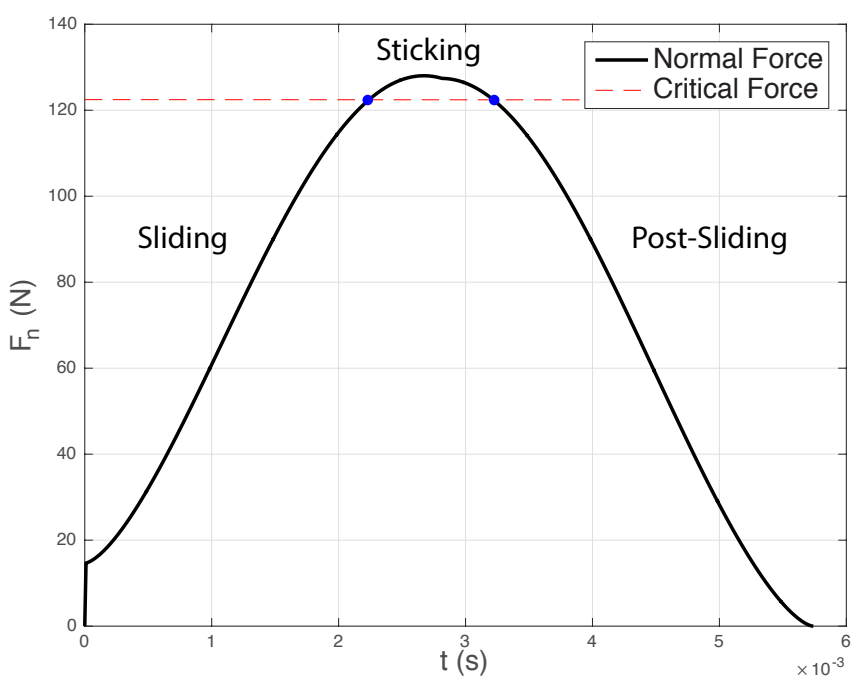

Figure 4.2: Contact force during the impact.

4.3 Experiments

The schematic of the experimental setup is shown in the Fig. 2.9. A massive metal flat holds the wooden flat with clamps. The impact angle is adjusted with a tripod that is attached to the massive flat. The impact angle is measured from the horizontal axis. The vibration during the impact is reduced by fixing the massive flat to the table.

A dropping device is built to perform consistent drops from a desired initial height. A solenoid has been used to hold and release the ball. A small metal piece has been glued to the top of the ball (the mass of the metal piece is ignored since it is very small compared to the ball). The impact has been captured by the high speed camera at 10 000 fps. The ball (e) II with random speckle pattern that is shown in Fig. 2.3 is used for the experiments.

The digital image processing method described in Chapter 2 has been used to analyze the collision. The Hough transform method has been used to track the position of the centroid of the ball. Impact angles $\beta = 20°, 30°, 40°$ have been tested with different initial velocities. The linear and angular velocities of the ball have been calculated before, during, and after the impact.

A separate experiment is done to calculate the coefficients of friction. The kinematic coefficient of friction, μ_k, and static coefficient of friction μ_s of the rubber ball on the wooden flat have been calculated experimentally from incline friction test. The angle of the wooden flat is gradually increased until the instant before the rubber moves. The critical angle is found and static coefficient of friction is measured. Several experiments are done from the angle bigger than the critical angle in order to calculate the kinematic coefficient of friction. The motion is recorded with the high speed camera. The average kinematic coefficient of friction and static coefficient of friction are calculated as 0.54 and 0.74, respectively. These coefficients are used in the theory.

Normal impact

The velocity of the center of the ball has been found using the spline interpolation of the velocity field at the centroid of the ball measured by the Hough transform method. Figure 4.3 shows the velocity of the center of the ball in the global and local coordinates for the normal impact with $\beta = 0°$. The initial impact velocity of the center of the ball is $\mathbf{v}_C(t_0) = -1.19\mathbf{J}$ m/s in the global and local coordinates. The impact starts at $t_0 = 5.4 \times 10^{-3}$ s and ends at $t_f = 10.2 \times 10^{-3}$ s. The velocity of the ball after the impact is $\mathbf{v}_C(t_f) = 1.03\mathbf{J}$ m/s.

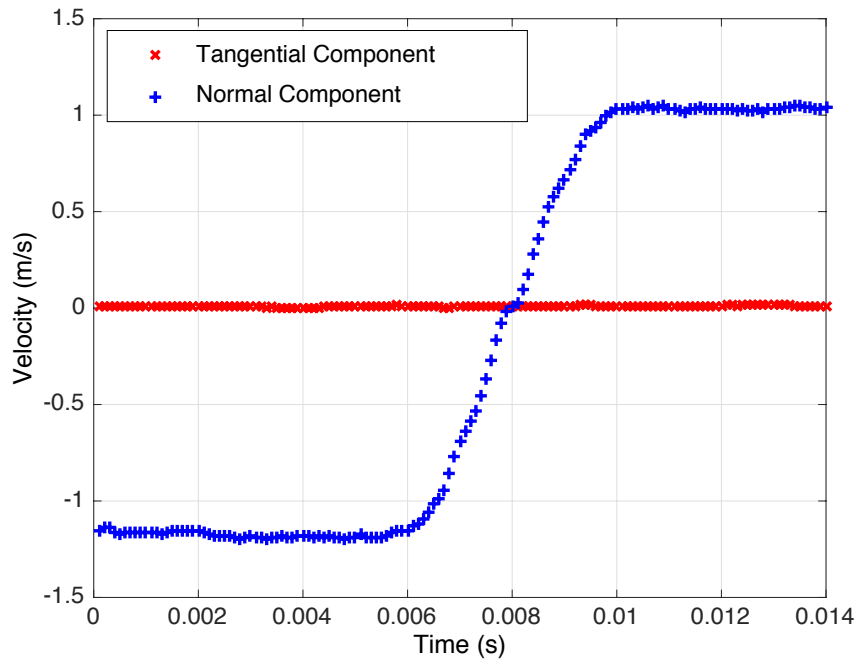

Figure 4.3: Velocity of the centroid of the lacrosse ball with the DIC method for normal impact.

Oblique impact ($\beta = 20°$)

Figure 4.4 shows the velocity of the center of the ball in the local coordinates for the oblique impact with $\beta = 20°$. The impact starts nearly at $t_0 = 2.2 \times 10^{-3}$ s. The initial impact velocity of the center of the ball is $\mathbf{v}_C(t_0) = 0.46\mathbf{I} - 1.27\mathbf{J}$ m/s in the local coordinates. At this instant, the normal velocity starts increasing until $t_f = 7.4 \times 10^{-3}$ s. The velocity

of the centroid of the ball after the impact is $\mathbf{v}_C(t_f) = 0.23\mathbf{\imath} + 1.08\mathbf{\jmath}$ m/s. An interesting phenomena is observed for the tangential velocity of the center of the ball. The tangential velocity starts decreasing after the collision starts. Then the decrease in the tangential velocity stops at nearly $t = 5.4 \times 10^{-3}$ s. After this point, the tangential velocity increases in a very slow but steady rate.

The angular velocity of the centroid of the ball during the impact is shown in Fig. 4.5 for the same experiment. An interesting phenomena happens during the impact. The magnitude of the angular velocity increases until $t = 5.4 \times 10^{-3}$ s and stays constant for a while, then decreases until the end of the impact at $t_f = 7.4 \times 10^{-3}$ s.

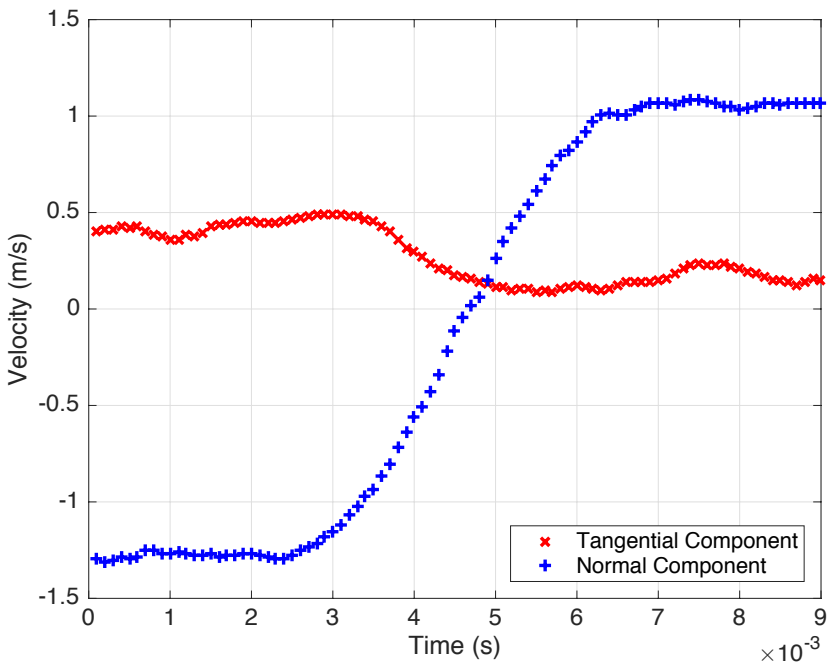

Figure 4.4: Velocity of the centroid of the lacrosse ball with the DIC method at $\beta = 20°$

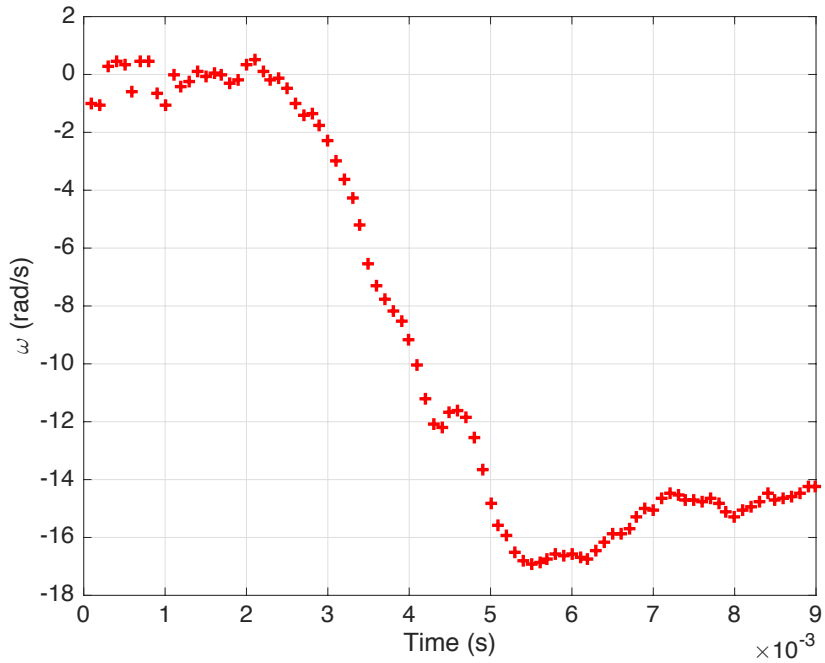

Figure 4.5: Angular velocity of the centroid of the lacrosse ball measured with the DIC method at $\beta = 20°$.

Oblique impact ($\beta = 40°$)

Figure 4.6 shows the velocity of the center of the ball in the local coordinates for the oblique impact with $\beta = 40°$. The impact starts nearly at $t_0 = 2.05 \times 10^{-3}$ s and ends nearly at $t_f = 7.7 \times 10^{-3}$ s. The initial impact velocity of the center of the ball is $\mathbf{v}_C(t_0) = 0.53\mathbf{\imath} - 0.65\mathbf{\jmath}$ m/s in the local coordinates. The velocity of the centroid of the ball after the impact is $\mathbf{v}_C(t_f) = 0.31\mathbf{\imath} + 0.58\mathbf{\jmath}$ m/s. Same trend is observed for the tangential velocity of the center of the ball for this impact angle. The tangential velocity starts decreasing after the collision starts. Then the decrease in the tangential velocity stops at nearly $t = 5.7 \times 10^{-3}$ s. After this point, the tangential velocity increases till the end of the impact.

The angular velocity of the centroid of the ball during the impact is shown in Fig. 4.7 for the same experiment. Same phenomena happens during the impact for this angle. The magnitude of the angular velocity increases until $t = 5.7 \times 10^{-3}$ s and stays constant for a short time, then decreases until the end of the impact at $t_f = 7.7 \times 10^{-3}$ s.

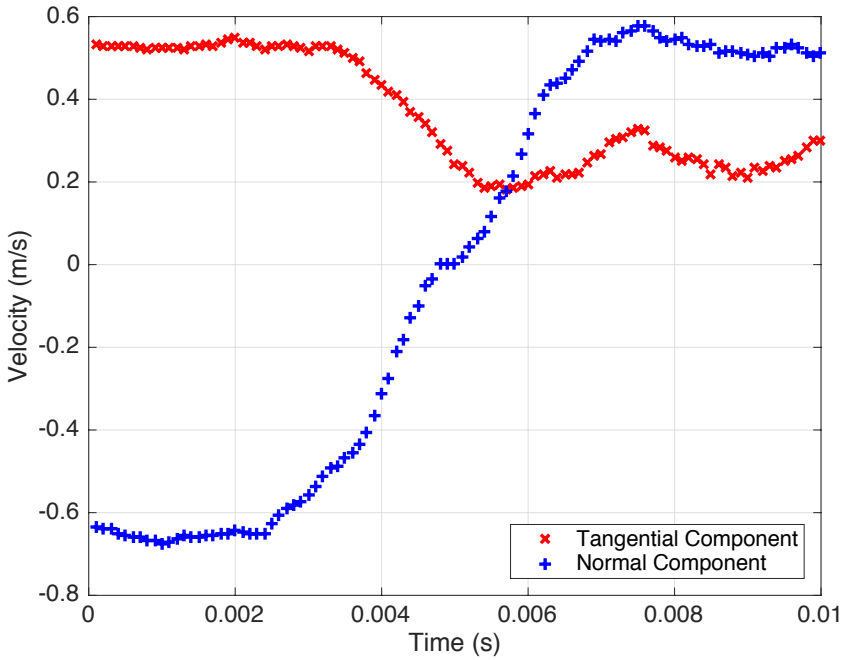

Figure 4.6: Velocity of the centroid of the lacrosse ball with the DIC method at $\beta = 40°$

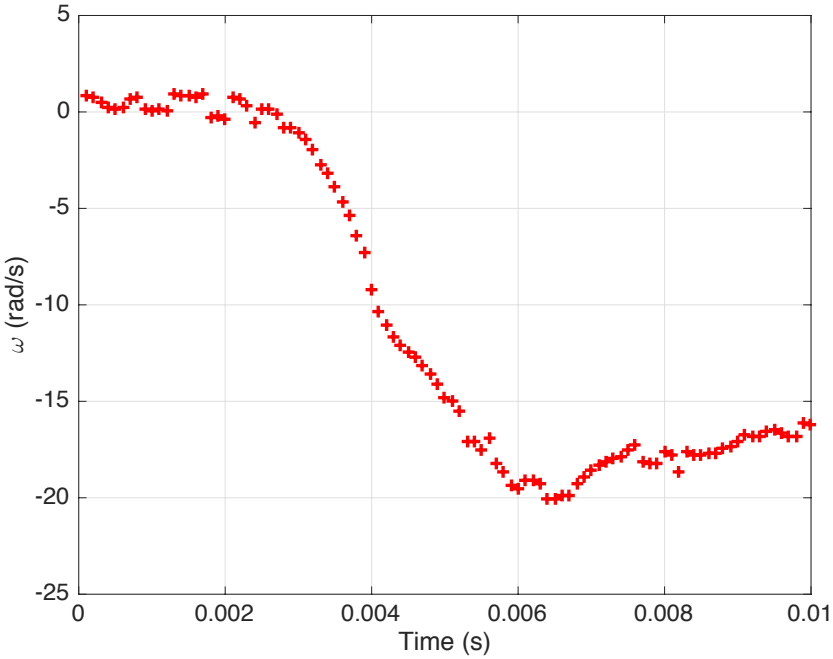

Figure 4.7: Angular velocity of the centroid of the lacrosse ball measured with the DIC method at $\beta = 40°$.

Coefficient of restitution

Same as before, the Newtonian kinematic coefficient of restitution is employed due to its simplicity. Low impact velocities from 0.8 to 3.6 m/s are tested. The results are obtained for three different impact angles $\beta = 0°, 20°, 40°$. The coefficient of restitution is compared for three different impact angles for different initial normal velocities and the result is presented in Fig. 4.8. Each shape in Fig. 4.8 presents the average result for at least three experiments with the same velocity. The results show that the coefficient of restitution is constant for the initial normal velocity range. The normal impact and oblique impact at $\beta = 20°$ show the same result $e = 0.82$. When the impact angle increases from 20° to 40°, the coefficient of restitution increases, and the average result is calculated as $e = 0.86$.

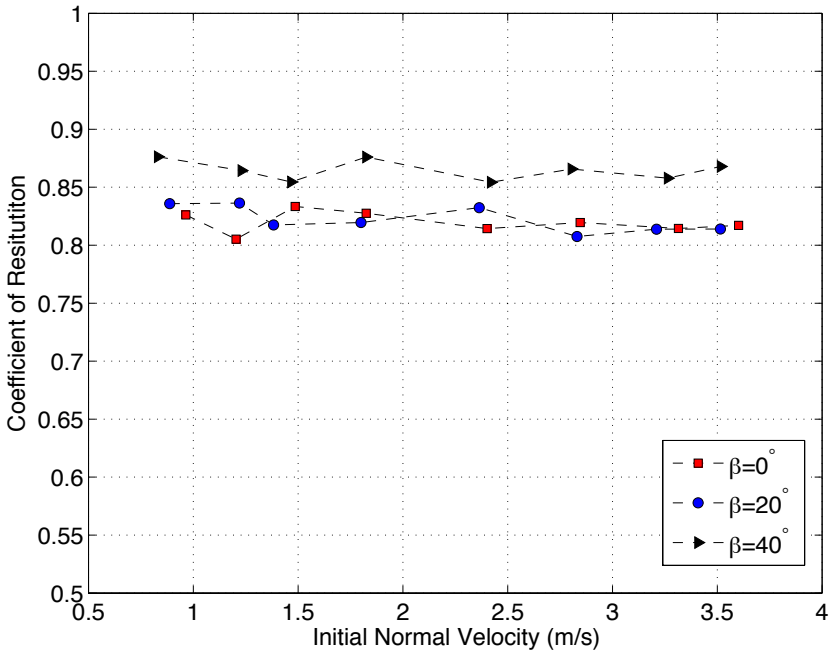

Figure 4.8: Coefficient of restitution for different initial normal velocities.

4.4 Comparing the theory with the experiments

In our proposed model, the tangential force is divided into three sub-phases: sliding, sticking and post-sliding. In our model, we have defined a critical contact force when the

tangential velocity of the tip of the ball reaches zero. The sliding phase starts first, then the sticking phase takes place when the velocity of the ball becomes zero. During the sticking phase, the normal force is greater than the critical force. The sticking phase continues until the normal force becomes smaller than the critical force. When the normal force becomes smaller than the critical normal force, post-sliding phase starts and continues till the end of the impact.

In this section, we are comparing our model with the experimental results and two other cases. The first case assumes fully sliding throughout the impact and the following equation is used for the tangential contact force

$$\mathrm{F}_t = \mu_k \, F_n \, \mathbf{1}. \tag{4.12}$$

For the fully sliding case, the ball slides along the surface; sliding friction reduces the tangential velocity of the tip and increases the angular velocity of the ball throughout the impact.

For the second case, Brody's model [11] is used. This model has two sub-phases in the tangential direction: sliding and then rolling. For the sliding-rolling model, the ball starts with sliding phase and Eq. 4.10 is used. Brody assumes that ball goes into the rolling mode when $\mathrm{v}_{Cx} = R\omega$, where v_{Cx} and ω are tangential and angular velocity of the ball, respectively. At this point, the tangential velocity of the tip of the ball is zero. The model assumes that if the ball reaches the rolling mode, the tangential contact force drops to zero, and there will not be any change in the tangential and angular velocities of the ball.

Figure 4.9 shows the comparison between the models and experimental results at $\beta = 20°$ in terms of tangential velocity of the center of the ball during the impact. Black cross shapes represent the experimental results. The experimental results show that the tangential velocity starts decreasing after the impact starts. Then the decrease in the tangential velocity stops at nearly $t = 3.2 \times 10^{-3}$ s. After this point, the tangential velocity increases till the end of the impact. During the initial sliding, all three models predict the same results,

which show decrease on the tangential velocity. The tangential velocity of the center of the ball decreases during this phase due to sliding friction applied on the contact point as seen in Fig. 4.9. For the theory, sliding phase ends at $t = 2.08 \times 10^{-3}$ s where the tangential velocity of the tip becomes zero. For the fully sliding case, the tangential velocity decreases throughout the impact. For the sliding-rolling model, the tangential velocity stays constant after the ball reaches the rolling mode as it is seen in Fig.4.9 For our model, the sticking phase starts at $t = 2.08 \times 10^{-3}$ s when the velocity of the tip is zero and continues till the critical force becomes greater than the normal force. The third phase, post-sliding, starts again at $t = 3.31 \times 10^{-3}$ s when the normal force becomes smaller than the critical normal force. The tangential velocity of the tip is in negative direction; therefore, the friction force is in the positive direction. The experimental result shows that the tangential velocity of the center of the ball after the impact is $\mathrm{v}_{Cx}(t_f) = 0.31$ m/s. The fully sliding case and sliding-rolling model predict $\mathrm{v}_{Cx}(t_f) = 0.01$, $\mathrm{v}_{Cx}(t_f) = 0.4$ m/s, respectively. The proposed model shows that $\mathrm{v}_{Cx}(t_f) = 0.26$ m/s. Our model shows better agreement with the experimental results when comparing with the other two cases. Our model is the only model which shows the increase on the tangential velocity right before the impact ends.

The experimental results show that the angular velocity increases until $t = 3.3 \times 10^{-3}$ s and stays constant for a while, then decreases until the end of the impact at $t_f = 5.6 \times 10^{-3}$ s. The angular velocity after the impact is $\omega(t_f) = 18.4$ rad/s for the experiment. The fully sliding case predicts increasing angular velocity throughout the impact, because the sliding friction reduces the tangential velocity of the center of the ball and increases the angular velocity. The fully sliding case predicts the angular velocity after the impact to be $\omega(t_f) =$ 41.2 rad/s. For the sliding-rolling model, the angular velocity is $\omega(t_f) = 12.55$ rad/s. For the sliding-rolling model, the angular velocity stays constant after the ball reaches the rolling mode. Our model shows that the angular velocity after the impact is $\omega(t_f) = 22.1$ rad/s, which shows better agreement with the experiment when compared with the other two cases.

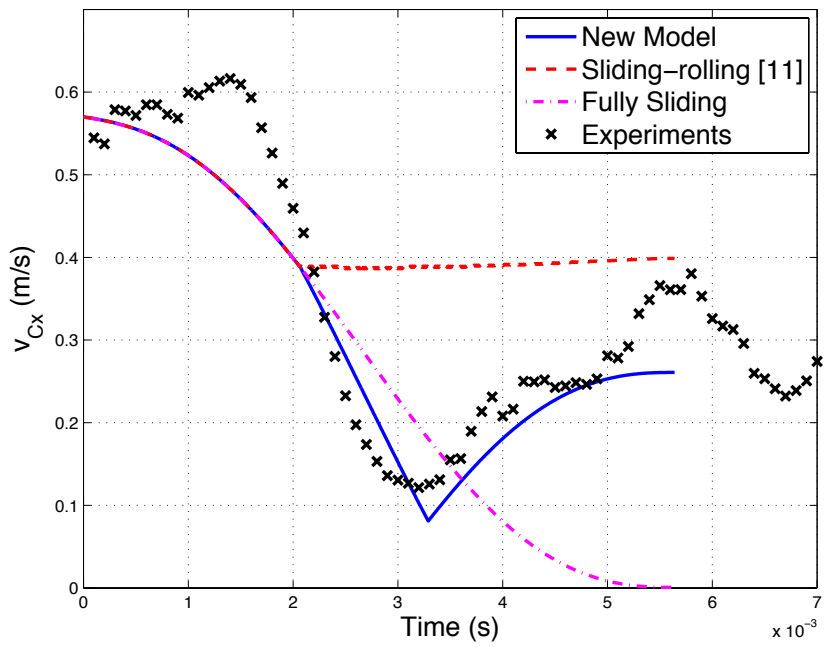

Figure 4.9: Comparing the models with the experiment at $\beta = 20°$ for the tangential velocity of the center of the ball.

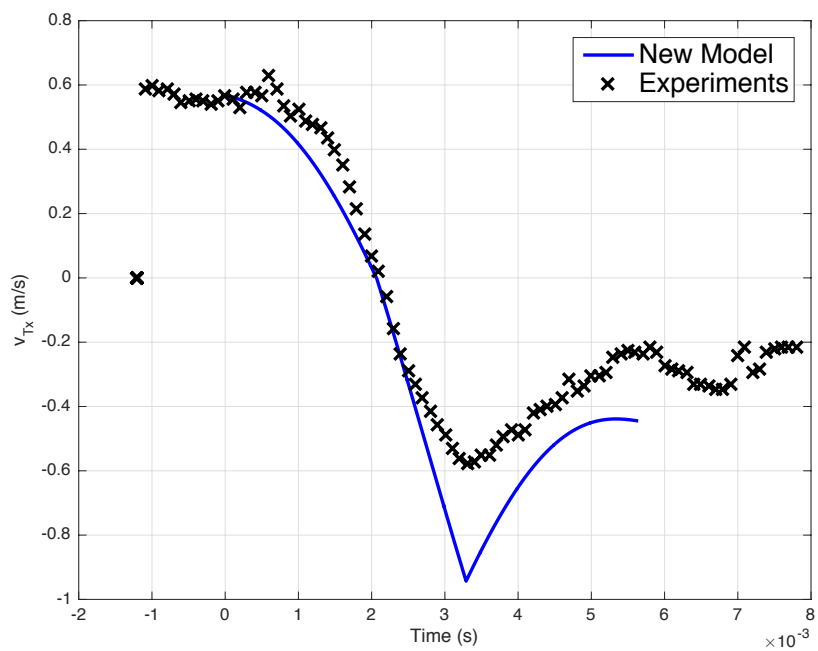

Figure 4.10: Comparing the models with the experiment at $\beta = 20°$ for the tangential velocity of the tip of the ball.

Figure 4.10 shows the tangential velocity of the tip of the ball during the impact for both theory and experiments at $\beta = 20°$. It has to be noted that the tangential velocity of the tip for the experiments is calculated using rigid body equations. For the theory, deformation on the normal direction is considered but, torsional deformation is not taken into consideration. The tangential velocity of the tip starts with 0.58 m/s and decreases to zero while the ball is sliding until $t = 2.08 \times 10^{-3}$ s as seen in Fig. 4.10. Then sticking phase starts when the tangential velocity of the tip becomes zero. At this instant the normal force is recorded as the critical force, and the friction force switches to static friction. The sticking phase ends at $t = 3.31 \times 10^{-3}$ s, and post-sliding phase starts from this moment. It has to be noted that the direction of the friction force will be in positive direction for this phase, since the velocity of the tip becomes negative during the sticking phase.

Figure 4.11 compares the results when the impact angle $\beta = 30°$ for the tangential velocity of the center of the ball. The sticking phase starts at $t = 2.16 \times 10^{-3}$ s when the velocity of the tip becomes zero end ends at $t = 3.31 \times 10^{-3}$ s. The experimental results show that tangential velocity decreases till $t = 3.1 \times 10^{-3}$ s and increases from that point till the end of the impact as it is seen in Fig. 4.11. The tangential velocity after the impact is found to be $\mathrm{v}_{Cx}(t_f) = 0.46$m/s experimentally. For this angle, the fully sliding case and sliding-rolling model predict $\mathrm{v}_{Cx}(t_f) = 0.06$, $v_t(t_f) = 0.62$ m/s, respectively. Our model predicts the tangential velocity to be $\mathrm{v}_{Cx}(t_f) = 0.49$ m/s. The angular velocity after the impact is found to be $\omega(t_f) = 29.4$ rad/s from the experiment. Our model shows that the angular velocity after the impact is $\omega(t_f) = 29.1$ rad/s. While the fully sliding case predicts $\omega(t_f) = 60.1$ rad/s , the sliding-rolling model shows $\omega(t_f) = 19.4$ rad/s. The results show that our model works better with the experiment.

The tangential velocity of the center of the ball at the impact angle $\beta = 40°$ is shown in Fig. 4.12. The sticking phase starts at $t = 2.25 \times 10^{-3}$ s when the velocity of the tip becomes zero and ends at $t = 3.22 \times 10^{-3}$ s. The experimental results show that tangential velocity decreases till $t = 3.52 \times 10^{-3}$ s and increases from that point till the end of the impact as seen

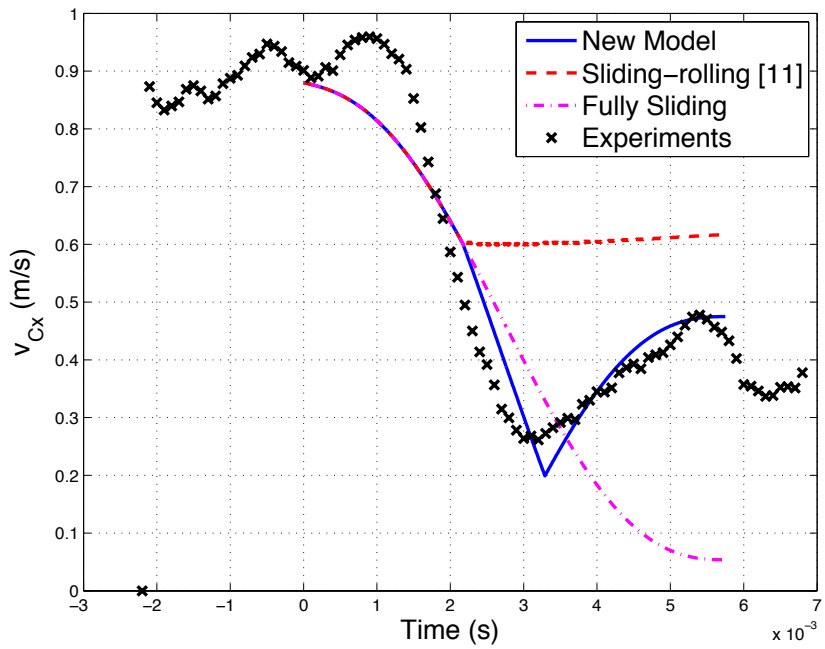

Figure 4.11: Comparing the models with the experiment at $\beta = 30°$ for the tangential velocity of the center of the ball.

in Fig. 4.12. The tangential velocity after the impact is found to be $v_{Cx}(t_f) = 0.59$ m/s from the experiment. Our model predicts the result to be $v_{Cx}(t_f) = 0.71$ m/s. Tangential velocity after the impact is $v_{Cx}(t_f) = 0.80$ m/s for the sliding-rolling model. The fully sliding case shows $v_{Cx}(t_f) = 0.12$ m/s. Our model can predict the increase on the tangential velocity right before the impact. The angular velocity after the impact is measured $\omega(t_f) = 39$ rad/s from the experiment. Our model shows $\omega(t_f) = 31.1$ rad/s. The fully sliding case and sliding-rolling model predict $\omega(t_f) = 73.8$, $\omega(t_f) = 25.1$ rad/s respectively. Our model predicts better result for this angle.

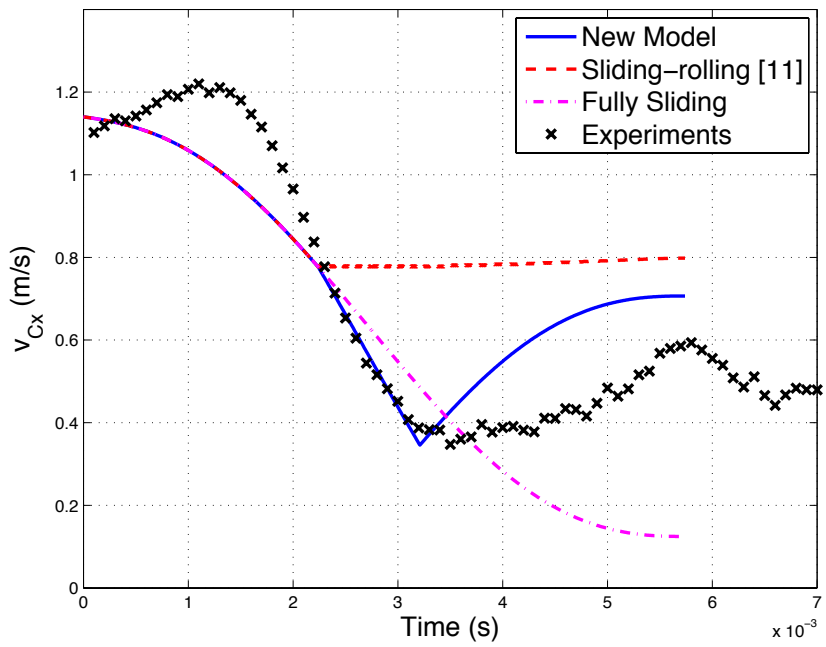

Figure 4.12: Comparing the models with the experiment at $\beta = 40°$ for the tangential velocity of the center of the ball.

4.5 Discussion and conclusion

In this study, digital image processing method described in Chapter 2 is used to measure the motion of a lacrosse ball impacting a wooden flat. The method is able to provide accurate information during the impact which enable us to study the friction behavior of the colliding bodies. The linear and angular velocities of the ball are measured before, during, and after the impact.

A theoretical model is proposed for the oblique impact of the solid rubber ball on a wooden flat. Flat is considered to be rigid, and the ball undergoes small deformation due to the low initial impact velocities. The contact force is applied on the ball from the flat in both the normal and tangential directions. Tangential force is considered to be the friction force. The normal force has been divided into two main sub-phases, compression and restitution. The compression phase consists of a nonlinear spring with the addition of linear damper to account for the energy lost. The restitution phase is considered to be fully elastic with

only a nonlinear spring. The model has three sub-phases for the tangential force; sliding, sticking and post-sliding. A critical normal force, F_c, has been defined when the tangential velocity of the tip of the ball becomes zero. The ball starts with the sliding phase. It has been assumed that the ball will stick to the surface when normal force, F_n, becomes greater than the critical force. The sticking phase will end, and third phase, post-sliding, will start when $F_n < F_c$. The model is compared with the experiments for the impact angle $\beta = 20°$, $\beta = 30°$, and $\beta = 40°$ in terms of tangential and angular velocities of the ball. The model is also compared with two other models, and the simulation results for the new model show better agreement with the experiments.

Chapter 5

Experimental study of the impact of a rod with a flat

In this study, the impact of the rounded end metal rod with a metal flat has been studied experimentally. A 3D infrared camera has been used in order to capture the motion of the rod before and after the impact. An experimental setup is built in order to measure the coefficient of restitution, the permanent deformation and angular velocity after the impact. The material properties of the rod and flat are seen in Table 5.1.

Table 5.1: The material properties of the rod and the flat

R	0.0088(m)	L	0.3048(m)
ρ	7800(kg/m^3)	g	9.81 (m/s^2)
μ	0.13	ν	0.29
E_{f}	200 (GPa)	E_{r}	200 (GPa)
S_{yf}	300 (MPa)	S_{yr}	750 (MPa)

5.1 Dynamics of the rod

The equations of motion of a rod during the oblique impact were developed using Newton-Euler equations of motion. Figure 5.1 shows the schematic of the rod during the impact. The impact angle is θ. The center of the mass is point C, and the contact point is T. The gravitational force is $\vec{G}$, the normal force during the impact is $\vec{F}_{\mathrm{n}}$, and the friction force during the impact is $\vec{F}_{\mathrm{f}}$. The friction has been considered to be continuous.

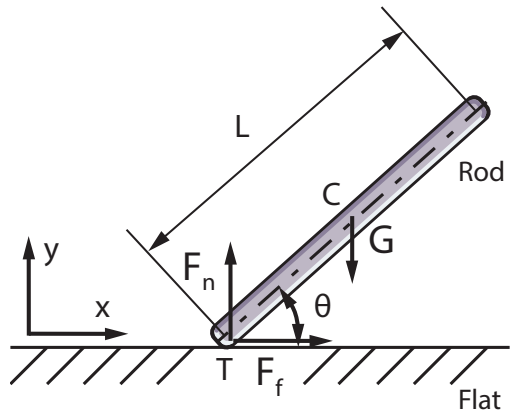

Figure 5.1: The rod impacting the flat.

The position vector of the contact point T is

$$\vec{r}_{\mathrm{T}} = x\,\hat{\imath} + \delta\,\jmath, \tag{5.1}$$

where x is the tangential displacement of the contact point and δ is the normal deformation or indentation of the rod for flattening and indentation models, respectively.

The position vector of the center of the mass of the rod is

$$\vec{r}_{\mathrm{C}} = [x\,\hat{\imath} + (\delta + R)\,\jmath] + \frac{L}{2}[\cos(\theta)\,\hat{\imath} + \sin(\theta)\,\jmath], \tag{5.2}$$

where the radius of the tip of the rod is R, and the length of the rod is L as shown in Fig. 5.1.

The angular velocity and acceleration of the rod are

$$\vec{\omega} = \dot{\theta}\,\hat{k} \quad , \quad \vec{\alpha} = \ddot{\theta}\,\hat{k}, \tag{5.3}$$

where ω is the angular velocity of the rod, and α is the angular acceleration of the rod.

The velocity of the center of the mass of the rod and contact point can be calculated as

$$\vec{v}_{\mathrm{C}} = \frac{d\vec{r}_{\mathrm{c}}}{dt} \quad , \quad \vec{v}_{\mathrm{T}} = \vec{v}_{\mathrm{C}} + \vec{\omega} \times (\vec{r}_{\mathrm{T}} - \vec{r}_{\mathrm{C}}), \tag{5.4}$$

where $\vec{v}_{\mathrm{C}}$ is the velocity of the center of the mass of the rod, and $\vec{v}_{\mathrm{T}}$ is the velocity of the tip of the rod.

The acceleration of the center of the mass of the rod and contact point can be written as

$$\vec{a}_{\mathrm{C}} = \frac{d^2\vec{r}_{\mathrm{c}}}{dt^2} \quad , \quad \vec{a}_{\mathrm{T}} = \vec{a}_{\mathrm{C}} + \vec{\alpha} \times (\vec{r}_{\mathrm{T}} - \vec{r}_{\mathrm{C}}) + \vec{\omega} \times [\vec{\omega} \times (\vec{r}_{\mathrm{T}} - \vec{r}_{\mathrm{C}})], \tag{5.5}$$

where $\vec{a}_{\mathrm{C}}$ is the acceleration of the center of the mass of the rod, and $\vec{a}_{\mathrm{T}}$ is the acceleration of the tip of the rod.

The equations of motion are

$$m\vec{\alpha}_{\mathrm{C}} = (F_{\mathrm{f}} - m\,g)\,\hat{\imath} + F_{\mathrm{n}}\jmath \quad , \quad F_{\mathrm{f}} = -\mu_{\mathrm{k}}\,F_{\mathrm{n}}\frac{\vec{v}_{\mathrm{T}}\hat{\imath}}{|\vec{v}_{\mathrm{T}}\hat{\imath}|}, \tag{5.6}$$

$$I_{\mathrm{C}}\,\vec{\alpha} = (\vec{r}_{\mathrm{T}} - \vec{r}_{\mathrm{C}}) \times (F_{\mathrm{f}}\,\hat{\imath} + F_{\mathrm{n}}\,\jmath), \tag{5.7}$$

where I_{C} is the mass moment of inertia about the center of the mass of the rod, F_{n} is the normal contact force, F_{f} is the friction force, and μ_{k} is the kinematic coefficient of friction.

5.2 Experiments

Experimental setup is seen in Fig. 5.2. The rod is held by a dropping device which consists of electromagnetic solenoids. The two electromagnetic solenoids keep the rod with the desired angle and height. The dropping device is designed in order to provide repeatable, accurate initial conditions for the experiments. A release button is controlled by the operator. The flat has been fixed on the table with clamps.

In this study, we have used an infrared camera (Optotrak 3020) (Fig. 5.3) to track the position of the rod in 3D. Three markers have been placed on different locations of the rod. One of the markers is located on the center of the rod, one is placed close to the contact point and one is attached on the top of the rod. These markers are used to track the displacement and angle of the rod. The infrared camera provides very accurate results before and after

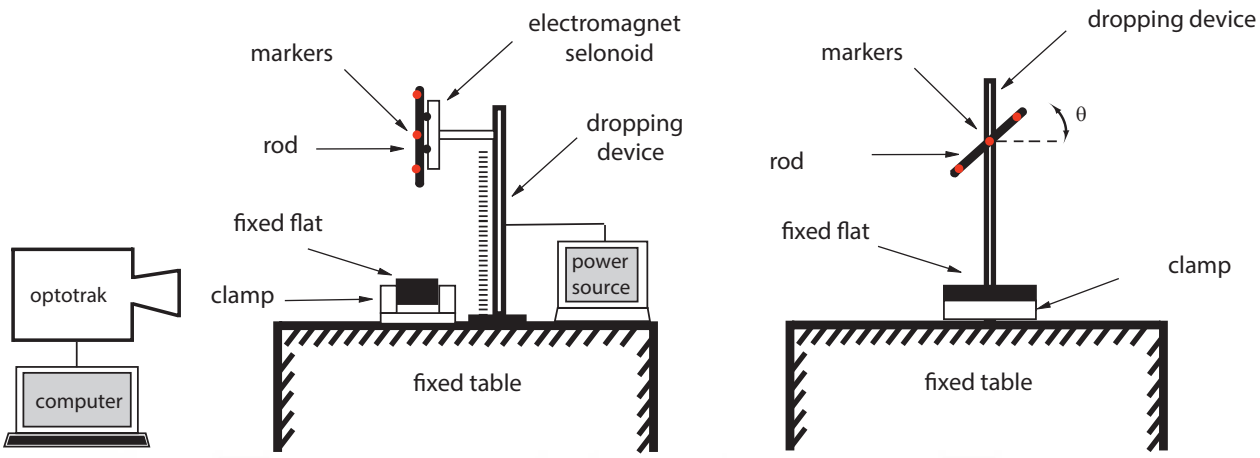

(a) (b)

Figure 5.2: Experimental setup for the impact of the rod (a) right view, (b) front view.

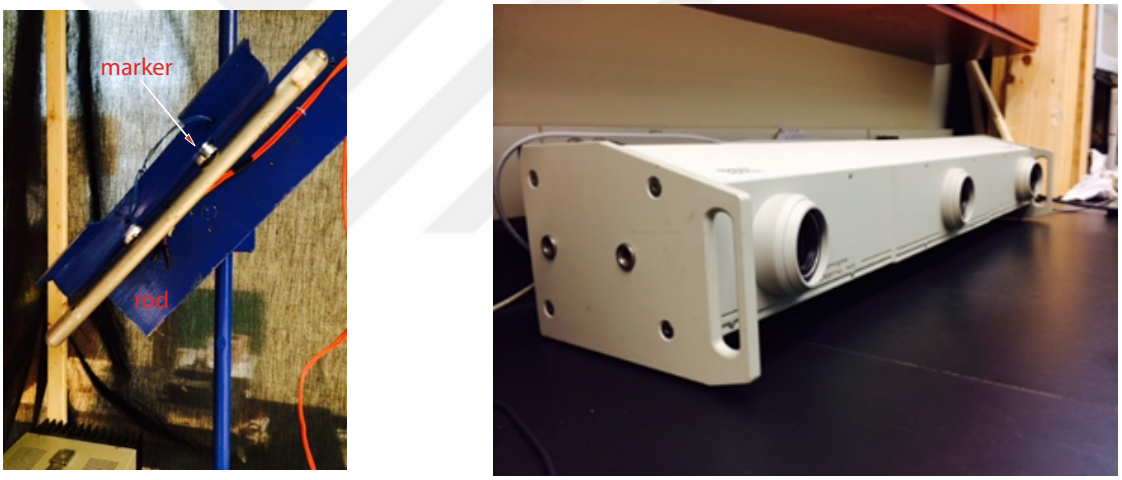

(a) (b)

Figure 5.3: Experimental setup for the impact of the rod (a) rod is held by the dropping device, (b) infrared camera.

the impact; however, it is unable provide the information during the impact due to low frequency. The motion of the rod was recorded with 500 frames per second. Low impact angles have been tasted from 0.5 to 4 m/s. At least three different drops have been done for each height. Three different impact angles, 17°, 45°, and 70° have been analyzed.

5.3 Results

The motion of the rod measured with the infrared camera has been analyzed with MATLAB software. The position of the center of the mass of the rod has been calculated before and after the impact for each heights. Both the tangential and normal component of the position of the center of the mass of the rod can be seen in Fig. 5.4 for the impact with 45° impact angle. The impact happens nearly at $t = 0.256$ s. Due to the low frequency, we were unable to obtain information during the impact. Numerical differentiation has been done in order to calculate the linear and angular velocities of the rod.

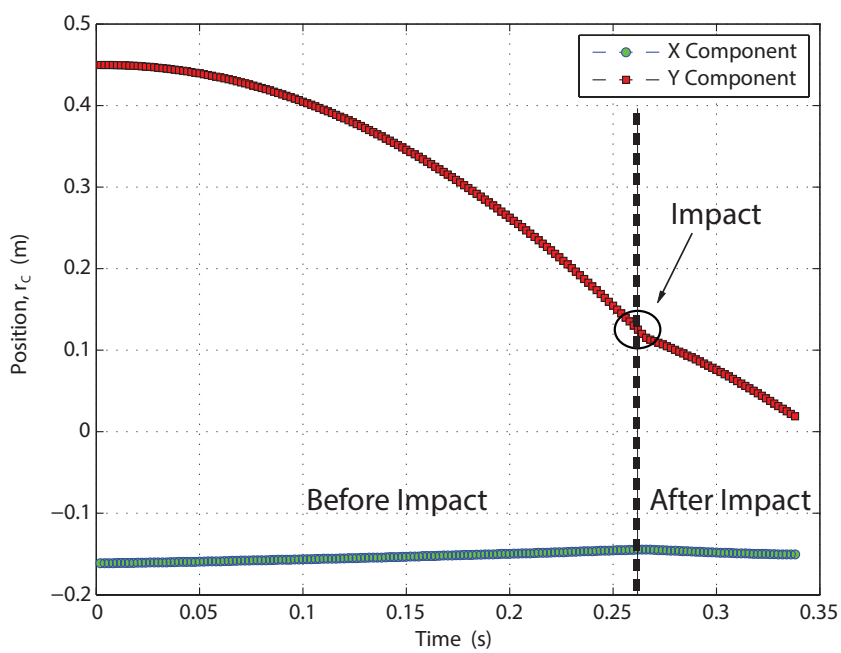

Figure 5.4: Position of the center of the rod before and after the impact for angle 45°.

The velocity of the center of the mass of the rod is calculated before and after the impact for all of the experiments. Figure 5.5 depicts the experimental results for one of the experiments with impact angle $\theta = 45°$. The impact occurs nearly at $t = 0.26$ s. The normal and tangential velocities are measured before and after the impact. The normal velocities

before and after the impact are $v^b_{\mathrm{Cn}} = -2.487$ m/s, and $v^a_{\mathrm{Cn}} = -0.855$ m/s, respectively. The tangential velocity before and after the impact are calculated as $v^b_{\mathrm{Ct}} = 0.067$ m/s, and $v^a_{\mathrm{Ct}} = -0.14$ m/s, respectively. In order to see how accurate our experimental data are , we wanted to verify the accuracy. The slope of the velocity graph is calculated and compared with gravitational acceleration, g. The experimental results show $g_{\mathrm{exp}} = 9.809$ m/s^2 which has less than 0.1% difference from the standard g for our location.

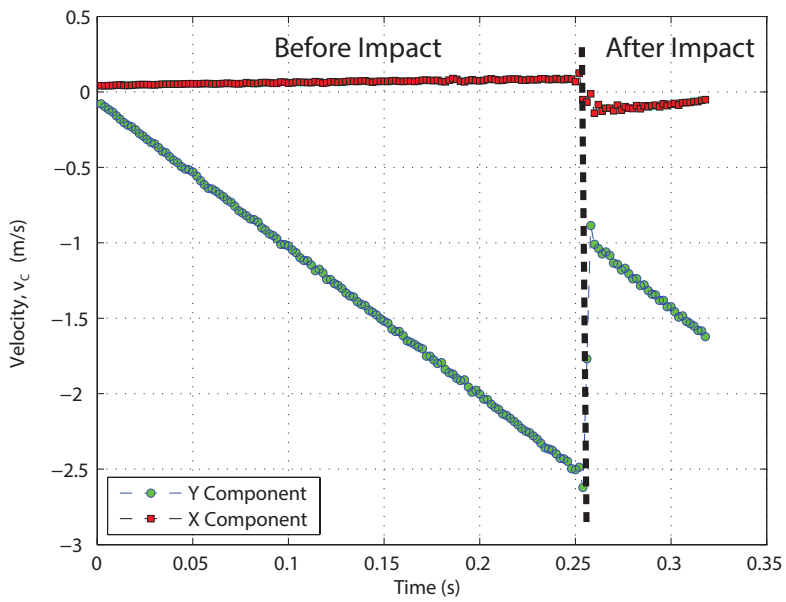

Figure 5.5: Velocity of the center of the rod before and after the impact for angle 45°.

The angle of the rod before and after the impact has been measured. Three markers have been used to calculate the position on different locations of the rod. The angle is tracked among these markers, and the average angle before and after the impact is obtained from three different results. Numerical differentiation has been done in order to calculate the angular velocity of the rod before and after the impact. Figure 5.6 presents the angular velocity of the rod before and after the impact. The rod is initially released with $\theta = 45°$, and the angle of the rod does not change until the rod impacts the flat. The angular velocity before and after the impact for the given experiment are $\omega_b = 0.02$ rad/s, and $\omega_a = -19.67$ rad/s, respectively.

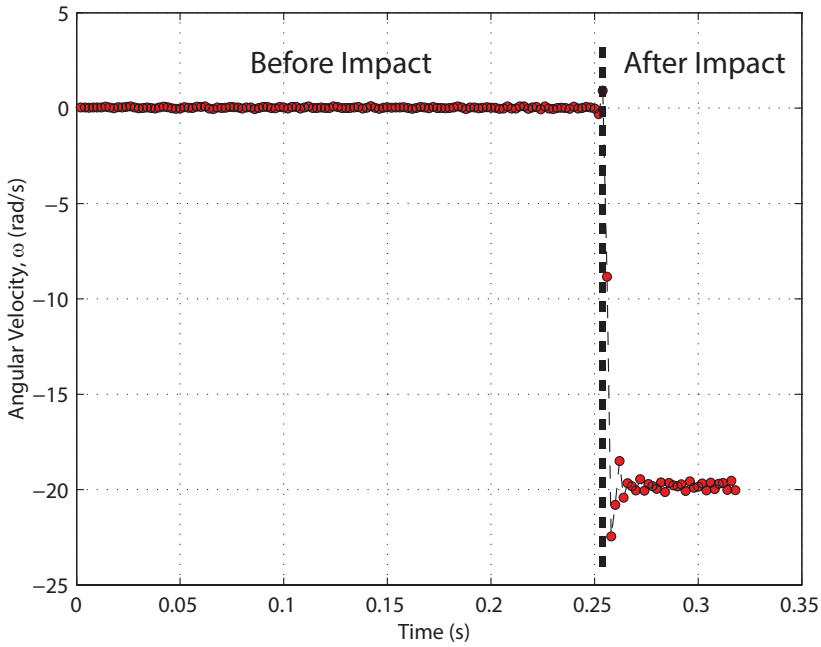

Figure 5.6: Angular velocity of the rod before and after the impact for angle 45°.

Coefficient of restitution

The kinematic coefficient of restitution is defined as the ratio between the normal rebound and normal initial velocity at the contact point. Next three results, in Figs. 5.7, 5.8, and 5.9 show the coefficient of restitution as a function of initial impact velocity for the impact angles 17°, 45°, and 70°, respectively. Each asterisk shaped marker presents the average of at least three experiments for the same height. The experiments are performed for the low initial impact velocities from 0.5 to 4 m/s. Figure 5.7 depicts all of the experimental results for the impact angle 17°. The experiments show nearly constant results for the whole velocity range with the coefficient of restitution, $e = 0.55$.

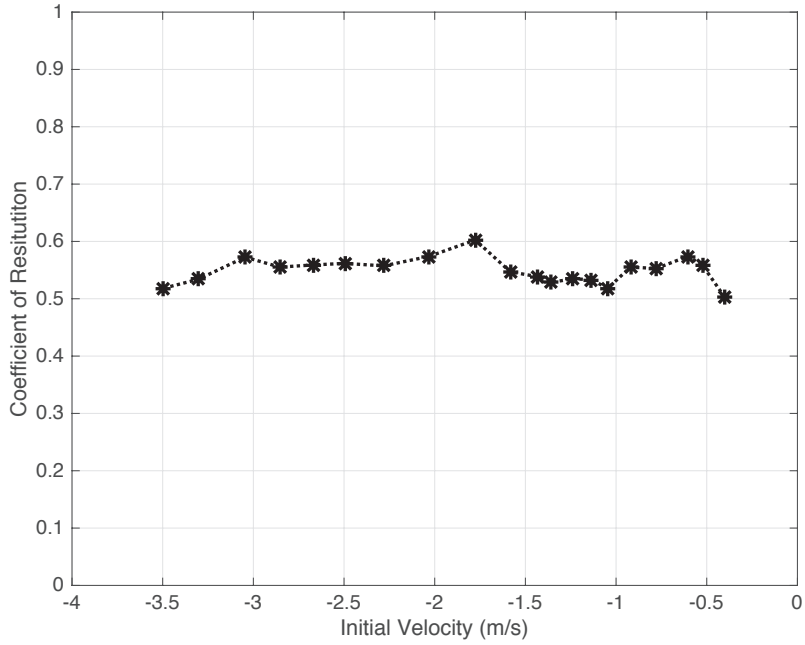

Figure 5.7: Coefficient of restitution as a function of initial impact velocity at $\theta = 17°$.

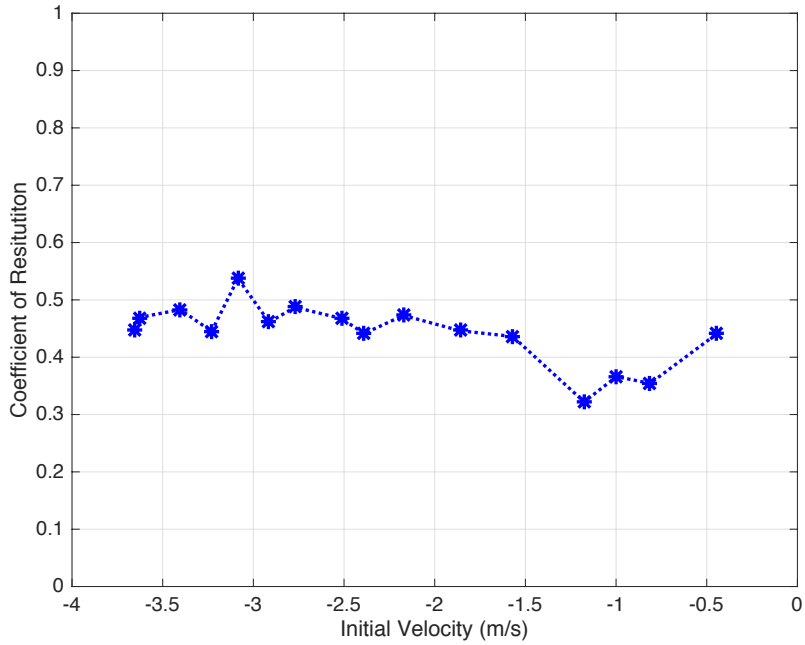

Figure 5.8: Coefficient of restitution as a function of initial impact velocity at $\theta = 45°$.

Figure 5.8 shows nearly constant results for the coefficient of restitution, $e = 0.44$ for the impact angle 45°. For the 70° impact experiments, the coefficient of restitution is found nearly $e = 0.08$ and the results are shown in Fig. 5.9.

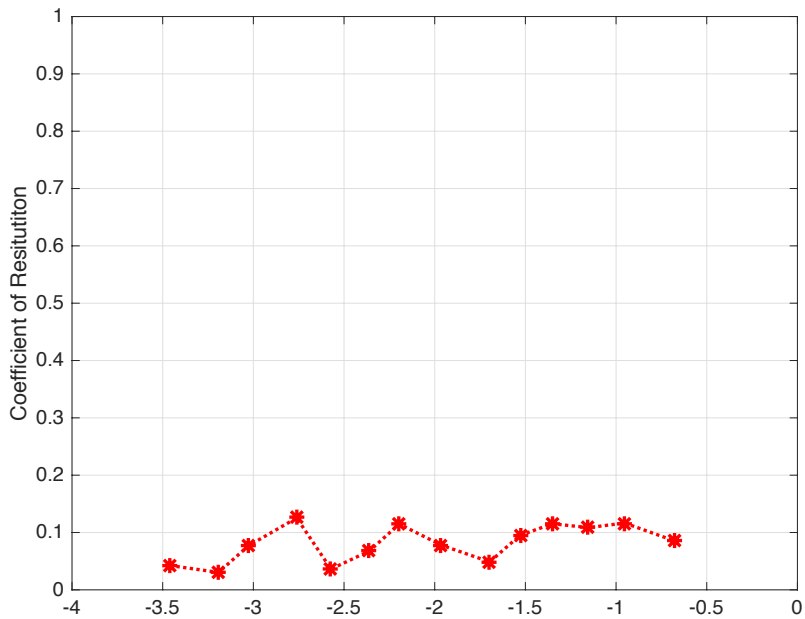

Figure 5.9: Coefficient of restitution as a function of initial impact velocity at $\theta = 70°$.

Comparison of the coefficient of restitution results for three different impact angles can be seen in Fig. 5.10. The impact with 17° and 70° show the largest and smallest coefficient of restitution results, respectively. It is observed from the experiments that coefficient of restitution slightly decreases when the impact angle increases from 17° to 45°. However, significant decrease on the coefficient of restitution is measured when the impact angle increased to 70°. This phenomenon was observed in [61] and was explained with the existence of micro impacts during single impact.

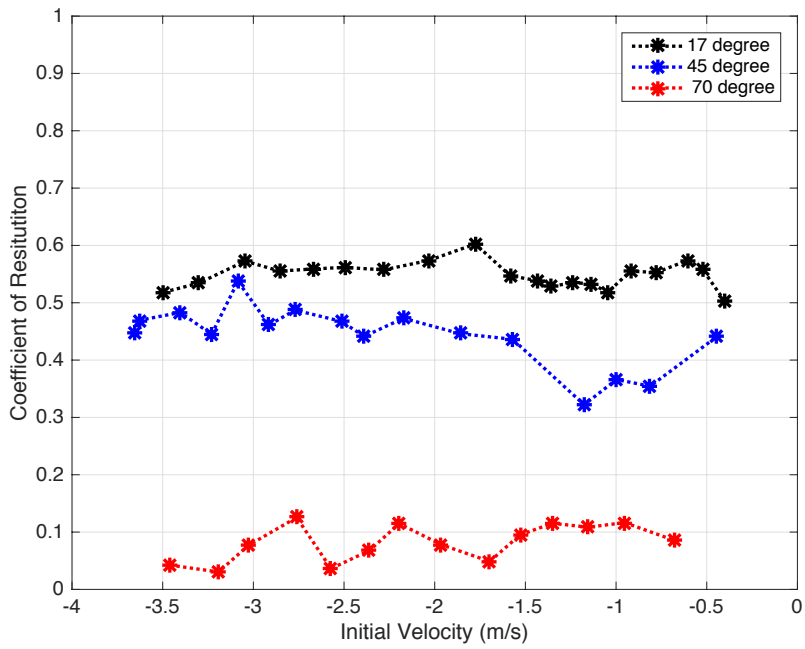

Figure 5.10: Comparision of the coefficient of restitution as a function of initial impact velocity for all of the impact angles.

Permanent deformation

The deformation after the impact has been measured for all of the impacts using the optical profilometer. Figures 5.11, 5.12, 5.13 depict the permanent deformation after the impact as a function of initial impact velocity for the impact angles 17°, 45°, and 70°, respectively. Each circle represents the average value of at least three experiments from the same height. Figure 5.14 shows the comparison of the permanent deformation for all three impact angles. The permanent deformation after the impact increases with the increase of the initial impact velocity with the same trend. For the lower initial velocities, similar permanent deformation results are obtained. It is seen from the results that, when the initial impact velocity increases, the difference in the permanent deformation increases with increasing impact angle. Larger deformations are measured for higher impact velocities for the experiments with impact angle 70° when compared with two other impact angles.

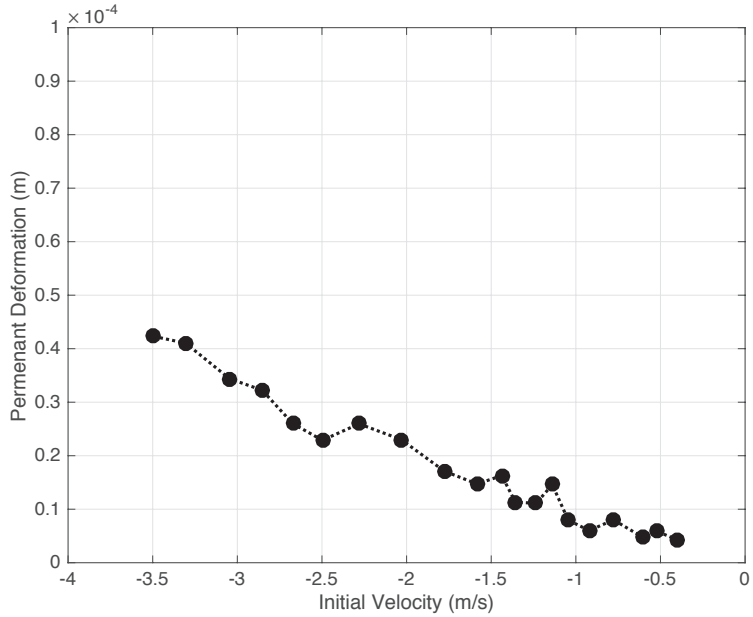

Figure 5.11: Permanent deformation as a function of initial impact velocity at $\theta = 17°$.

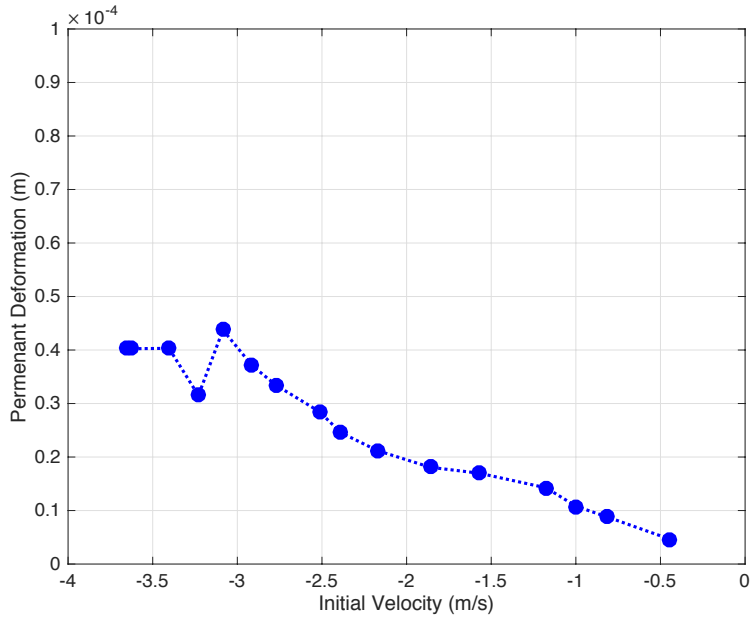

Figure 5.12: Permanent deformation as a function of initial impact velocity at $\theta = 45°$.

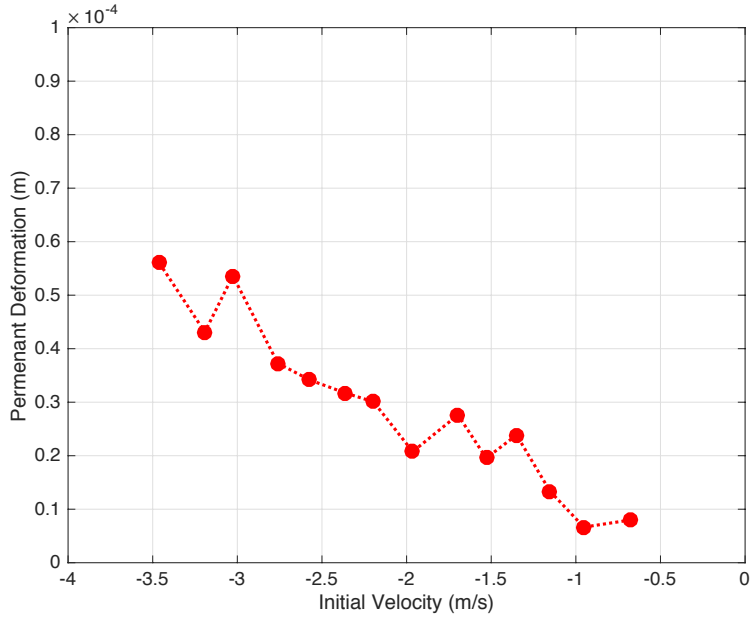

Figure 5.13: Permanent deformation as a function of initial impact velocity at $\theta = 70°$.

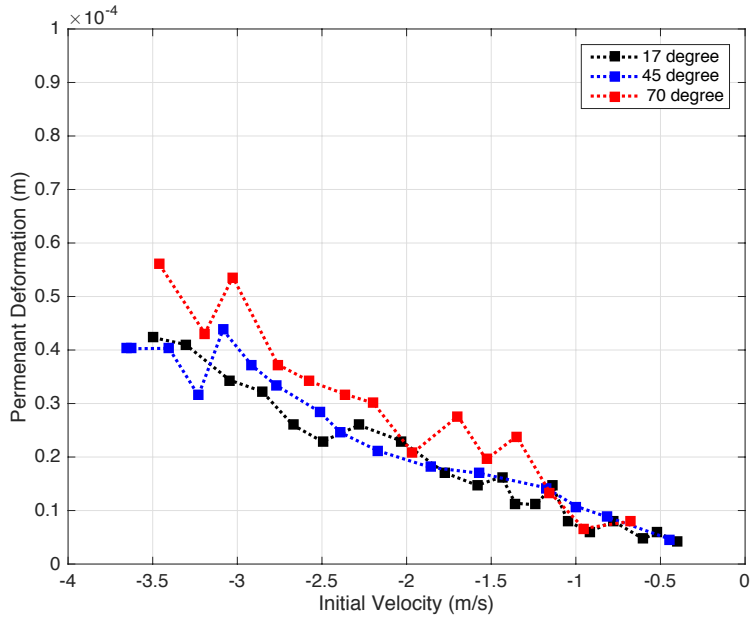

Figure 5.14: Comparison of the permanent deformation as a function of initial impact velocity for all of the impact angles.

Angular velocity after the impact

The angular motion of the rod has been measured before and after the impact. Figures 5.15 5.16 and 5.17 depict the results for the angular velocity of the rod after the impact for the impact angle $\theta = 17°$, $\theta = 45°$ and $\theta = 70°$, respectively. The same trend is seen for all the impact angles, where the angular velocity after the impact increases with increasing initial impact velocity. Figure 5.18 shows the comparison of the results for different impact angles. The result is almost identical for the angles 17° and 45°. However, the impact with 70° shows significantly smaller results compared with the other two angles.

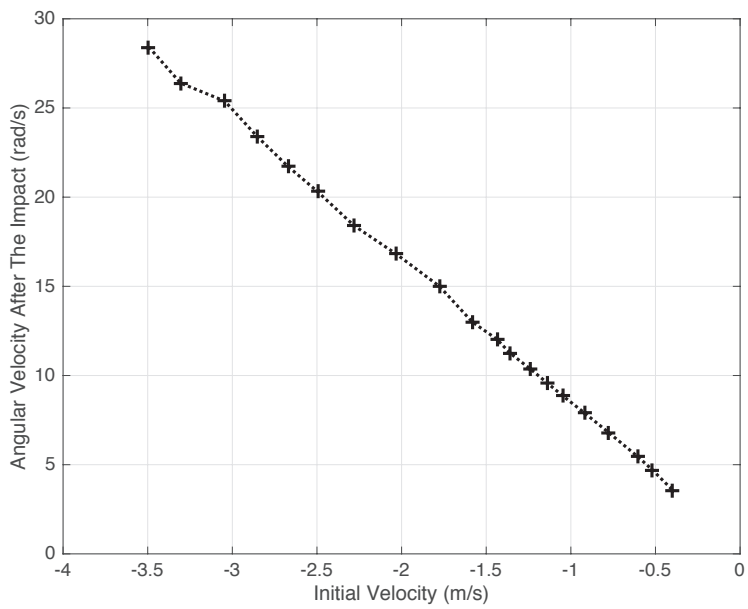

Figure 5.15: Angular velocity after the impact as a function of initial impact velocity at $\theta = 17°$.

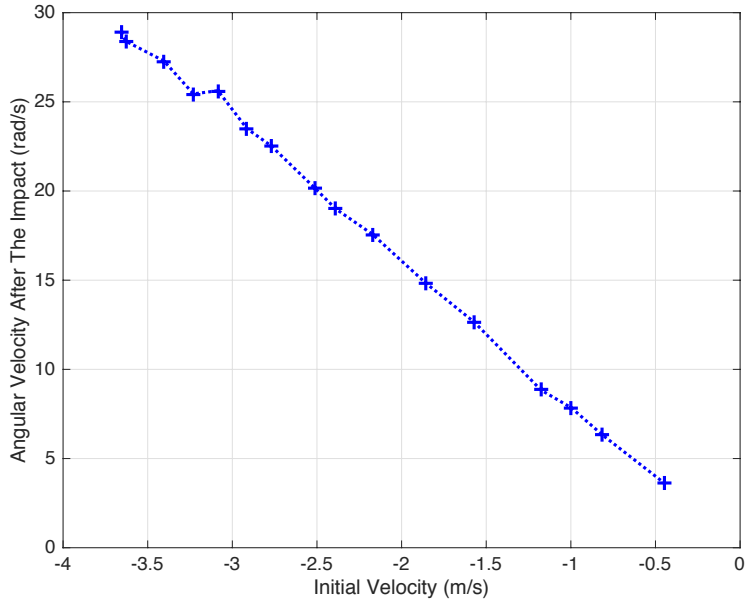

Figure 5.16: Angular velocity after the impact as a function of initial impact velocity at $\theta = 45°$.

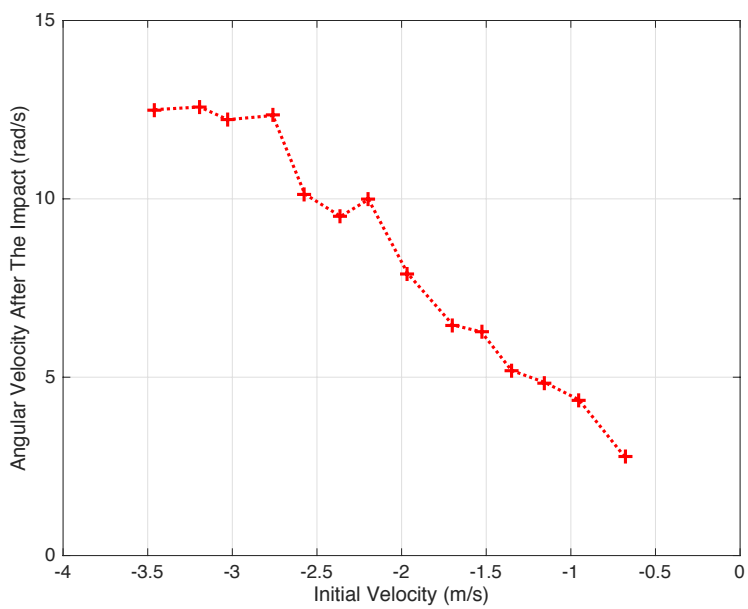

Figure 5.17: Angular velocity after the impact as a function of initial impact velocity at $\theta = 70°$.

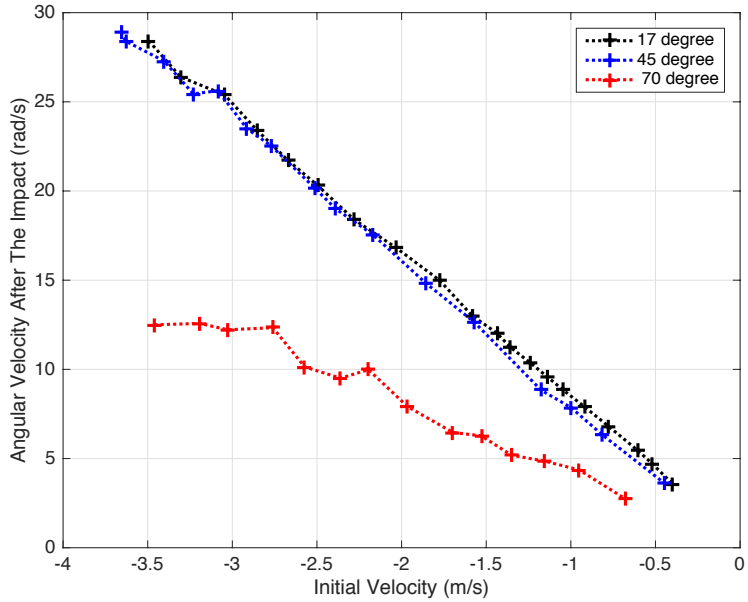

Figure 5.18: Comparison of the angular velocity after the impact as a function of initial impact velocity for all of the impact angles.

5.4 Conclusion

In this study, an experimental analysis for the impact of the rod with a flat has been done. A 3D infrared camera has been used to track the motion of the rod. The linear and angular velocity of the rod has been measured before and after the impact.

The coefficient of restitution, the permanent deformation, and the angular velocity after the impact have been measured and compared for three different impact angles 17°, 45°, and 70°. The coefficient of the restitution is found to decrease when impact angles increases. A significant decrease is measured on the coefficient of restitution when changing the impact angle from 45° to 70°. An optical profilometer is used for the deformation measurement. The permanent deformation increases with increasing initial velocities. Larger permanent deformation is measured when the impact angle increases. The angular velocity after the impact is found to increase when increasing the initial impact velocity. Similar results is seen for the impact angles 17° and 45°. However significantly smaller result is seen for 70°.

Chapter 6

Conclusions

This dissertation is dedicated to study the impact behavior of spherical objects on flexible and rigid surfaces. Firstly, a new implementation of the digital image correlation method for impact problems has been presented. To the best of knowledge, DIC methods have not been employed to calculate the motion during the impact before. Our study can be considered one of the first work that shows the potential of DIC methods to measure the linear and angular velocities during the impact. Impact problems have two main complexities for image processing method: long computation time and large displacements during the impact. Fast Fourier Transform method has been used to decrease the computation time. The spline interpolation has been applied to increase the accuracy from pixel to sub-pixel. A study has been done for the effects of the speckle pattern on the accuracy of the DIC methods for the impact problem. Balls with different size and density speckle patterns have been used in order to find the optimum pattern for the experiments. Generated videos have been used to verify the implementation of the method. It has been shown that DIC method can be used to capture the motion during the collision. This method has been used for two different impact cases: the impact of a hollow sphere with a flexible flat and the impact of a solid rubber sphere with a wooden flat. The motion of the spheres has been recorded with a high speed camera at 10,000 fps.

A new model has been presented for the impact of the hollow sphere with the flexible flat. Linear stiffness (k) and damping (b) coefficients are used for the compression phase, and the restitution phase is considered to be completely elastic. The contact coefficients k and b have been measured experimentally for the normal impact case. The image processing method has been used to calculate the linear and angular velocities of the sphere before and

after the impact. The displacement and the velocity of the sphere after the impact have been taken into consideration when finding the contact coefficients with less error. The theory has been expended to the oblique impact case and compared with the experiments for four different impact angles, and the simulation results are found to be in good agreement with the experiments.

Next, the oblique impact of a solid rubber sphere with a rigid wooden flat has been studied experimentally and theoretically. Proposed DIC method in Chapter 2 has been used to measure the linear and angular velocities of the sphere during the impact. A theoretical model has been proposed, and formulations have been given for both the normal and tangential forces. The normal force has been divided into two sub-phases: compression and restitution. A nonlinear stiffness and linear damping have been used for the compression phase, and restitution has been considered fully elastic. The stiffness and damping coefficients have been measured experimentally from the normal impact. The model is calibrated for both of the contact coefficients in terms of the impact duration and the coefficient of restitution for the least error. The tangential force is considered to be the friction force. The tangential force has been divided into three sub-phases during the impact: sliding, sticking and post-sliding. A critical normal force, F_c, has been defined when the tangential velocity of the tip of the sphere becomes zero, and it is assumed that the sphere sticks to the surface when the normal force, F_n, becomes greater than the critical force ($F_n > F_c$), and it will slide again when $F_n < F_c$. The results for the tangential and angular velocities of the centroid of the sphere calculated from the DIC method have been compared with the model, and the results are found in good agreement.

Next, the impact of a round ended rod with a metal flat has been studied experimentally, and the results are compared for three different impact angles in terms of the coefficient of restitution, angular velocity after the impact, and the permanent deformation on the flat after the impact. A 3D infrared camera has been used to analyze the motion of the rod, and the permanent deformation was measured with optical profilometer.

Bibliography

[1] I. Newton. Philosophiae naturalis principia mathematica. 1686.

[2] S. D. Poisson. Mechanics, vol. ii. *Trans. HH Harte, Longman, London*, 1817.

[3] W. J. Stronge. Unraveling paradoxial theories for rigid body collisions. *ASME Journal of Applied Mechanics*, 59:681–682, 1991.

[4] R. M. Brach. Mechanical impact dynamics: rigid body collisions. 1991.

[5] R. M. Brach. Formulation of rigid body impact problems using generalized coefficients. *International journal of engineering science*, 36(1):61–71, 1998.

[6] T. Mase and A. M. Kersten. Experimental evaluation of a 3-d hyperelastic, rate-dependent golf ball constitutive model. *The engineering of sport*, 5:238–244, 2004.

[7] D. S. Price, R. Jones, A. R. Harland, and V. V. Silberschmidt. Viscoelasticity of multi-layer textile reinforced polymer composites used in soccer balls. *Journal of materials science*, 43(8):2833–2843, 2008.

[8] R. Cross. Dynamic properties of tennis balls. *Sports Engineering*, 2:23–34, 1999.

[9] J. R. Roberts, R. Jones, and S. J. Rothberg. Measurement of contact time in short duration sports ball impacts: an experimental method and correlation with the perceptions of elite golfers. *Sports Engineering*, 4(4):191–203, 2001.

[10] R. Garwin. Kinematics of an ultraelastic rough ball. *American Journal of Physics*, 37(1):88–92, 1969.

[11] H. Brody. That's how the ball bounces. *Physics Teacher*, 22(8):494–97, 1984.

[12] R. Cross. Effects of friction between the ball and strings in tennis. *Sports Engineering*, 3(2):85–97, 2000.

[13] R. Cross. Grip-slip behavior of a bouncing ball. *American Journal of Physics*, 70(11):1093–1102, 2002.

[14] R. Cross. Measurements of the horizontal and vertical speeds of tennis courts. *Sports Engineering*, 6(2):95–111, 2003.

[15] N. Maw, J. R. Barber, and J. N. Fawcett. The oblique impact of elastic spheres. *Wear*, 38(1):101–114, 1976.

[16] S. J. Haake, M. J. Carre, and S. R. Goodwill. The dynamic impact characteristics of tennis balls with tennis rackets. *Journal of sports sciences*, 21(10):839–850, 2003.

[17] R. J. Dignall and S. J. Haake. Analytical modelling of the impact of tennis balls on court surface. In *Tennis science and technology conference*, pages 155–162. Blackwell, 2000.

[18] S. R. Goodwill, R. Kirk, and S. J. Haake. Experimental and finite element analysis of a tennis ball impact on a rigid surface. *Sports engineering*, 8(3):145–158, 2005.

[19] R. Cross. Measurements of the horizontal coefficient of restitution for a superball and a tennis ball. *American Journal of Physics*, 70(5):482–489, 2002.

[20] S. R. Goodwill and S. J. Haake. Spring damper model of an impact between a tennis ball and racket. *Proceedings of the Institution of Mechanical Engineers, part C: Journal of mechanical engineering science*, 215(11):1331–1341, 2001.

[21] S. R. Goodwill and S. J. Haake. Modelling of tennis ball impacts on a rigid surface. *Proceedings of the Institution of Mechanical Engineers, part C: Journal of mechanical engineering science*, 218(10):1139–1153, 2004.

[22] M. J. Carre, D. M. James, and S. J. Haake. Impact of a non-homogeneous sphere on a rigid surface. *Proceedings of the Institution of Mechanical Engineers, part C: Journal of mechanical engineering science*, 218(3):273–281, 2004.

[23] S. Yang, A. Fafitis, and A. Wiezel. Nonlinear impact model of a tennis racket and a ball. *Journal of mechanical science and technology*, 26(2):315–321, 2012.

[24] H. Ghaednia, O. Cermik, and D. B. Marghitu. Experimental and theoretical study of the oblique impact of a tennis ball with a racket. *Proceedings of the Institution of Mechanical Engineers, Part P: Journal of Sports Engineering and Technology*, page 1754337114567490, 2015.

[25] R. Cross. Impact behavior of hollow balls. *American Journal of Physics*, 82(3):189–195, 2014.

[26] R. Cross. Oblique bounce of a rubber ball. *Experimental Mechanics*, 54(9):1523–1536, 2014.

[27] R. Cross. Impact behavior of a superball. *American Journal of Physics*, 83(3):238–248, 2015.

[28] M. Hubbard and W. J. Stronge. Bounce of hollow balls on flat surfaces. *Sports Engineering*, 4(2):49–61, 2001.

[29] T. Allen, S. Goodwill, and S. Haake. Experimental validation of a finite-element model of a tennis racket string-bed (p21). In *The Engineering of Sport 7*, pages 115–123. Springer, 2008.

[30] T. Allen, S. Haake, and S. Goodwill. Comparison of a finite element model of a tennis racket to experimental data. *Sports engineering*, 12(2):87–98, 2009.

[31] T. Allen, S. Haake, and S. Goodwill. Effect of friction on tennis ball impacts. *Proceedings of the Institution of Mechanical Engineers, Part P: Journal of Sports Engineering and Technology*, 224(3):229–236, 2010.

[32] A. Rezaei, R. Verhelst, W. Van Paepegem, and J. Degrieck. Finite element modelling and experimental study of oblique soccer ball bounce. *Journal of sports sciences*, 29(11):1201–1213, 2011.

[33] C. Hertz. Üher die berührung fester elastischer körper (on the contact of elastic solids). *Journal fur die Reine und Andegwandte Mathematik*, 92:156–171, 1882.

[34] JA Brinell. Way of determining the hardness of bodies and some applications of the same. *Teknisk Tidskrift*, 5:69, 1900.

[35] E. Meyer. Investigations of hardness testing and hardness. *Phys. Z*, 9:66, 1908.

[36] D. Tabor. A simple theory of static and dynamic hardness. *Proceedings of the Royal Society of London, Series A*, 192:247–274, 1948.

[37] D. Tabor. The hardness of metals. Clarendon Press, Oxford, UK, 1951.

[38] K.L. Johnson. Contact mechanics. pages 154–179. Cambridge, Cambridge University Press, 1985.

[39] K. Komvopoulos. Finite element analysis of a layered elastic solid in normal contact with a rigid surface. *Journal of tribology*, 110(3):477–485, 1988.

[40] K. Komvopoulos. Elastic-plastic finite element analysis of indented layered media. *Journal of Tribology*, 111(3):430–439, 1989.

[41] N. Ye and K. Komvopoulos. Indentation analysis of elastic-plastic homogeneous and layered media: Criteria for determining the real material hardness. *Journal of Tribology*, 125(4):685–691, 2003.

[42] I. Kogut and K. Komvopoulos. Analysis of the spherical indentation cycle for elastic-perfectly plastic solids. *Journal of Material Research*, 19(12):3641, 2002.

[43] R. L. Jackson, H. Ghaednia, and S. Pope. A solution of rigid–perfectly plastic deep spherical indentation based on slip-line theory. *Tribology Letters*, 58(3):1–7, 2015.

[44] M. R. W. Brake. An analytical elastic plastic contact model with strain hardening and frictional effects for normal and oblique impacts. *International Journal of Solids and Structures*, 62:104–123, 2015.

[45] K .L. Johnson. Experimental determination of the contact stresses between plastically deformed cylinders and spheres. *Engineering Plasticity, Cambridge University Press. Cambridge*, pages 341–361, 1968.

[46] L. Y. Li, C. Y. Wu, and C. Thornton. A theoretical model for the contact of elasto-plastic bodies. *Journal of Mechanical Engineering Science*, 216(4):421–431, 2002.

[47] C. Thornton and Z. Ning. Oblique impact of elasto-plastic spheres. *Proc. 1st int. Particle Technology Forum*, 2:14–19, 1994.

[48] C. Thornton. Coefficient of restitution for collinear collisions of elastic-perfectly plastic spheres. *ASME Journal of Applied Mechanics*, 65:383–354, 1997.

[49] C. Wu, L. Y. Li, and C. Thornton. Energy dissipation during normal impact of elastic and elastic-plastic spheres. *International Journal of Impact Engineering*, 32(1):593–604, 2005.

[50] L. Kogut and I.Etsion. Elastic-plastic contact analysis of a sphere and a rigid flat. *ASME Journal of Applied Mechanics*, 69(5):657–662, 2002.

[51] I. Etsion, Y. Klingerman, and Y. Kadin. Unloading of an elastic-plastic loaded spherical contact. *International Journal of Solid Structures*, 42(13):3716–3729, 2005.

[52] R. L. Jackson and I. Green. A finite element study of elasto-plastic hemispherical contact against a rigid flat. *ASME Journal of Tribology*, 127(2):343–354, 2005.

[53] M. R. Brake. An analytical elastic-perfectly plastic contact model. *International Journal of Solid Structures*, 49:3129–3141, 2012.

[54] O. Cermik, H. Ghaednia, and D. B. Marghitu. Analytical study of the oblique impact of a rod with a flat using an elasto-plastic contact model. *Applied Mechanics & Materials*, 801, 2015.

[55] H. Ghaednia, S. A. Pope, R. L. Jackson, and D. B. Marghitu. A comprehensive study of the elasto-plastic contact of a sphere and a flat. *Tribology International*, 93:78–90, 2016.

[56] W. J. Stronge. Rigid body collisions with friction. *Proceedings of the Royal Society of London*, pages 169–181, 1990.

[57] W. J. Stronge. Energy dissipated in planar collision. *ASME Journal of Applied Mechanic*, 61:605–611, 1992.

[58] A. H Kharaz, D. A. Gorham, and A .D. Salman. Accurate measurement of particle impact parameters. *Measurement Science Technology*, 10:31, 1999.

[59] R.L. Jackson, I. Green, and D.B. Marghitu. Predicting the coefficient of restitution impacting elastic-perfectly plastic spheres. *Journal of Nonlinear Dynamics*, 60(3):217–229, 2010.

[60] D. B. Marghitu, D. Cojocaru, and R. L. Jackson. Elasto-plastic impact of a rotating link with a massive surface. *International journal of Mechanical Sciences*, 53:309–315, 2011.

[61] D. Stoianovici and Y. Hurmuzlu. A critical study of the applicability of rigid-body collision theory. *Journal of Applied Mechanics*, 63(2):307–316, 1996.

[62] H. Minamoto and S. Kawamura. Effects of material strain rate sensitivity in low speed impact between two identical spheres. *International Journal of Impact Engineering*, 36(5):680–686, 2009.

[63] A. H. Kharaz, D. A. Gorham, and A. D. Salman. Accurate measurement of particle impact parameters. *Measurement Science and Technology*, 10(1):31, 1999.

[64] D. A. Gorham and A. H. Kharaz. The measurement of particle rebound characteristics. *Powder Technology*, 112(3):193–202, 2000.

[65] A. H. Kharaz, D. A. Gorham, and A. D. Salman. An experimental study of the elastic rebound of spheres. *Powder Technology*, 120(3):281–291, 2001.

[66] O. Cermik, H. Ghaednia, and D. Marghitu. Experimental coefficient of friction for the impact of a tennis ball. *Stle Annual Meeting Exhibition*, 2014.

[67] H. Ghaednia, D. B. Marghitu, and R. L. Jackson. Predicting the permanent deformation after the impact of a rod with a flat surface. *Journal of Tribology*, 137(1):011403, 2015.

[68] H. Gheadnia, O. Cermik, and D. B. Marghitu. Experimental and theoretical analysis of the elasto-plastic oblique impact of a rod with a flat. *International Journal of Impact Engineering*, 86:307–317, 2015.

[69] H. Ghaednia and D. B. Marghitu. Permanent deformation during the oblique impact with friction. *Archive of Applied Mechanics*, 86(1-2):121–134, 2016.

[70] D. B. Marghitu, D. Cojocaru, and R. L. Jackson. Elasto-plastic impact of a rotating link with a massive surface. *International Journal of Mechanical Sciences*, 53(4):309–315, 2011.

[71] F. Pfeiffer. Impacts with friction: structures, energy, measurements. *Archive of Applied Mechanics*, pages 1–21, 2016.

[72] K. Kardel, H. Ghaednia, A. L. Carrano, and D. B. Marghitu. Experimental and theoretical modeling of behavior of 3d-printed polymers under collision with a rigid rod. *Additive Manufacturing*, 14:87–94, 2017.

[73] L. Labous, A. D. Rosato, and R. N. Dave. Measurements of collisional properties of spheres using high-speed video analysis. *Physical review E*, 56(5):5717, 1997.

[74] S. R. Goodwill and S. J. Haake. Spring damper model of an impact between a tennis ball and racket. *Proceedings of the Institution of Mechanical Engineers, part C: Journal of mechanical engineering science*, 215(11):1331–1341, 2001.

[75] S. Goodwill, J. Douglas, S. Miller, and S. Haake. Measuring ball spin off a tennis racket. In *The Engineering of Sport 6*, pages 379–384. Springer, 2006.

[76] S. J. Haake, M. J. Carre, and S. R. Goodwill. The dynamic impact characteristics of tennis balls with tennis rackets. *Journal of sports sciences*, 21(10):839–850, 2003.

[77] T. Allen, S. Haake, and S. Goodwill. Comparison of a finite element model of a tennis racket to experimental data. *Sports engineering*, 12(2):87–98, 2009.

[78] R. Cross. Enhancing the bounce of a ball. *The Physics Teacher*, 48(7):450–452, 2010.

[79] R. Cross. Measurements of the horizontal coefficient of restitution for a superball and a tennis ball. *American Journal of Physics*, 70(5):482–489, 2002.

[80] R. Cross. Behaviour of a bouncing ball. *Physics Education*, 50(3):335, 2015.

[81] B. Pan, K. Qian, H. Xie, and A. Asundi. Two-dimensional digital image correlation for in-plane displacement and strain measurement: a review. *Measurement science and technology*, 20(6):062001, 2009.

[82] Y. Sun, J. H. L. Pang, X. Shi, and J. W. R. Tew. Thermal deformation measurement by digital image correlation method. In *Thermal and Thermomechanical Phenomena in*

Electronics Systems, 2006. ITHERM'06. The Tenth Intersociety Conference on, pages 921–927. IEEE, 2006.

[83] W. H. Peters and W. F. Ranson. Digital imaging techniques in experimental stress analysis. *Optical engineering*, 21(3):213427–213427, 1982.

[84] M. A. Sutton, W. J. Wolters, W. H. Peters, W. F. Ranson, and S. R. McNeill. Determination of displacements using an improved digital correlation method. *Image and vision computing*, 1(3):133–139, 1983.

[85] H. A. Bruck, S. R. McNeill, M. A. Sutton, and W. H. Peters Iii. Digital image correlation using newton-raphson method of partial differential correction. *Experimental Mechanics*, 29(3):261–267, 1989.

[86] C. Q. Davis and D. M. Freeman. Statistics of subpixel registration algorithms based on spatiotemporal gradients or block matching. *Optical Engineering*, 37(4):1290–1298, 1998.

[87] G. C. Jin, X. F. Yao, and N. K. Bao. Applications of speckle metrology to vibration and deformation measurements of electronic devices. In *Thermal and Thermomechanical Phenomena in Electronic Systems, 2000. ITHERM 2000. The Seventh Intersociety Conference on*, volume 2, pages 253–255. IEEE, 2000.

[88] J. Chen, X. Zhang, N. Zhan, and X. Hu. Deformation measurement across crack using two-step extended digital image correlation method. *Optics and Lasers in Engineering*, 48(11):1126–1131, 2010.

[89] J. Chen, G. Xia, K. Zhou, G. Xia, and Y. Qin. Two-step digital image correlation for micro-region measurement. *Optics and Lasers in Engineering*, 43(8):836–846, 2005.

[90] B. Pan, A. Asundi, H. Xie, and J. Gao. Digital image correlation using iterative least squares and pointwise least squares for displacement field and strain field measurements. *Optics and Lasers in Engineering*, 47(7):865–874, 2009.

[91] B. Pan. Reliability-guided digital image correlation for image deformation measurement. *Applied optics*, 48(8):1535–1542, 2009.

[92] B. Pan and K. Li. A fast digital image correlation method for deformation measurement. *Optics and Lasers in Engineering*, 49(7):841–847, 2011.

[93] B. Pan, W. Dafang, and X. Yong. Incremental calculation for large deformation measurement using reliability-guided digital image correlation. *Optics and Lasers in Engineering*, 50(4):586–592, 2012.

[94] B. Pan, K. Li, and W. Tong. Fast, robust and accurate digital image correlation calculation without redundant computations. *Experimental Mechanics*, 53(7):1277–1289, 2013.

[95] R. O. Duda, P. E. Hart, et al. *Pattern classification and scene analysis*, volume 3. Wiley New York, 1973.

[96] J. A. Richards. *Remote sensing digital image analysis*, volume 3. Springer, 1999.

[97] P. V. C. Hough. Method and means for recognizing complex patterns. Technical report, 1962.

[98] D. H. Ballard. Generalizing the hough transform to detect arbitrary shapes. *Pattern recognition*, 13(2):111–122, 1981.

[99] S. Bossuyt. Optimized patterns for digital image correlation. In *Imaging Methods for Novel Materials and Challenging Applications, Volume 3*, pages 239–248. Springer, 2013.

[100] B. Pan, K. Qian, H. Xie, and A. Asundi. On errors of digital image correlation due to speckle patterns. In *International Conference on Experimental Mechnics 2008 and Seventh Asian Conference on Experimental Mechanics*, pages 73754Z–73754Z. International Society for Optics and Photonics, 2008.

[101] S. A. Collette, M. A. Sutton, P. Miney, A. P. Reynolds, X. Li, P. E. Colavita, W. A. Scrivens, Y. Luo, T. Sudarshan, P. Muzykov, et al. Development of patterns for nanoscale strain measurements: I. fabrication of imprinted au webs for polymeric materials. *Nanotechnology*, 15(12):1812, 2004.

[102] D. Lecompte, A. Smits, S. Bossuyt, H. Sol, J. Vantomme, D. Van Hemelrijck, and A.M. Habraken. Quality assessment of speckle patterns for digital image correlation. *Optics and lasers in Engineering*, 44(11):1132–1145, 2006.

[103] R.L. Jackson, I.Chusoipin, and I. Green. A finite element study of the residual stress and strain formation in spherical contacts. *ASME Journal of Tribology*, 60(3):217–229, 2010.

[104] W. Goldsmith. *Impact*. Courier Dover Publications, 2001.

[105] L. Shapiro and G. C. Stockman. Computer vision. 2001. *ed: Prentice Hall*, 2001.

[106] G. C. Stockman and A. K. Agrawala. Equivalence of hough curve detection to template matching. *Communications of the ACM*, 20(11):820–822, 1977.